STAR BUR Run 25

STAR Collaboration

November 1, 2024

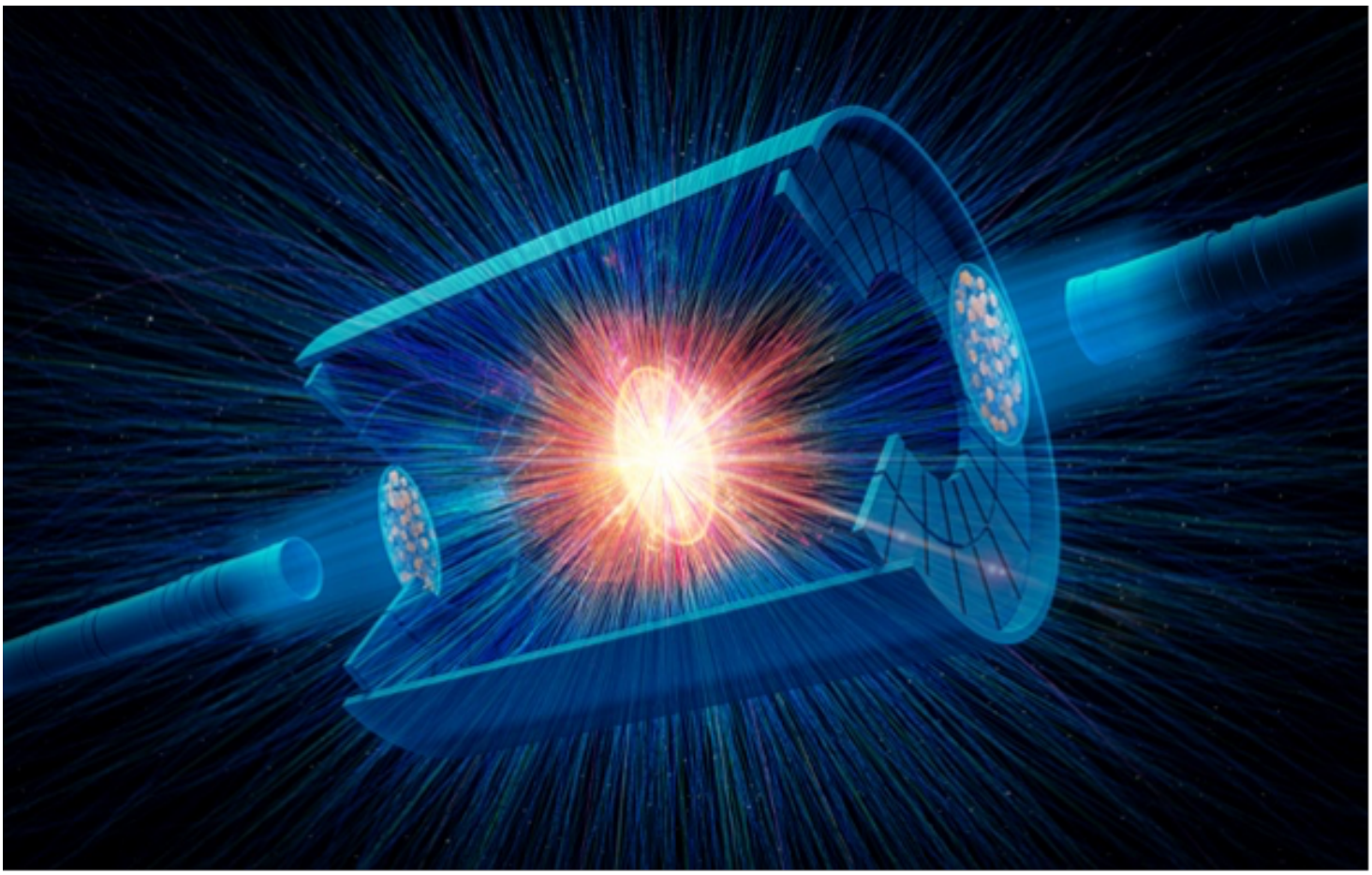

Courtesy of Brookhaven National Lab

Executive Summary

This Beam Use Request outlines the compelling physics programs proposed by STAR collaboration for data taking in RHIC's final run in 2025.

STAR's **highest scientific priority** is to complete the Hot QCD physics program via the collection of 200 GeV Au+Au collisions and the "must-do" Cold QCD forward physics program enabled by the recently completed suite of forward detectors via the collection of transversely polarized p+Au data at 200 GeV in Run-25. A combination of soft and hard probes collected during 2025, as outlined in Table 1, will be used to probe the QGP's microstructure and continue our unique forward physics program via the collection of high statistics Au+Auand p+Au data at $\sqrt{s_{\rm NN}} = 200$ GeV.

Table 1: Proposed Run-25 assuming 20 or 28 cryo-weeks of running in 2025 and 2 weeks of set-up time to achieve minimum-bias running conditions. For both scenarios, we request 200 GeV Au+Au collisions. We provide the requested event count for our minimum bias (MB) trigger, and the requested sampled luminosity from our a high-$p_{\rm T}$ trigger that covers all v_z. During Runs 23 and 24, STAR collected 8 billion MB Au+Au events and achieved a sampled luminosity of 1.2 nb^{-1}.

$\sqrt{s_{\rm NN}}$ (GeV)	Species	Number Events/ Sampled Luminosity	Year
200	Au+Au	8B+**5B** / 1.2 nb^{-1}+**20.8 nb^{-1}**	2023+2024+**2025 (20 cryo-weeks)**
200	Au+Au	8B+**9B** / 1.2 nb^{-1}+**28.6 nb^{-1}**	2023+2024+**2025 (28 cryo-weeks)**

STAR's scientific program is enabled by combining the detector upgrades for Beam Energy Scan phase II (BES-II) and the Forward Upgrades. Together, they generate STAR's unique particle identification (PID) capabilities over an extended rapidity acceptance and down to very low transverse momentum ($p_{\rm T}$) while maintaining a low material budget. All these new detectors are now fully commissioned and have operated exceptionally well during the past three runs.

Significantly increased luminosities, the extended acceptance at mid-rapidity due to the iTPC, improved event plane and triggering capabilities via the EPD, and the ability to probe the previously inaccessible forward region are all exploited in our Hot QCD program, which informs on the microstructure of the QGP, and in our Cold QCD program that will utilize transverse polarization setting the stage for related future measurements at the Electron-Ion Collider (EIC).

Combined Au+Au datasets collected in Run-23, Run-24, and Run-25 will allow STAR to address essential questions about the inner workings of the QGP, including the temperature dependence of the shear and bulk viscosities, the 3-D nature of the initial state, how global vorticity is transferred to the spin angular momentum of particles on such short time scales, and the chiral properties of the medium.

The scenario in which Run-25 is reduced to 20 cryo-weeks would significantly increase the statistical and systematic uncertainties of all the data, impacting the excellent precision we aim for with the measurements described in this BUR.

We estimate that 20 instead of 28 cryo-weeks will decrease STAR's Au+Au data sample by at least 24-26%

STAR considered it critical that we collect approximately equal nucleon-nucleon luminosities for p+p and p+Au at 200 GeV during Run-24. This optimizes the statistical precision of several critical observables that require comparisons between results in both p+p and p+Au. However, due to the priorities set by the PAC, no p+Au data were collected in Run-24. STAR would like to request an extension of Run-25 beyond the 28 cryo-weeks, allowing 5 weeks of physics data collection to achieve a sampled luminosity of 0.22 pb^{-1}. The detector upgrades implemented since Run 15 will enable critical and qualitatively new measurements that were not previously possible at RHIC.

Finally, in Section 3, we propose the collection of two datasets if the opportunity arises after the collection of our higher-priority datasets outlined above. One proposal enables the imaging of the shape and radial profile of atomic nuclei via collective flow measurements. Such studies are important to improve our understanding of the complex initial conditions and subsequent hydrodynamical response of the medium. Information on these deformation and nuclear skin parameters is also of significant interest to the nuclear structure physics community. Heavy ion collision data have different sensitivities to nuclear structure experiments and are, therefore, promising complementary tools to probe different aspects of the nucleus' shape and substructure. The other proposal expands our fixed-target program to include other light beam and target combinations. These data will help clarify the role and mechanisms of nucleon stopping. In addition, light nucleus cross-sections in the target/projectile regions using beams of 3-50 GeV/n are of great interest to the NASA Space Radiation Protection community.

Contents

1 Run-25 Requests for Au+Au Collisions at 200 GeV

1.1 Explore the Microstructure of the QGP

The completion of RHIC's scientific mission involves two central goals: (i) mapping out the QCD phase diagram, and (ii) understanding the inner workings of the QGP by resolving its properties at varying length scales [1]. The former goal is addressed by the BES-II/FXT program. For the latter goal, the complementarity of the RHIC and LHC facilities is scientifically as essential as having more than one experiment independently studying the microstructure of the QGP at RHIC. With several years of operating the iTPC upgrade and commissioning and operation of the forward detectors in Run-22, the STAR collaboration is in an excellent position to take advantage of its vastly improved detection capabilities. Combining this with the substantial increase in beam luminosities in Run-23 and Run-25, RHIC is uniquely positioned to fully engage in a detailed exploration of the QGP's microstructure.

Through careful discussions in its physics working groups, the STAR collaboration has identified a number of topics that together with the expected sPHENIX results in 2023-25 make up a comprehensive study of the QGP microstructure, and successfully complete RHIC's scientific mission. In this section, we present a selection of those topics that will take full advantage of both STAR and RHIC's unique capabilities and address the following important questions about the inner workings of the QGP. We enumerate questions below that follow the chronology of an event; from questions addressing the QCD vacuum and the initial conditions, to the formation, temperature, and properties of the QGP, to the quenching of jets in said QGP, to its phase transition back to hadronic matter, and finally to the interactions of those final state hadrons.

1. **What is the nature of the 3-dimensional initial state at RHIC energies?** How does a twist of the event shape break longitudinal boost invariance and decorrelate the direction of an event plane? Can the J/ψ v_1 tell us about the initial tilt angle of the source? Can the Wigner distributions of photon tell us about the magnetic field effects in the initial state?

2. **What is the precise temperature dependence of the shear (η/s) and bulk (ζ/s) viscosities?** Can combining precision flow results at different beam energies help determine the temperature dependence of the viscosity?

3. **What can we learn about confinement from charmonium measurements?** Can the elliptic flow of J/ψ tell us whether charmed quarks are deconfined?

4. **What is the temperature of the medium?** Do the Υ and ψ(2S) melt at RHIC energies, and if so can their suppression be used to determine the temperature of the QGP? The thermally produced dileptons are also sensitive to the medium temperature. Does their temperature agree with that found via quarkonium suppression?

5. **What are the electrical, magnetic, and chiral properties of the medium?** How is global vorticity transferred to the spin angular momentum of particles on such

short time scales? And, how can the global polarization of hyperons be reconciled with the spin alignment of vector mesons? Can dilepton production in the low mass region tell us about the electrical conductivity of the plasma? Can clear observation of the ρ^0-a_1 mixing tell us about the degrees of freedom therefore the chirality of the plasma? Is there local parity violation and chiral magnetic effect?

6. **What are the underlying mechanisms of jet quenching at RHIC energies?** What do jets tell us about the microscopic structure of the QGP as a function of resolution scale?

7. **What is the precise nature of the transition near $\mu_B = 0$?** Where does the sign-change of the susceptibility ratio χ_6^B/χ_2^B take place?

8. **What can we learn about the strong interaction?** Can correlation functions between baryons emitted at the surface of the fireball tell us how they interact in free space.

The impetus for running STAR during Run-23 and Run-25 for Au+Au 200 GeV collisions comes from gains via: i) enhanced statistics, ii) extended acceptance, and iii) low material budget.

With the successful upgrade of the DAQ system, STAR is able to record minimum bias events at a rate about factor of 2 faster than before. The increased DAQ speed can also facilitate sampling a large luminosity for rare probes. The projected statistics for both minimum bias events and sampled luminosity are listed in Table 1. In order to achieve a balance between those physics observables which are acquired with a minimum bias trigger (and negatively impacted by excess tracks in the TPC) and the rare probes which require specialized triggers (Barrel High Tower (BHT), dimuon) and the highest luminosity which can be accommodated with the TPC, the collaboration will optimize the interaction rates at STAR by allocating high and low luminosity periods. CAD can offset the beam to independently control the maximum luminosity in each IR. Such separation will allow us to collect clean, low pile-up, minimum bias events, with improved tracking efficiency, which is expected to especially benefit many of the proposed correlation analyses. The dedicated high luminosity period will enable a significant improvement in the precision and kinematic reach of current STAR measurements, and making important measurements that are yet more differential possible.

The extended acceptance is important for analyses that probe the η dependencies and especially so for those that require correlations between particles (CME, $v_2(\eta)$, $r_n(\eta)$, and $P_H(\eta)$). With the BES-II upgrades and the recent forward upgrade, STAR's acceptance spans from mid-rapidity to beam rapidity. STAR's BES-II upgrade sub-systems comprised of the inner Time Projection Chamber (iTPC, $|\eta| < 1.5$), endcap Time Of Flight (eTOF, $1 < \eta < 1.5$) and Event Plane Detectors (EPDs, $2.1 < |\eta| < 5.1$), that are all fully operational since the beginning of 2019 [2–4]. In what follows, we will refer to the combination of the existing TPC ($|\eta| < 1$) and the iTPC upgrade as iTPC ($|\eta| < 1.5$) for simplicity. The STAR Collaboration has also commissioned and operated a forward rapidity ($2.5 < \eta <$

4) upgrade that includes charged particle tracking and electromagnetic/hadronic calorimetry [5]. Charged particle tracking is achieved using a combination of silicon detectors and small strip thin gap chamber detectors. The combination of these two tracking detectors is referred to as the forward tracking system (FTS). The FTS is capable of discriminating the hadron charge sign. It can measure p_{T} of charged particles in the range of $0.2 < p_{\mathrm{T}} < 2$ GeV/c with $20-30\%$ momentum resolution.

In the previous 200 GeV Au+Au runs in 2014 and 2016, STAR included inner silicon detectors (the Heavy Flavor Tracker). This has since been removed and by comparison in Run-23–25 STAR will have a reduced material budget between the beam and the iTPC, which is essential for performing dielectron measurements. With these measurements, we propose to study the initial conditions (Wigner functions, photoproduction of J/ψ), the degree of freedom of the medium (excess yield), and its temperature (slope in the intermediate mass region).

A synopsis of the proposed analyses, which questions they address, whether they will be part of the minimum bias (low luminosity) or specialized trigger (high luminosity) program, which coverage is essential, and the required trigger is shown in Fig. 1. The following subsections will address the specific analyses which are proposed to answer the questions outlined above. The questions sequentially step through the chronology of an event.

Please note that all the following projection plots use assumed statistics of 20 B MB events and 34 nb^{-1} of sampled luminosity during high-luminosity running period for Run-23+25. Combined with the MB events, the total sampled luminosity is 37 nb^{-1}. As shown in Table 1 of the Executive Summary, the latest projected statistics is about 10% less than what's assumed in this section. Nevertheless, it is straightforward to scale the projected error bars to take into account such differences.

Observable	Question	PWG	MB/H$\mathcal{L}$	Coverage	Trigger
$v_2(\eta)$ Twist	1) Initial State	FCV	Min bias	iTPC, TOF, EPD, FTS	MB
$r_n(\eta_a,\eta_b)$	1) Initial State	FCV	Min Bias	iTPC, TOF, EPD, FTS	MB
J/ψ v_1	1) Initial State	HP	Luminosity	iTPC, TOF, EPD	MB+BHT
Photon WF	1) Initial State	LFSUPC	Min Bias	iTPC, TOF	MB
$v_2(\eta)$	2) Viscosity	FCV	Min bias	iTPC , TOF, EPD, FTS	MB
J/ψ v_2	3) Deconfinement	HP	Luminosity	iTPC, TOF, EPD	MB+BHT
Υ Suppression	4) Temperature	HP	Luminosity	iTPC, TOF	BHT+Dimuon
$\psi(2s)$ suppress.	4) Temperature	HP	Min Bias	iTPC, TOF	MB
Di-elec IMR	4) Temperature	LFSUPC	Min Bias	iTPC, TOF	MB
$P_H(\eta)$	5) Properties	FCV	Min Bias	iTPC, TOF, FTS, EPD	MB
P_H of J/ψ	5) Properties	FCV	Luminosity	iTPC, TOF, EPD	MB+BHT
ρ^0 a_1 mixing	5) Properties	LFSUPC	Min Bias	iTPC, TOF	MB
Di-elec LMR	5) Properties	LFSUPC	Min Bias	iTPC, TOF	MB
CME	5) Properties	FCV	Min Bias	iTPC, TOF, EPD	MB
γ_{Dir} + jet I_{AA}	6) Jet quenching	HP	Luminosity	BEMC, EEMC FCS	BHT
γ_{Dir} + jet acopl.	6) Jet quenching	HP	Luminosity	BEMC, EEMC, FCS	BHT
Jet substruct.	6) Jet quenching	HP	Luminosity	BEMC, EEMC, FCS	BHT
Net-p C_6	7) Phase Transition	CF	Min Bias	iTPC, TOF	MB
Baryon CF	8) Strong Interact.	CF	Min Bias	iTPC, TOF	MB
UPC ρ^0, ϕ, J/ψ	UPC – CNM	LFSUPC	Luminosity	iTPC, TOF, BEMC, EEMC	ZDCEW, UPC
v_2 in γ+Au (UPC)	UPC – CNM	FCV	Min Bias	iTPC, TOF, FTS	UPC
UPC di-jets	UPC – CNM	HP	Luminosity	iTPC, TOF, BEMC	UPC+BHT
UPC CP spectra	UPC – CNM	LFSUPC	Min Bias	iTPC, TOF	ZDCE(1n)+ZDCW

Figure 1: A tabulation of the proposed analyses. The columns indicate which of the eight questions a given analysis addresses, which physics working group will lead the analysis effort, whether the analysis will be part of the low or high luminosity program, which detector systems are essential, and the required trigger for that analysis.

1.1.1 What is the Nature of the 3D Initial State?

Pseudorapidity-dependent azimuthal correlations to constrain the longitudinal structure of the initial state ($v_n(\eta)$)

Initial-state longitudinal fluctuations and the fluid dynamical response of the medium formed in heavy-ion collisions can lead to de-correlations of the direction of the reaction planes Ψ_n (which determines the orientation of the harmonic anisotropies) with pseudorapidity (see Fig. 2). Such effects are often referred to as a torque or twist of the event shape [6–8] that eventually leads to a breaking of longitudinal/boost/rapidity invariance. The magnitude of the de-correlation is determined by the details of the dynamics of initial state, and the distribution of nucleons and partons inside the colliding nuclei.

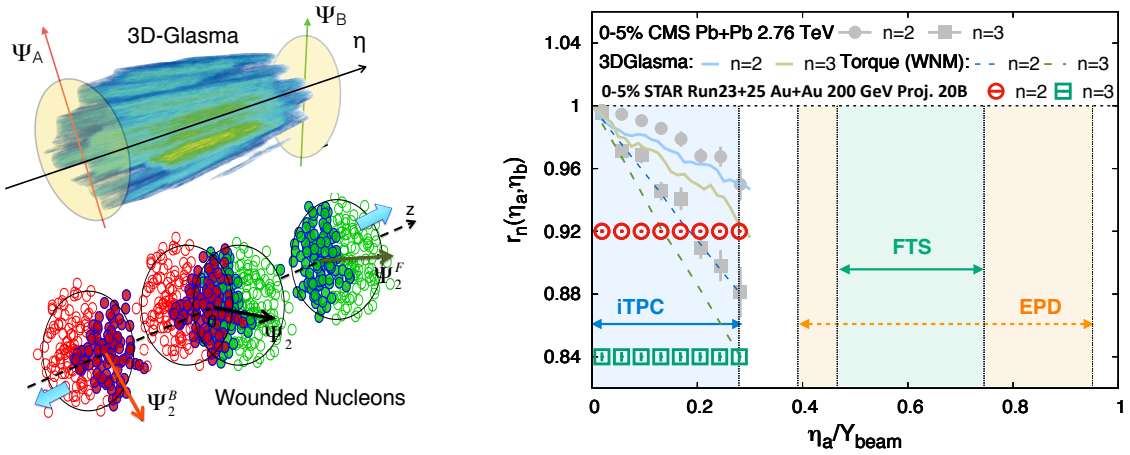

Figure 2: (Left) Cartoon to demonstrate the de-correlation of event planes in the longitudinal direction of a collision from a gluon saturation based 3D-Glasma model [9] and a wounded nucleon model (WNM). [6, 10] (Right) The longitudinal de-correlation of the elliptic anisotropy plane as a function of pseudorapidity in units of beam rapidity. CMS results are compared to predictions from two models, along with STAR projection for Run-23 (using preliminary Run-19 results) from a sample of anticipated 10 B min-bias events. The colored regions show that with iTPC+EPD+FTS one can extend such measurements with good precision by covering a large fraction of the beam rapidity at 200 GeV. This demonstrates the unique strength of STAR to study the physics of 3D initial state.

Several promising observables have been proposed to study this effect, Fig. 2 shows one which can be expressed as $r_n(\eta_a, \eta_b) = V_{n\Delta}(-\eta_a, \eta_b)/V_{n\Delta}(\eta_a, \eta_b)$, where $V_{n\Delta}$ is the Fourier coefficient calculated with pairs of particles taken from three different pseudorapidity regions $-\eta_a$, η_a and η_b. The observable $r_n(\eta_a, \eta_b)$ was originally introduced and measured by CMS collaboration in Ref. [11] and also been measured by the ATLAS collaboration in [12]. An observable using three-particle correlations that is sensitive to this effect is the relative pseudorapidity dependence of the three-particle correlator $C_{m,n,m+n}(\eta_a, \eta_b, \eta_c) = \langle\cos(m\phi_1(\eta_a) + n\phi_2(\eta_b) - (m+n)\phi_3(\eta_c)\rangle$ [13]. Another variable, very similar to r_n in terms of design but involving four-particle correlations, is: $R_{n,n|n,n}(\eta_a, \eta_b)$ [14]. As shown in Fig. 2,

CMS measurements of r_n show strong de-correlation ($\sim$ 16% for n=3, $\sim$ 8% for n=2) in central events within the range of their acceptance. In the 3D-Glasma model of initial state, the breaking of boost invariance is determined by the QCD equations which predict the evolution of gluons in the saturation regime with Bjorken-x. At the LHC such models predict weaker de-correlations as compared to wounded nucleon models. The 3D-Glasma model underpredicts r_2 and overpredicts r_3 results from CMS [9].

One expects the nature of the initial state to change from LHC to RHIC, in particular the region of Bjorken-x probed is very different. It is therefore extremely important to utilize the enhanced acceptance of the STAR detector to study this effect in 200 GeV Au+Au collisions. In Fig. 2 STAR's projections using preliminary Run-19 results to estimate the uncertainties for 10 B events are shown for the measurement of r_n within the acceptance $|\eta| < 1.5$. The colored regions show that with iTPC+EPD+FTS one can extend such measurements using observables $r_n, C_{m,n,m+n}, R_{n,n|n,n}$ with good precision by covering either an equal (iTPC only) or larger (iTPC+FTS+EPDs) fraction of the beam rapidity at 200 GeV compared to the LHC measurements. This unique measurement capability will help pin down the nature of the 3-D initial state of heavy ion collisions. It will also help constrain different models of QCD that predict different rapidity (or Bjorken-x) dependence of valance quark and gluon distributions inside colliding nuclei as has been demonstrated by theoretical calculations in Ref. [9, 15].

J/ψ v_1 to study the initial tilt

Studies of the directed flow, v_1, as a function of rapidity provide crucial information to understand the initial tilt of the medium produced in heavy-ion collisions [16,17]. Heavy quarks are produced in the early stage of a heavy-ion collision and thus are of particular interest for the medium initial asymmetry studies. STAR recently reported the first measurement of D-meson v_1 in Au+Au collisions at 200 GeV where the magnitude of the heavy-flavor meson v_1 is about 25 times larger than the v_1 for charged kaons.

With the Run-23 and Run-25 data, STAR would have a unique opportunity to study the v_1 of a bound $c\bar{c}$ state, the J/ψ mesons, for which even larger directed flow can be expected [18]. In addition to STAR's excellent capability to reconstruct low-$p_{\rm T}$ J/ψ, the iTPC will improve the momentum resolution and extend the pseudorapidity coverage. This will provide better precision for the slope extraction of v_1 vs. y, which quantifies the strength of the directed flow. The expected precision of a J/ψ v_1 measurement vs $p_{\rm T}$ at STAR in Runs-23 and 25, assuming 20 B MB events and 34 nb^{-1} of BHT trigger sampled luminosity, in 0-80% central Au+Au collisions at 200 GeV is shown in Fig. 3.

Studying the photon Wigner function and initial-state magnetic fields

The $p_{\rm T}$ broadening of the dilepton pairs from photon-photon interactions has been observed in hadronic heavy-ion collisions compared to that in UPCs [19, 20]. The unsuccessful description of STAR data by the STARLight model led to the attribution of the broadening to the possible residual magnetic field trapped in an electrically conducting QGP [19]; which is key information to the study of the chiral magnetic effect. Similarly, ATLAS quantified

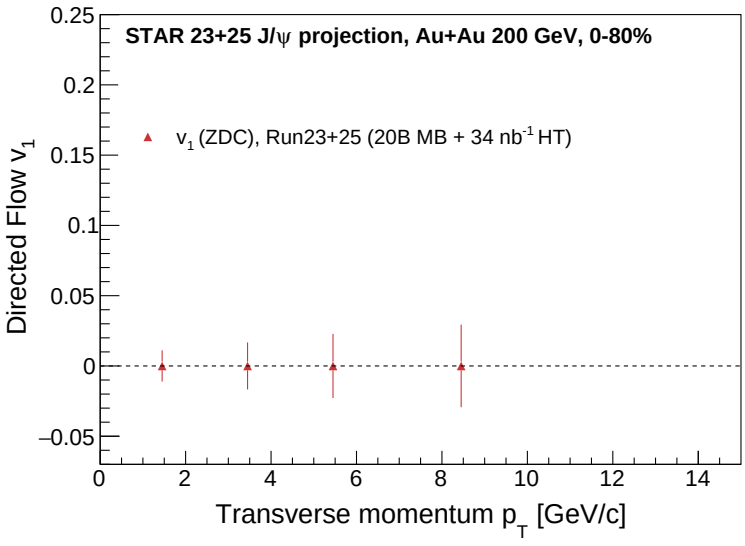

Figure 3: Precision projection for J/ψ ($J/\psi \to e^+e^-$) directed flow (v_1) vs J/ψ $p_{\rm T}$ in 0-80% Au+Au collisions at $\sqrt{s_{\rm NN}}$ = 200 GeV, assuming 20 B MB events and 34 nb^{-1} of BHT trigger sampled luminosity.

the effect via the acoplanarity of lepton pairs in contrast to the measurements in UPCs and explained the additional broadening by multiple electromagnetic scatterings in the hot and dense medium [20], which is analogous to the medium $P_\perp$-broadening effects for jet quenching. These descriptions of the broadening in hadronic collisions are based on the assumption that there is no impact parameter dependence of the p_T distribution for the electromagnetic production. Recent lowest-order QED calculations, in which the impact parameter dependence is recovered, could reasonably describe the broadening observed by STAR and ATLAS without any hot medium effect.

To further shed light on the underlying mechanism, we propose to precisely study the initial $p_{\rm T}$-broadening for the dilepton pair in ultra-peripheral and peripheral collisions. Different neutron emission tags serve as the centrality definition, which will allow us to explore the baseline broadening variation with impact parameter. Furthermore, the differential spectra as a function of pair $p_{\rm T}$, rapidity, and mass enable us to study the Wigner function of the initial electromagnetic field, which provides information to extract the momentum and space correlation of electromagnetic field.

As shown in Fig. 4, compared with the latest QED calculation, there still exists possible additional broadening in peripheral collisions, although the significance is only about 1σ, which leaves room for potential medium effects. In Run-23 and Run-25, as projected in the figure, we could judge the existence of additional broadening with much higher precision and further constrain the strength of final-state magnetic field in the QGP.

Precision measurement of the amplitude of the recently observed $\cos 4\Delta\phi$ modulation of the $\gamma\gamma \to e^+e^-$ process will allow mapping the photon Wigner function and provide additional constraints on possible final-state effects, thereby complementing the $p_{\rm T}$ broadening

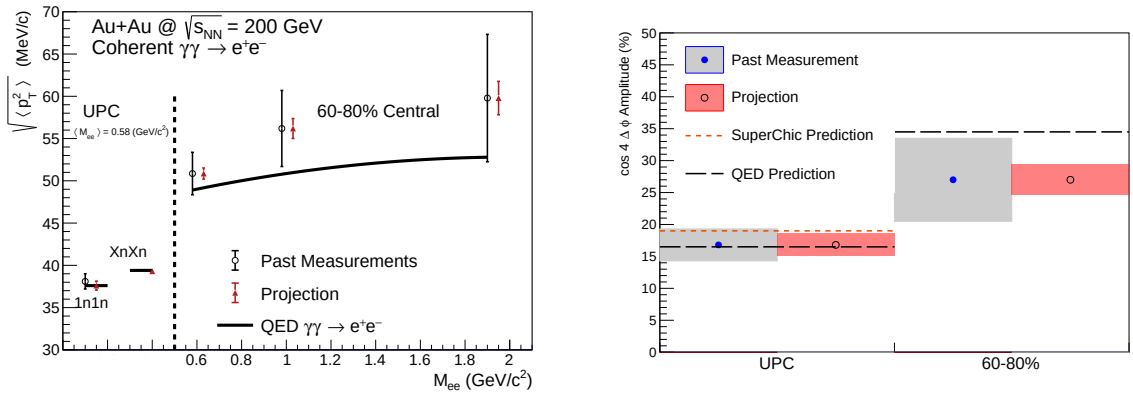

Figure 4: Projections for measurements of the $\gamma\gamma \to e^+e^-$ process in peripheral and ultra-peripheral collisions. Left: The $\sqrt{\langle p_T^2 \rangle}$ of dielectron pairs within the fiducial acceptance as a function of pair mass, M_{ee}, for 60–80% peripheral and ultra-peripheral Au+Au collisions at $\sqrt{s_{\rm NN}} = 200$ GeV. Right: The projection of the $\cos 4\Delta\phi$ measurement for both peripheral (60–80%) and ultra-peripheral collisions.

measurement. Figure 4 (right panel) shows the projected precision for a measurement of the $\cos 4\Delta\phi$ modulation in Run-23+25. The modulation is a direct result of the mismatch in initial and final spin configuration of the $\gamma\gamma \to e^+e^-$ process. Any final-state effect that modifies the $p_{\rm T}$ will necessarily reduce the amplitude of the modulation. Assuming the same central values as previously measured, evidence for suppression of the $\cos 4\Delta\phi$ modulation will be visible at the $> 3\sigma$ level (stat. & syst. uncertainty). Precision measurement of the $\cos 4\Delta\phi$ modulation in Run-23+25 may also allow a first direct experimental measurement of the impact parameter dependence of this new observable (by comparing UPC and 60–80%). Assuming the same central values as previously measured, the improved precision will provide evidence for impact parameter dependence at the $> 3\sigma$ level (stat. & syst. uncertainty). Assuming the central values predicted by QED would lead to a $> 5\sigma$ difference between the UPC case and the 60–80% case.

1.1.2 What is the Precise Temperature Dependence of Viscosity?

The idea of tightly constraining the temperature dependent viscosity of the QGP was envisioned in the 2015 Long Range Plan for Nuclear Science [1]. The QCD matter formed at RHIC shows nearly perfect fluidity characterized by the smallest viscosity to entropy ratio η/s known in nature. One major aim is to perform precision measurements to constrain the temperature dependence of the shear $\eta/s(T)$ and bulk $\zeta/s(T)$ viscosities. Recent state-of-the-art Bayesian analyses of flow and spectra data within sophisticated event-by-event hydrodynamic models has show strong evidence for temperature dependence of η/s and ζ/s [21–23], but the uncertainties are still quite large. On the other hand, hydrodynamic simulations have demonstrated that since the temperature of the produced fireball varies with rapidity, the measurement of the rapidity dependence of flow harmonics can provide

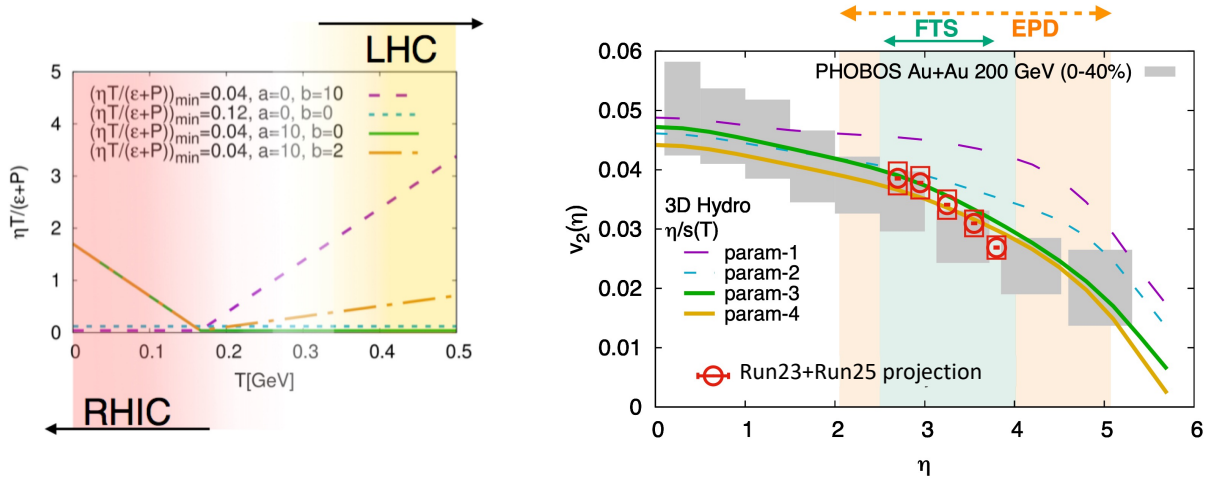

Figure 5: (Left) Different parameterizations of the temperature dependence of the shear viscosity to entropy ratio $\eta/s(T)$ (at $\mu_B = 0$) used in the hydrodynamic simulation of Ref. [24]. It has been demonstrated in Ref. [25] that the region of lowest η/s is the one that can be probed at RHIC. (Right) Effects on the elliptic flow co-efficient v_2 due to different parameterizations of the viscosity parameter, indicating better constraints on $\eta/s(T)$ can only be performed by measurements at forward rapidities at RHIC. The interpretation of the existing PHOBOS data is limited by the large uncertainties. Projections for STAR measurements are shown on the same plot.

additional constraints on the η/s(T) and $\zeta/s(T)$. [24] For this, RHIC measurements have an advantage over the LHC since the smaller beam rapidity at RHIC provides stronger variations of the temperature with rapidity. The beam energy scan at RHIC provides an additional handle on temperature to map $\eta/s(T)$, and $\zeta/s(T)$ over a wide range of temperatures. Indeed, the hydrodynamic simulation of Ref. [24] indicates that $\eta/s(T)$ at lower temperatures, near its possible minimum ($T = T_c$), can be better constrained by RHIC measurements. In this simulation, a number of QCD-motivated parameterizations of the temperature dependence of the shear viscosity were assumed, as shown in Fig. 5 (left).

Existing data from the PHOBOS collaboration suffer from large uncertainties, therefore only limited constraints on the temperature dependence of the transport parameters can be achieved. The BES-II upgrades and the FTS will provide precise estimations of different azimuthal correlation observables: $v_n(\eta)$ and other higher-order ($n > 2$) flow coefficients $v_n(\eta)$, its fluctuations $\sigma(v_n)/v_n$ that have never been measured at forward rapidity, which are essential in terms of constraining $\eta/s(T)$ near its possible minimum. These quantities previously measured at mid-rapidity are not enough for discriminating different parameterizations of $\eta/s(T)$ as shown in the hydrodynamic simulation of Ref. [24]. While $p_{\rm T}$ integrated quantities at forward rapidity can constrain the shear viscosity, measurement of the $p_{\rm T}$ of particles at forward rapidity (i.e. FTS) is essential to constrain the bulk ζ/s – in particular the information of $\langle p_T \rangle$ is needed to constrain $\zeta/s(T)$. With the FTS it will be possible to measure the $p_{\rm T}$ dependence of v_n in Au+Au collisions in Run-23+25.

1.1.3 What can Charmonium Tell Us about Deconfinement?

The strong collectivity of the QGP can be studied by measuring the azimuthal anisotropy of the produced particles in heavy-ion collisions. A positive elliptic flow coefficient (v_2) of the light flavor hadrons, and also D-mesons and electrons from heavy-flavor hadron decays are observed in Au+Au collisions at $\sqrt{s_{\rm NN}} = 54.4$ and 200 GeV at RHIC. This corroborates that, like light-flavor, the charm quarks could also be (partially) thermalized and show collectivity in the QGP.

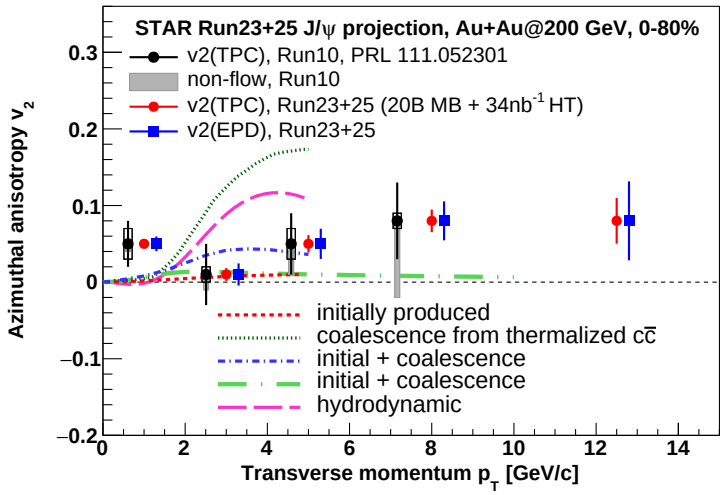

Figure 6: Precision projection for J/ψ ($J/\psi \to e^+e^-$) elliptic flow (v_2) vs J/ψ $p_{\rm T}$ in 0–80% Au+Au collisions at 200 GeV, assuming 20 B MB events and 34 nb^{-1} of BHT trigger sampled luminosity. Projections (red circles and blue squares) are compared with previously published results (black circles) [26] and various model calculations.

On the other hand, the v_2 of heavier J/ψ reported by STAR based on the 2010 Au+Au 200 GeV data sample [26], shown as black circles in Fig. 6, was found to be consistent with zero within large statistical uncertainties and systematic uncertainties due to non-flow effects. The precision of the measurement was not high enough to distinguish between theoretical model calculations that assume only primordial J/ψ production and ones that include additional J/ψ production via regeneration, illustrated as lines of different styles in Fig. 6. This calls for a larger sample of Au+Au collisions at 200 GeV, as will be provided by RHIC in Run-23 and Run-25, in order to observe a possible non-zero J/ψ v_2 at RHIC energies and provide additional insights to the J/ψ production mechanism especially regarding the regeneration contribution. Particularly important for these studies is STAR's ability to measure low $p_{\rm T}$ J/ψ with good precision, thanks to its low material budget and great particle identification capabilities.

The second order event plane will be reconstructed using the EPDs which will significantly decrease the contribution from the non-flow effects and consequently the measurement's systematic uncertainties. Also, an inverse of the event plane resolution enters directly the

J/ψ v_2 uncertainty calculation. Due to the use of the EPD, the resolution of the event plane at forward rapidity for the J/ψ v_2 measurement at STAR will improve. Figure 6 presents statistical projections for the J/ψ v_2 measurement in 0–80% Au+Au collisions assuming 20 B MB events and 34 nb^{-1} of BHT trigger sampled luminosity. Both cases of the second order event plane reconstruction, using the forward EPD and mid-rapidity TPC, are considered and shown. A significant improvement in the precision of the J/ψ v_2 can be seen across the experimentally accessible J/ψ p_{T} coverage, providing the potential to distinguish among different model calculations. In addition, the larger dataset would allow to extend the measured p_{T} range beyond 10 GeV/c.

1.1.4 What is the Temperature of the Medium?

Υ suppression

In the QGP, the confining potential of a heavy quark-antiquark pair is predicted to be screened by the surrounding partons leading to the quarkonium dissociation. Within this static picture, a quarkonium state dissociates if its size is larger than the Debye screening length of the medium that is inversely proportional to the medium temperature. Consequently, different quarkonium states, depending on their sizes, are expected to dissociate at different temperatures, which is usually referred to as the quarkonium sequential suppression. Quarkonia are therefore considered excellent probes of the medium thermodynamic properties. In particular, differences in the dissociation temperatures between Υ(1S), Υ(2S) and Υ(3S) states are larger compared to the charmonium states, providing a longer lever arm. In addition, the regeneration contribution for bottomonia is expected to be negligibly small at RHIC energies.

Figure 7 presents statistical projections for Υ(1S) and Υ(2S) R_{AA} as a function of p_{T} and N_{part} (centrality), compared to STAR's latest results from the 2011, 2014 and 2016 datasets [27]. One can see a clear improvement of the statistical precision for both Υ states. Due to the larger suppression of the Υ(3S) state, only an upper limit on the R_{AA}, 0.17 at 95% confidence level, was obtained so far [27]. With an integrated luminosity of 34 nb^{-1} plus 20 B MB events, we expect a precision of about 30% for Υ(3S) that may allow us to extract the Υ(3S) signal if the meson is not fully dissociated in the medium or at least significantly improve the precision of the upper limit. The requested luminosity is therefore crucial to obtain a full picture of the bottomonia suppression at the RHIC top energy.

ψ(2S) suppression

ψ(2S) is the most loosely bounded quarkonium state currently accessible by heavy-ion experiments. Its dissociation temperature is predicted to be around, or even below, the critical temperature, and is much smaller than that of J/ψ and Υ states. It is therefore more likely to be dissociated in the early stage and in the core of the fireball, and those ψ(2S) that are measured may have significant contributions from regeneration at a later stage in the evolution of the fireball. The relative suppression of ψ(2S) and J/ψ is sensitive to the temperature profile of the fireball produced in heavy-ion collisions and its space-time evolution. It is also argued that the charmonium formation process from a $c\bar{c}$ pair may be affected by both the

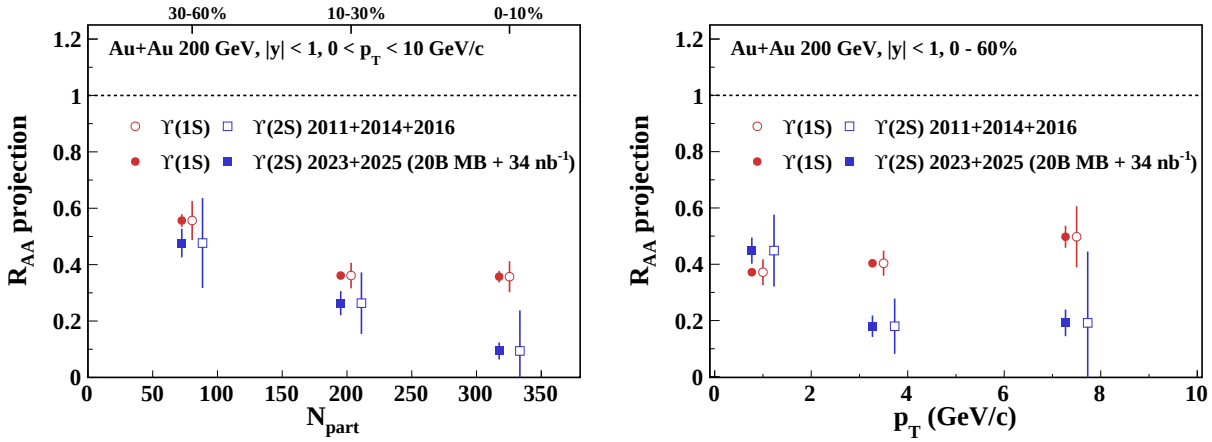

Figure 7: Statistical projections for the Υ(1S) and Υ(2S) $R_{\rm AA}$ as a function of $N_{\rm part}$ (left) and $p_{\rm T}$ (right) in 0–60% Au+Au collisions at $\sqrt{s_{\rm NN}}$ = 200 GeV, assuming 20 B MB events and 34 nb^{-1} of BHT trigger sampled luminosity. The projections (filled symbols) are compared to the STAR results from 2011, 2014 and 2016 datasets (open symbols) [27].

QGP and the initial strong magnetic field, altering the relative yields among different charmonium states. [28, 29] The measurement of ψ(2S) is much more difficult than that of J/ψ due to a much smaller production cross-section and dilepton decay branching ratio, resulting in a very low signal-to-background ratio. The ALICE Collaboration successfully measured the relative suppression of ψ(2S) and J/ψ in Pb+Pb collisions at forward rapidity [30], and the ATLAS and CMS Collaborations published the relative suppression in Pb+Pb collisions at mid-rapidity and high $p_{\rm T}$ [31, 32].

Attempts to measure ψ(2S) suppression in heavy-ion collisions at RHIC have not been successful to date. The low material budget and excellent particle identification capability of STAR together with the large data sample from Run-23+25 will provide a unique opportunity to measure the suppression of ψ(2S) at low $p_{\rm T}$ and mid-rapidity at RHIC. Figure 8 shows the projections of ψ(2S) signal and the yield ratio of ψ(2S) and J/ψ from 20 B MB events in 200 GeV Au+Au collisions. Here the ψ(2S)/J/ψ ratio is assumed to be 0.02, and the performance of detectors from existing data before STAR iTPC upgrade is used for the projection. As shown in the figure, the ψ(2S) signal significance will be around 3σ level in the 0-20% centrality bin. This significance could become even smaller depending on the level of further suppression for ψ(2S) compared to J/ψ. Despite the improvement of momentum and dE/dx resolution thanks to the STAR iTPC upgrade, it is crucial record a large data sample for a significant ψ(2S) measurement.

QGP temperature from dileptons in the IMR

The dilepton mass spectrum has many contributions, and a cocktail of known processes needs to be subtracted to find the excess radiation. To gain a deeper understanding of the microscopic origin of the excess radiation, we will

- separate early time radiation from later time radiation by measuring dilepton elliptic

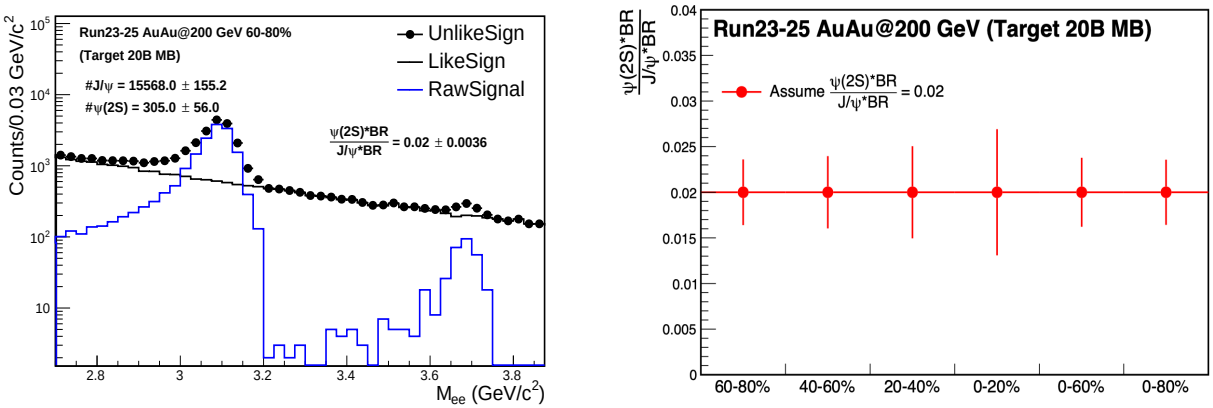

Figure 8: Projections for the J/ψ and ψ(2S) signals in 60–80% Au+Au collisions at $\sqrt{s_{\rm NN}} = 200$ GeV (left) and the ψ(2S) to J/ψ yield ratios in various centrality bins (right).

flow (v_2) as a function of dilepton mass;

- identify the source of dilepton radiation by studying dilepton polarization versus invariant mass (helicity angle);
- measure precisely the lifetime of the fireball. As an observable we will compare integrated low-mass yield to model calculations with various $\tau_{\rm fireball}$;
- extract the average radiating source temperature from the fit of a Boltzmann function to the invariant mass spectrum in the range of 1.1 - 2.5 GeV/c^2. The higher the invariant mass, the stronger the QGP contribution to the spectrum.

The dilepton intermediate mass region (IMR), between the peaks of ϕ and J/ψ, is dominated by thermal emission from the QGP. The slope of the spectrum in this region can be used as a blue-shift free measurement of the temperature at the time of dilepton emission. Extraction of the QGP temperature from the dilepton spectrum can be compared to the temperatures suggested by the Υ and ψ(2S) suppression.

Last but not least, concerning the direct photon emission, the existing difference, on the order of a factor of two, between the low momentum spectra from PHENIX and STAR in 200 GeV Au+Au collisions, needs to be resolved. In order to do so, we will carry out high-precision measurement of the direct virtual photon yield as well as its elliptic flow coefficient, which can also shed light on the so-called direct photon puzzle. In particular, we will focus on low $p_{\rm T}$ η meson measurement which might be instrumental in clarifying this long-standing question.

1.1.5 What are the Electrical, Magnetic, and Chiral Properties of the Medium?

The QGP medium which is created during the collision of two heavy ions has significant electric fields, magnetic fields, vorticity, and chirality.

Pseudorapidity dependence of global hyperon polarization ($P_H(\eta)$)

The global polarization of hyperons produced in Au+Au collisions has been observed by STAR [33]. The origin of such a phenomenon has yet to be understood. Several outstanding questions remain. How exactly is the global vorticity, and its associated strong magnetic fields, generated by the two incident heavy ions dynamically transferred to the fluid-like medium on the rapid time scales of a collision? How does the local thermal vorticity of the fluid gets transferred to the spin angular momentum (magnetic moment) of the produced particles during the process of hadronization and decay? In order to address these questions one may consider measurement of the polarization of different particles that are produced in different spatial parts of the system, or at different times. A concrete proposal is to: 1) measure the $\Lambda(\bar{\Lambda})$ polarization as a function of pseudorapidity and 2) measure it for different particles such as Ω and Ξ. Both are limited by the current acceptance and statistics available as recently published by STAR [34]. However, as shown in Fig. 9 with the addition of the iTPC and FTS as well as high statistics data from Run-23+25, it will be possible to perform such measurements with reasonable significance. iTPC has excellent PID capability

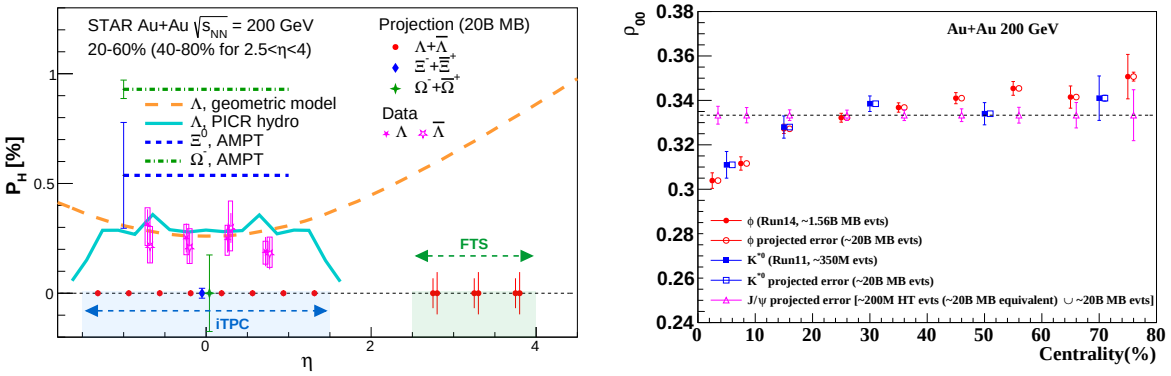

Figure 9: (Left) Projections (along with preliminary data) for differential measurements of $\Lambda(\bar{\Lambda})$ polarization over the extended range of pseudorapidity with the iTPC and FTS, which will help resolve tension between different theoretical model predictions (shown by curves) of polarization with η. In addition, projections for the measurements of spin-1/2 Ξ and spin-3/2 Ω particles are also shown. (Right) Spin alignment co-efficient ρ_{00} as a function of centrality, with projected errors. The enhanced statistics from Run-23+25, combined with the excellent dilepton capabilities of STAR, will enable us to measure J/ψ alignment and improve the significance of the ϕ and K^{*0} measurements.

to measure all these hyperons.

Although the FTS has no PID capability we can do combinatorial reconstruction of $\Lambda(\bar{\Lambda})$ candidates via displaced vertices. A similar analysis was performed and published by STAR using the FTPC [35] more than a decade ago. In order to make a projection, we assume similar momentum resolution of 10–20% for single charged tracks, similar overall tracking efficiency, charge state identification capability for the FTS and FTPC. We also assume that the FTS, with its novel tracking framework, will be able to measure a minimum separation

of 20 cm between a pair of one positive and one negative track (a possible decay vertex) from the collision vertex. This will give rise to about 5% efficiency of $\Lambda(\bar{\Lambda})$ reconstruction with about $15-20\%$ background contribution from $K^0_S \to \pi^+ + \pi^-$ [35]. With this we can make projections for a polarization measurement in 40–80% Au+Au collisions at $\sqrt{s_{\rm NN}} =$ 200 GeV within $2.5 < \eta < 4$, as shown in Fig. 9. The two different error bars correspond to lower and upper limits considering current uncertainties on the efficiency of charged track reconstruction.

Currently theoretical models predict contradictory trends for the pseudorapidity dependence of Λ polarization. If the initial local orbital angular momentum driven by collision geometry [36] plays a dominant role, it will lead to an increases of polarization with pseudorapidity. On the other hand, if the local thermal vorticity and hydrodynamic evolution [37] play a dominant role, it will predict decreasing trend or weak dependence with pseudorapidity. Such tensions can be easily resolved with the proposed measurement during Run-23 and Run-25.

Global spin alignment of J/ψ

Surprisingly large signals of global spin alignment of vector mesons such as $\phi(1020)$ and $K^{*0}(892)$ have been measured via the angular distribution of one of their decay products [38]. These experimental observations of vector meson spin alignment have yet to be interpreted satisfactorily by theory calculations. It has been realized that the mechanism driving the global polarization of hyperons can have its imprint on vector meson spin alignments albeit the observed strength of signals for the two measurements cannot be reconciled. In fact the large quantitative difference between the measurements of $\phi(1020)$ and $K^{*0}(892)$ spin alignment at low energies cannot be simultaneously explained by conventional mechanisms of spin-orbit coupling, driven by angular momentum, without invoking strong force fields [38]. It is argued that the strong force field makes a dominant contribution to the spin-alignment coefficient ρ_{00} of ϕ, while for K^{*0}, the contribution is diminished due to the mixing of quark flavors (averaging-out of different meson fields) [39, 40]. Therefore, the current experimental data from STAR [38] supports the role of strong force field as a key mechanism that leads to global spin alignment.

An extended test of such a prediction can be performed by measuring the spin alignment of J/ψ. This is because similar arguments apply for J/ψ, i.e. like s and $\bar{s}$, the strong field component also couples to c and $\bar{c}$ quarks leading to large ρ_{00} for J/ψ. ALICE recently reported $\rho_{00} \approx 0.37$ for J/ψ at forward rapidity ($2.5 < y < 4$) with a 3.9σ significance, seemingly supporting this argument. STAR can definitely contribute to this study by measuring J/ψ global spin alignment at midrapidity with the large dataset to be taken during Run-23+25.

In Fig. 9 we present the projected uncertainties for ρ_{00} of J/ψ estimated for various centralities assuming: 1) 20 B min-bias events for low $p_{\rm T}$ J/ψ measurements and, 2) 200 M BHT triggered events for the high $p_{\rm T}$ J/ψ. It is worth to mention that apart from J/ψ spin alignment, such a large statistics dataset will also allow addition differential study of global spin alignment of ϕ and K^{*0} and help to further elucidate the mechanism behind vector

meson spin alignment.

Probing electromagnetic effect via charge-dependent directed flow

One of the features in high energy heavy-ion collisions is the generation of an ultra-strong magnetic field, which is predicted to have the strength of 10^{18} Gauss [41–45]. The interplay between magnetic field and QGP may induce many interesting phenomena, such like the CME and CMW. Recent studies suggest that the charge dependent directed flow can be used to search for magnetic field related effects [46, 47], which predict a negative $\Delta dv_1/dy$ between positively and negatively charged particles due to the influence of electromagnetic field. Some experimental efforts have been made for searching this effect, such as the charge dependent v_1 measurements presented by LHC-ALICE collaboration [48], and the directed flow of D^0 and $\overline{D^0}$ from STAR experiment [49]. Results of light flavors in Pb+Pb collisions at $\sqrt{s_{\rm NN}} = 5.02$ TeV show large discrepancy to theoretical calculations, which gives an order of magnitude larger and positive Δv_1 slope. Similar results have been obtained in Au+Au collisions at several energies at RHIC, which measured positive Δv_1 slope between proton and anti-proton in semi-central collisions owning to the transported quark contributions.

Recent analyses in Au+Au and isobar collisions at $\sqrt{s_{\rm NN}} = 200$ GeV show striking centrality dependence of the Δv_1 slope. It was found that the $\Delta dv_1/dy$ between proton and anti-proton changes from positive to negative as centrality goes from central to peripheral. The negative value in peripheral collisions, with the significance of 5σ, qualitatively agrees with theoretical calculations. However, the $\Delta dv_1/dy$ between K^+ and K^-, π^+ and π^- are less significant because of the limitation of statistics. With 20 B events in Au+Au collisions at 200 GeV to be collected, the $\Delta dv_1/dy$ between K^+ and K^- can achieve a significance $> 5\sigma$, as illustrated in left panel of Fig. 10. Moreover, the EM-field prediction shows a non-trivial $p_{\rm T}$ dependence, but this measurement is currently limited by statistics. As illustrated in the right panel of Fig. 10, with the data accumulated from Run-23+25, we will be able to measure the $p_{\rm T}$ dependence of $\Delta dv_1/dy$ with higher precision.

The existing measurements of v_1 for Ξ and Ω in Au+Au collisions at $\sqrt{s_{\rm NN}} = 200$ GeV have large uncertainties. There is a hint of a large v_1 for Ω baryons from recent measurements, however, as shown in Fig. 11, the statistical uncertainties of the current STAR measurements are large. There are also measurements for electric charge and strangeness dependent splittings in Au+Au collisions at $\sqrt{s_{\rm NN}} = 200$ GeV. These measurements also suffer from insufficient statistics, as shown in Fig. 12. A large dataset from the upcoming Run-23 and 25 for Au+Au collisions at $\sqrt{s_{\rm NN}} = 200$ GeV will definitely help improve the precision of these measurements. The projected statistical precision, based on 20 B events to be collected Run-23+25, are shown in Figs. 11 and 12.

Chiral properties: ρ-a_1 mixing

In case the measured in-medium spectral function merges into the QGP description, it would indicate a transition from hadrons into a structure-less quark-antiquark continuum, thus providing the manifestation of chiral symmetry restoration. We will continue to search for a direct signature of chiral symmetry restoration via chiral ρ-a_1 mixing.

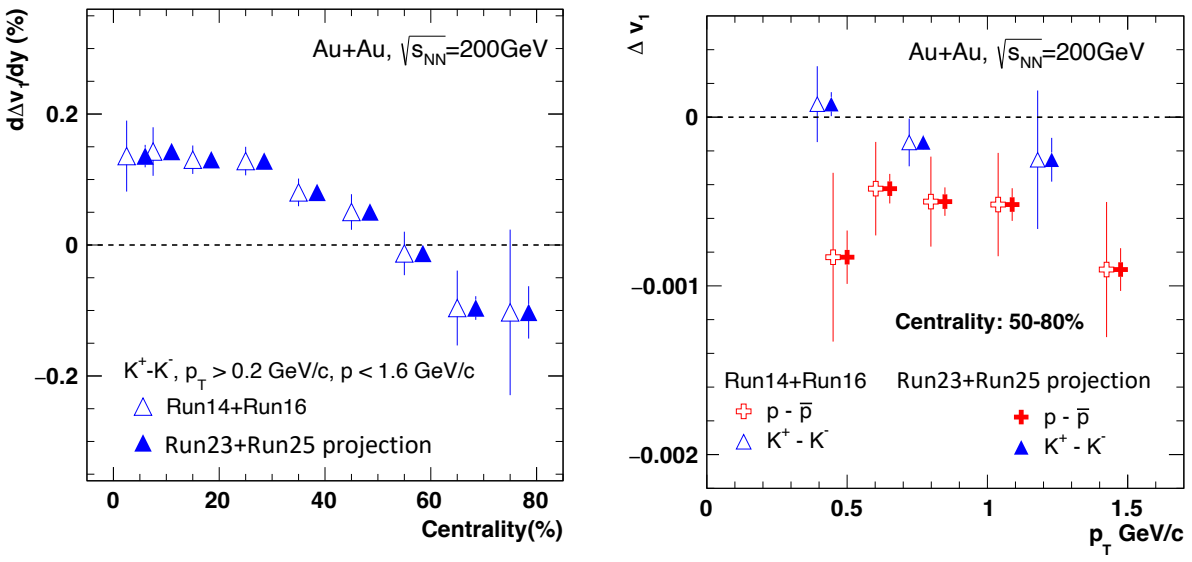

Figure 10: (Left) $\Delta dv_1/dy$ between K^+ and K^- as a function of centrality in Au+Au collisions at $\sqrt{s_{\rm NN}}$ = 200 GeV. Open markers indicate the projected results. (Right) $\Delta dv_1/dy$ for proton and kaon as a function of $p_{\rm T}$ in 50–80% Au+Au collisions at 200 GeV.

The signal is predicted to be detectable in the dilepton intermediate mass range. Difficulties are related to the fact that correlated charm-anticharm decays and QGP emission saturate this invariant mass region of 1.1 — 1.3 GeV/c^2. Therefore an accurate measurement of the excess dilepton yield, i.e. dilepton yield after subtraction of the cocktail of contributions from final-state decays, Drell-Yan and those from correlated heavy-flavor decays, up to invariant mass of 2.5 GeV/c^2 is required. Deeper understanding of the origin of the thermal radiation in Au+Au collisions at $\sqrt{s_{\rm NN}}$ = 200 GeV from ∼zero mass up to 2.5 GeV/c^2 will become possible with rigorous theoretical efforts and improved dielectron measurements. Figure 13 shows the expected statistical and systematic uncertainties of the dielectron excess mass spectrum with all the detector upgrades taken into account and for the anticipated statistics of 20 B events.

Electrical conductivity (dielectron LMR)

Another application of dielectron continuum is to measure transport coefficients. The electrical conductivity can be directly obtained as the low-energy limit of the EM spectral function. We aim to extract such information by studying excess dielectron yields at the low-energy regime of the dilepton spectra and the conductivity peak at small invariant masses, i.e. at low invariant mass and low $p_{\rm T}^{ee}$. Measurement of the Drell-Yan process in p+Au collisions at low $p_{\rm T}$ would provide an important reference to constrain the dilepton cocktail.

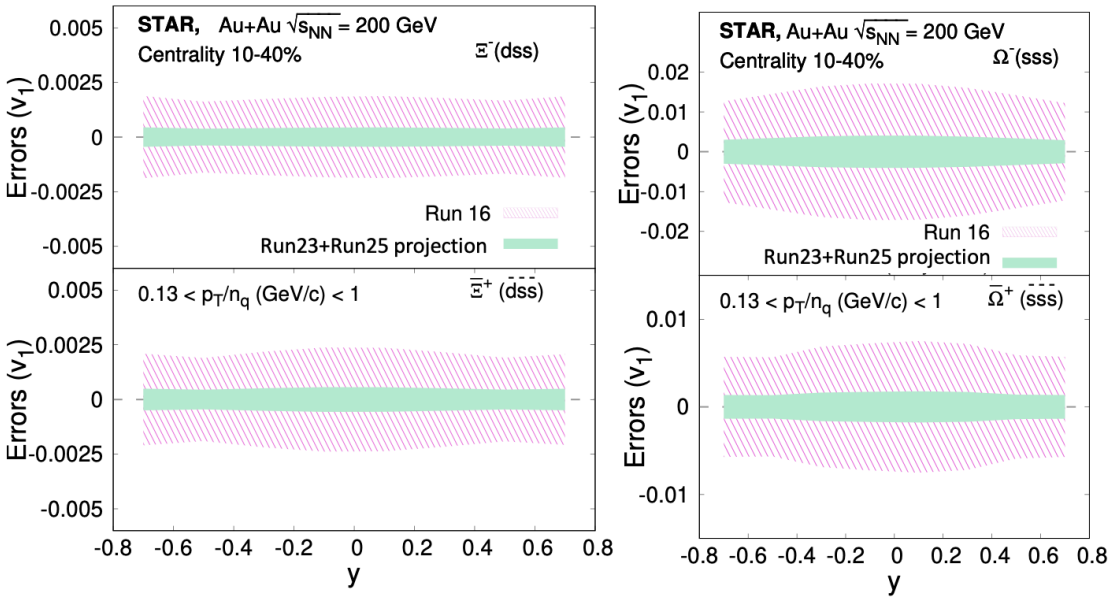

Figure 11: Projection of directed flow (v_1) error for Ξ^-, $\overline{\Xi}^+$, Ω^- and $\overline{\Omega}^+$ as a function of rapidity (y) in 10–40% central Au+Au collisions at $\sqrt{s_{\rm NN}}$ = 200 GeV. The projections are made by assuming 20 B MB events to be collected in Run-23+25.

Local parity violation and the chiral magnetic effect

A decisive experimental test of the Chiral Magnetic Effect (CME) has become one of the major scientific goals of the heavy-ion physics program at RHIC. The existence of CME would be a leap towards an understanding of the QCD vacuum, establishing a picture of the formation of a deconfined medium in which chiral symmetry is restored, and it would

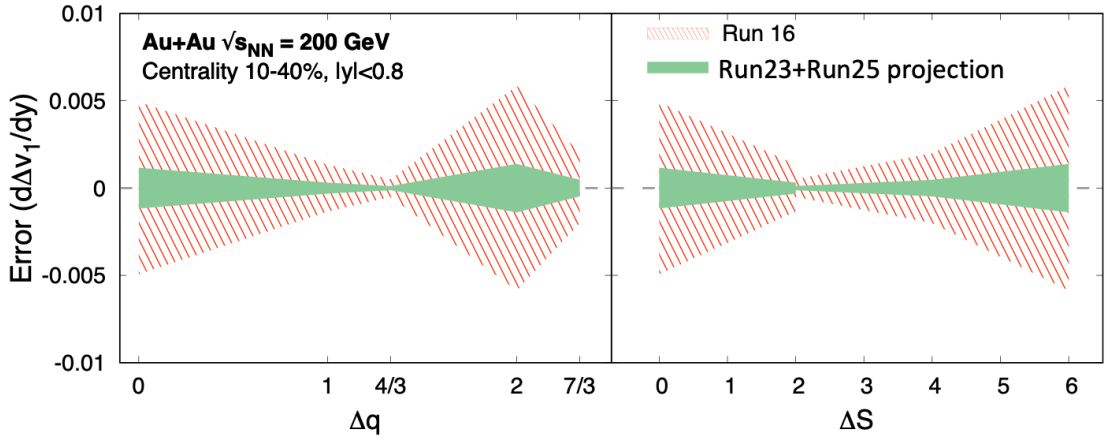

Figure 12: Δv_1 slope ($d\Delta v_1/dy$) error at mid-rapidity as a function of electric charge difference (Δq) and strangeness difference (ΔS) for 10-40% centrality in Au+Au collisions at $\sqrt{s_{\rm NN}}$ = 200 GeV. The projections are made assuming 20 B events to be collected in Run-23+25.

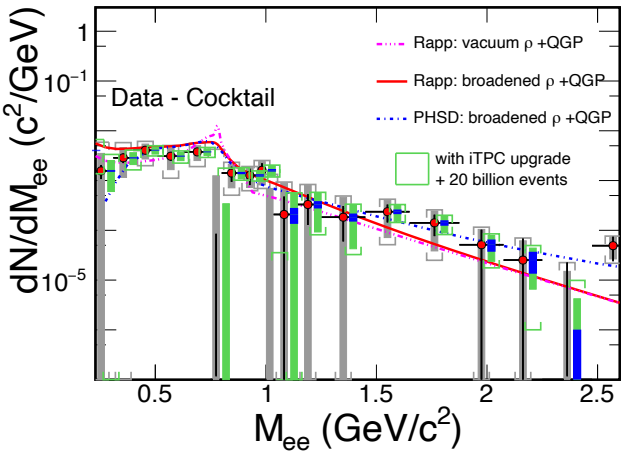

Figure 13: The expected statistical and systematic uncertainties on the dielectron excess mass spectrum with the iTPC upgrade compared to the current TPC case. Data are from current measurements in $\sqrt{s_{\rm NN}}$ = 200 GeV Au+Au collisions [50]. Model comparisons are also shown. The boxes represent systematic uncertainties from data and the brackets represent the total systematic uncertainties including those from cocktails. The grey ones are for the current case while the green ones are for the Run-23 and 25 case. The blue bands represent statistical uncertainties from 20 B min-bias events with the iTPC upgrade.

also provide unique evidence that the strongest known electromagnetic fields are created in relativistic heavy-ion collisions [51,52]. The impact of such a discovery would go beyond the community of heavy-ion collisions and will possibly be a milestone in physics. The remaining few years of RHIC running and analyses of previously-collected data will likely provide the only chance for CME searches in heavy-ion collisions in the foreseeable future.

The isobar collisions provided an unique opportunity to search for the CME because of the $\sim$ 15% difference in B^2 and hence the CME correlation signals between Ru+Ru and Zr+Zr collisions. However, no clear CME signal has been observed in isobar data even with an improved understanding of the baseline. The signal-to-background ratio is expected on general ground to be smaller in isobar collisions than in Au+Au collisions by an approximately factor of 3 [53]. This is in line with the Au+Au results which indicate a positive CME signal of $\sim$ 8% with $\sim 2\sigma$ significance using the spectator/participant plane method [54]. The size of the current Au+Au data sample is about 2.4 B events from Run-11, Run-14 and Run-16 [54]. In order to achieve 5σ significance with the same analysis technique, one needs to have about 15 B events. Therefore, with the proposed 20 B events to be collected by STAR during Run-23 and 25, one can achieve more than 5σ significance provided the possible CME signal remains at 8%. A stringent upper limit will be possible on the CME if the size of the signal turns out to be smaller. This rough estimate does not account for two important facts that can lead to higher significance though. The first is that the iTPC upgrade enhances the charge particle multiplicity by 50% and therefore triplet($\sim dN/d\eta^3$) (pair $\sim dN/d\eta^2$) statistics by a factor of 3.4 (2.3). The second one is the addition of the EPD detector which will significantly reduce nonflow contaminations in the measurements

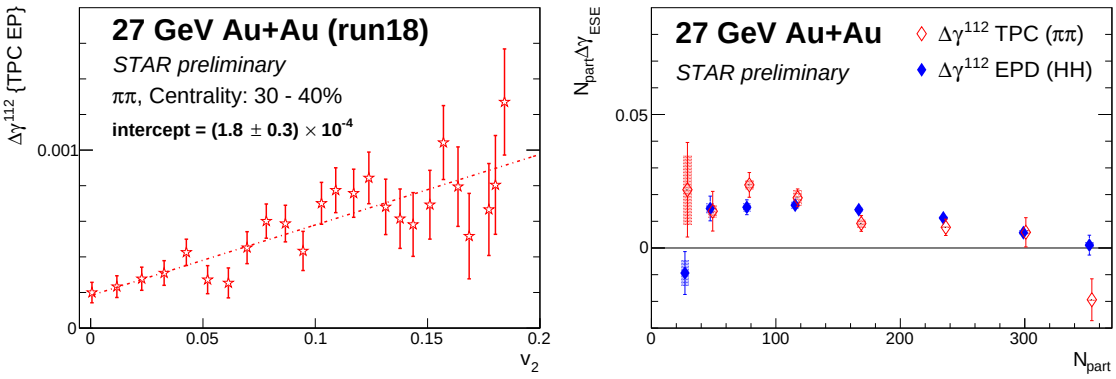

Figure 14: (Left) $\Delta\gamma_{112}$ for π-π vs v_2 measured with the TPC event plane in 30–40% Au+Au collisions at 27 GeV. (Right) $\Delta\gamma_{112,\mathrm{ESE}}$ scaled by N_{part} as a function of N_{part} for π-π using the TPC event plane, and for hadron-hadron using the EPD event plane in Au+Au collisions at 27 GeV.

with respect to the participant plane. Our estimate assumes that the systematic uncertainty can be controlled to be smaller than the statistical uncertainty, i.e. below 1%.

Another technique used to search for the CME is based on the event-shape engineering (ESE). The dominant background in the CME-sensitive $\Delta\gamma_{112}$ correlator is caused by the coupling of elliptic flow with other mechanisms such as resonance decays and local charge conservation. The ESE method aims to project $\Delta\gamma_{112}$ to a class of events with minimal flow to suppress the v_2-related background. We adopt an ESE technique [55] that uses the flow vector ($q_{2,x} = \frac{1}{\sqrt{N}}\sum_i^N \cos(2\phi_i)$, $q_{2,y} = \frac{1}{\sqrt{N}}\sum_i^N \sin(2\phi_i)$) to select spherical sub-events with almost zero v_2. Observables like v_2 and γ_{112} are measured as a function of q_2^2 from the particles of interest (POIs), and then $\Delta\gamma_{112}$ is plotted against v_2 in the same q_2^2 interval to yield a reliable projection to the zero-flow mode. Figure 14 (left) demonstrates the application of the ESE approach to the STAR data of 30–40% Au+Au collisions at 27 GeV (run 2018). The decrease of $\Delta\gamma_{112}$ for π-π with decreasing v_2 illustrates how the v_2-related background is suppressed. Figure 14 (right) shows the centrality dependence of N_{part} $\Delta\gamma_{112\mathrm{ESE}}$ for π-π using the TPC event plane, and for hadron-hadron using the EPD event plane in Au+Au collisions at 27 GeV. The ESE method will be applied to the 200 GeV Au+Au data from Run-23 and Run-25. With the large dataset of anticipated 20 B events, we will be able to perform more differential measurements and involve identified particles such as kaons and protons.

Event-by-event correlations between CME charge separation and other parity-odd features of the event will also be studied. One such analysis is motivated by the idea that the local parity violation (characterized in each event by a net topological charge Q) that is expected to couple with the spectator-produced magnetic field to give rise to the CME should also cause a net helicity of $\Lambda(\bar{\Lambda})$ in the event. Importantly, even though both of these parity-odd signatures switch handedness event-by-event, in any given event they should have the same handedness and so can be compared. Specifically, a measured event-by-event correlation between Δa_1 and ΔN would be strong evidence for the CME and underlying local

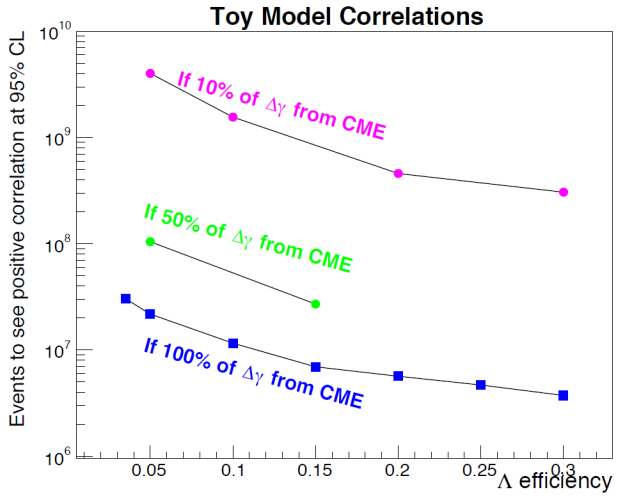

Figure 15: Estimation of the number of events required to see positive correlation between net Λ helicity and out-of-plane charge separation sensitive to local parity violation at the 95% confidence level, plotted against the efficiency of $\Lambda(\bar{\Lambda})$ reconstruction (see Ref. [57] for details).

parity violation. Note also that the flow-related backgrounds that plague charge-separation measurements are not expected to affect ΔN and so should not affect such correlation measurement. We use a similar toy model to estimate the number of events needed to see non-zero correlations between Δa_1 and ΔN with different CME signal fraction in the $\Delta\gamma$ measurement (see Fig. 15). The main unknown in this estimate is the extent to which strange quarks may be counted as light quarks and so will have a net handedness imparted by the parity-odd domain. Recent theoretical work [56] makes a direct connection between the net lambda helicity and the axial chemical potential developed from local parity violation. Figure 15 suggests that this will be a topic requiring the large datasets of Run-23+25. To better understand this correlation, we have analyzed the Run-18 Au+Au collision data at $\sqrt{s_{\rm NN}} =$ 27 GeV [58]. The $\Lambda(\bar{\Lambda})$ baryons are reconstructed by their decay daughter tracks and identified by the `KFParticle` package. Each Λ handedness is estimated by decay kinematics. After a purity correction, $N_{\rm L}$ and $N_{\rm R}$ are calculated for both Λ and $\bar{\Lambda}$ in each event, and then Δn (normalized ΔN, $\Delta n = \frac{N_{\rm L}-N_{\rm R}}{\langle N_{\rm L}+N_{\rm R}\rangle}$) is calculated. The observable Δa_1 can be calculated from primordial particles' azimuthal angles w.r.t. the first-order EP measured by the EPD. The covariance between Δn and Δa_1 is then calculated for the event sample. In this exploratory measurement, the covariance is consistent with zero, and so no significant correlations have been observed (see Fig. 16). However, this event-by-event correlation method holds great potential with future high statistics data from Run-23+25 by a qualitatively new technique different from all existing analyses.

1.1.6 What are the Underlying Mechanisms of Jet Quenching?

The dependence of jet energy loss on the jet $p_{\rm T}$ and/or resolution or angular scale tagged by jet substructure observables are key tools in discriminating various jet quenching mech-

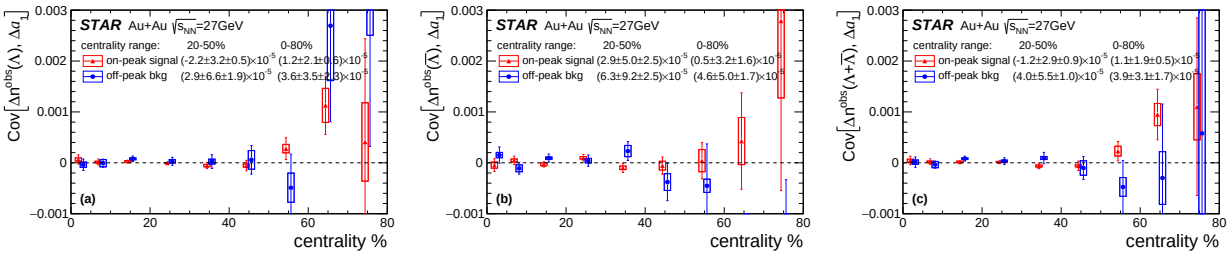

Figure 16: The covariance between Δa_1 and Δn for Λ (Left), $\bar{\Lambda}$ (Middle), and the sum of them (Right) as a function of centrality [58]. The red markers come from the $\Lambda(\bar{\Lambda})$ mass peak region with purity correction and blue markers come from the side bands for background.

anisms [59–62]. In addition, the measurement of jet acoplanarity is a sensitive probe of p_{T} broadening and medium response [63], particularly for jets at low p_{T} which are accessible at STAR by selecting a given momentum transfer via a photon trigger. Such a measurement is also affected by background arising from vacuum Sudakov radiation at RHIC energies [64,65].

STAR's unique geometry allows collection of events over a wide range of vertex positions along the beam direction (vz) for jet analyses, thereby efficiently sampling the provided RHIC luminosity. Optimization of the vz range used in the various analyses involves a balance between statistical precision and complexity of corrections, with the latter predominantly contributing to the systematic uncertainties of the measurement. Recent STAR jet measurements in Au+Au collisions have employed two classes of vz cuts: the inclusive charged-particle jet analysis [66] utilizes $|\mathrm{vz}| < 30$ cm, whereas the $\gamma_{\mathrm{dir}}+$jet analysis utilizes $|\mathrm{vz}| < 70$ cm. With the $\gamma_{\mathrm{dir}}+$jet measurement successfully utilizing the broad vz range with controlled systematic precision, we are exploring similar event selections maximizing the available statistics for future jet measurements, including the inclusive/differential jet analyses. In the following discussions, we assume an integrated luminosity of 34 nb^{-1} plus 20 B min-bias events, which is roughly a factor 3.7 increase in trigger statistics relative to the current analyses based on Run-14 data.

To quantify the effect of the marked increase in statistics, we utilize two mature jet measurements and discuss their expected improvements. These analyses are the semi-inclusive distribution of charged-particle jets recoiling from a high-E_{T} direct-photon trigger (γ_{dir}+jet); and the differential measurement of energy loss for jet populations selected by varying a substructure metric. Since these analyses are mature, their analysis methodologies and correction schemes are optimized, so that their projections based on increased statistics are meaningful.

Semi-inclusive $\gamma_{\mathrm{dir}}+$jet measurements (I_{AA})

Figure 17 shows I_{AA} for fully-corrected semi-inclusive distributions of charged-particle jets (anti-k_{T}, $R = 0.5$) recoiling from a direct-photon trigger with $15 < E_{\mathrm{T}} < 20$ GeV in 0–15% central Au+Au collisions at $\sqrt{s_{\mathrm{NN}}} = 200$ GeV, for the current analysis based on 10 nb^{-1} [67] within $|\mathrm{vz}| < 70$ cm. The projected uncertainties, accounting for the Au+Au data

from previous years and Run-23+25 as well as the projected p+p statistics from Run-24, are shown in green bands. Significant reduction in the uncertainty is seen resulting from the increase in integrated luminosity, together with a significant increase in kinematic reach as indicated by the extended green band along the x-axis.

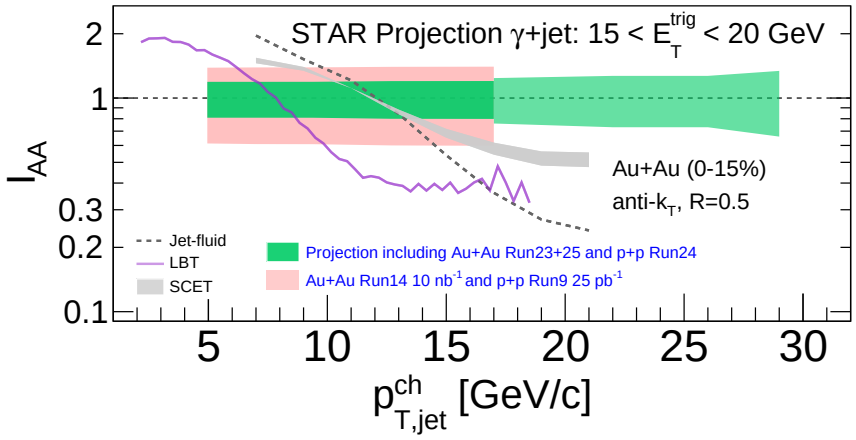

Figure 17: Projections of the I_{AA} for semi-inclusive anti-k_{T}, $R = 0.5$ jets recoiling from a direct-photon trigger with $15 < E_{\mathrm{T}} < 20$ GeV for central (0-15%) Au+Au collisions at $\sqrt{s_{\mathrm{NN}}} = 200$ GeV. The colored bands show the cumulative uncertainties for the current analysis and projections for future analysis with the higher statistics datasets.

Jet acoplanarity

The p_{T} broadening due to medium effects not only modifies the shape but also introduces a decorrelation between the di-jet angular distributions. The vacuum QCD process (Sudakov radiation) makes such measurements challenging in heavy-ion collisions, but at RHIC the Sudakov effect is smaller than that at the LHC as it depends on the virtuality Q^2 [64, 65]. A detailed study is needed to understand both effects (medium-induced and vacuum radiation) in a wide range of jet $p_{\mathrm{T,jet}}$ both at RHIC and the LHC energies.

In this direction, the STAR experiment has reported the first signature of medium-induced acoplanarity in central Au+Au collisions. However, due to limited available statistics, current preliminary result is limited to γ_{dir} and π^0 triggers of $11 < E_{\mathrm{T}} < 15$ GeV and charged-particle jets (anti-k_{T}, $R = 0.2$ and 0.5) of $10 < p_{\mathrm{T,jet}}^{\mathrm{ch}} < 15$ GeV/c. To have a better understanding of the nature of this acoplanarity, we need to extend both $E_{\mathrm{T}}^{\mathrm{trig}}$ and recoil jet $p_{\mathrm{T,jet}}$ kinematic ranges which demands high statistics datasets. On the other hand, the STAR experiment also reported the same measurement in p+p collisions to study the effect of Sudakov radiation in vacuum and set the baseline for Au+Au collisions. Figure 18 shows the semi-inclusive distributions of the azimuthal separation between a direct-photon trigger with $15 < E_{\mathrm{T}} < 20$ GeV and a charged-particle jet (anti-k_{T}, $R = 0.5$) with $10 < p_{\mathrm{T,jet}}^{\mathrm{ch}} < 15$ GeV/c in p+p (left) and 0–15% central Au+Au (right) collisions at $\sqrt{s_{\mathrm{NN}}} = 200$ GeV. The azimuthal smearing of this observable due to uncorrelated background is small, and such acoplanarity measurements are therefore strongly statistics limited [68, 69]. The grey ver-

tical bars represent the statistical uncertainty with the current available statistics, whereas the red vertical bars correspond to statistics including Run-23, 24, and 25 datasets.

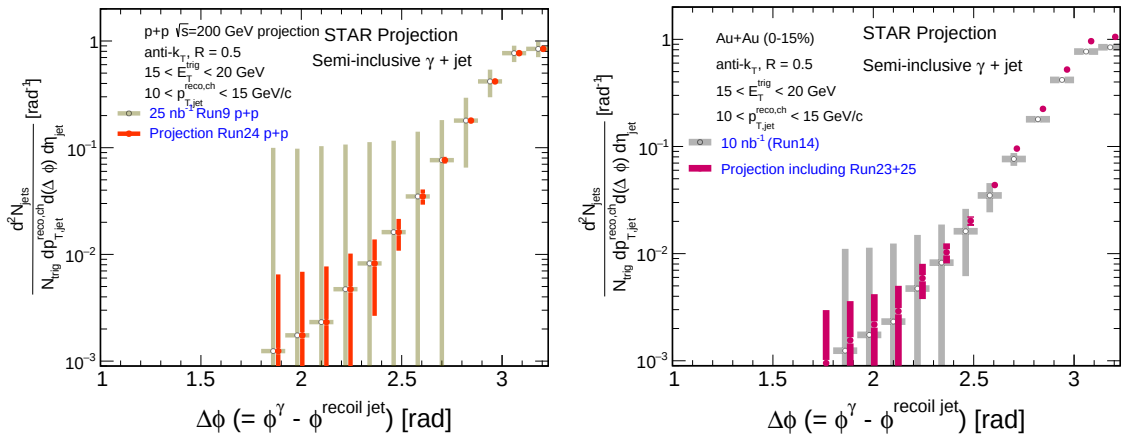

Figure 18: Projections of the acoplanarity for semi-inclusive anti-k_{T}, $R = 0.5$ jets of $10 < p_{\mathrm{T,jet}}^{\mathrm{ch}} < 15$ GeV/c recoiling from a direct-photon trigger with $15 < E_{\mathrm{T}} < 20$ GeV in p+p (left) and 0–15% central Au+Au (right) collisions at $\sqrt{s_{\mathrm{NN}}} = 200$ GeV. The vertical bands show the statistical uncertainties for the current analysis and projections for future analysis with the high statistics datasets.

It is worth noting that this measurement in p+p collisions could exploit forward triggering using forward calorimeter to explore a relatively small x region, compared to mid-rapidity measurement. This is important to study various pQCD effects like NLO corrections, ISR/FSR, and MPI effects, and upcoming Run-24 p+p collision data-taking is critical in this direction.

Differential measurement of energy loss tagged with a substructure metric

Systematic exploration of parton energy loss controlled for variations in the jet shower forms an integral part of the jet program at STAR. Since parton showers are inherently probabilistic, a jet population contains patterns of radiation varying in both angle and momentum scales which can be extracted via jet substructure measurements defined based on jet constituents' angle and/or momentum via algorithms or correlations. By selecting jets based on their substructure, STAR can differentially measure jet-medium interactions for various types of energy loss e.g. color coherence, dead cone, etc. In other words, part of the STAR jet program for Run-23+25 will focus on jet substructure as a jet-tagger.

Theory calculations show significant differences between energy loss signatures for jets perceived by the medium as a single or multiple color charges [61]. The integrated luminosity from the Runs 23 and 25 datasets not only provide a substantial increase in statistics in the current measurements of jet substructure, they also increase the available phase space for rare processes such as wide angle emissions from high-p_{T} jets. This enables STAR to extend the current measurements of differential energy loss from a resolution of $\delta\theta = 0.1$ to finer

resolution $\delta\theta \approx 0.025$ in the jet opening angle as shown in Fig. 19, and also extend to jets of higher momenta. By extending to high energy splittings within jets at varied opening angles, we can probe earlier formation times whereby vacuum-like emissions and medium induced radiations are expected to occur.

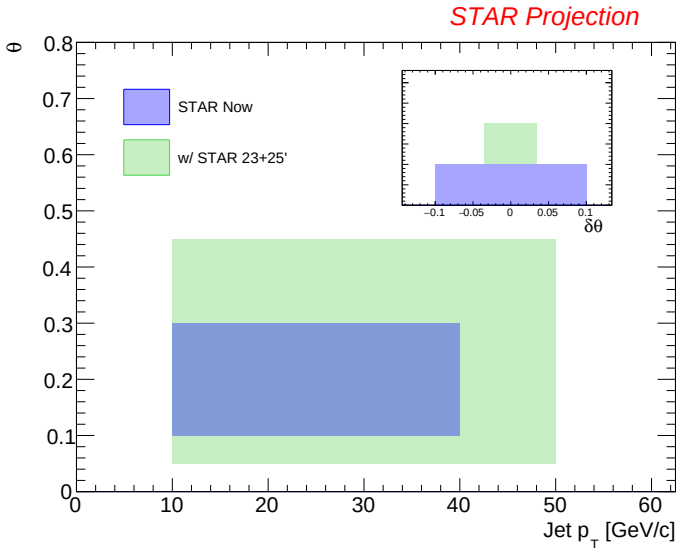

Figure 19: The subjet opening angle as a function of jet $p_{\mathrm{T,jet}}$ in 0-20% central Au+Au collisions. The inset is the corresponding resolution of θ. Blue and green represent current (10 nb^{-1}) and future (including Run-23 and 25) analyses, respectively.

Given the unique nature of jet-medium interactions at RHIC, with the jet and sub-jet scales sufficiently closer to the medium scale than the LHC, the aforementioned measurements bolster the importance of the STAR jet program with the goal of extracting the microscopic properties of the QGP.

1.1.7 What is the Nature of the Phase Transition Near $\mu_B = 0$?

Lattice-QCD calculations [70,71] predict a sign change in the susceptibility ratio χ_6^B/χ_2^B with temperature (T) taking place in the range of 145-165 MeV at $\mu_B = 0$. The observation of this ratio going from positive to negative values is considered a signature of a crossover transition. Interestingly, values of net-proton C_6/C_2 are found to be systematically negative from peripheral to central 200 GeV Au+Au collisions within large statistical uncertainties [72]. The hint of negative C_6/C_2 is intriguing, but the current result has less than 2.3σ significance for 30-40% centrality in terms of statistical uncertainties. The systematic uncertainty is of similar magnitude as the statistical uncertainty. As shown in the projection plot of Fig. 20, it is possible to establish a definitive observation of negative C_6/C_2 at 200 GeV with 20 B minimum-bias events to be collected during Run-23 and 25 and taking into account an expected 15% increase in the reconstruction efficiency and enhanced acceptance thanks to the iTPC upgrade. A similar measurement can be performed at the LHC for vanishing

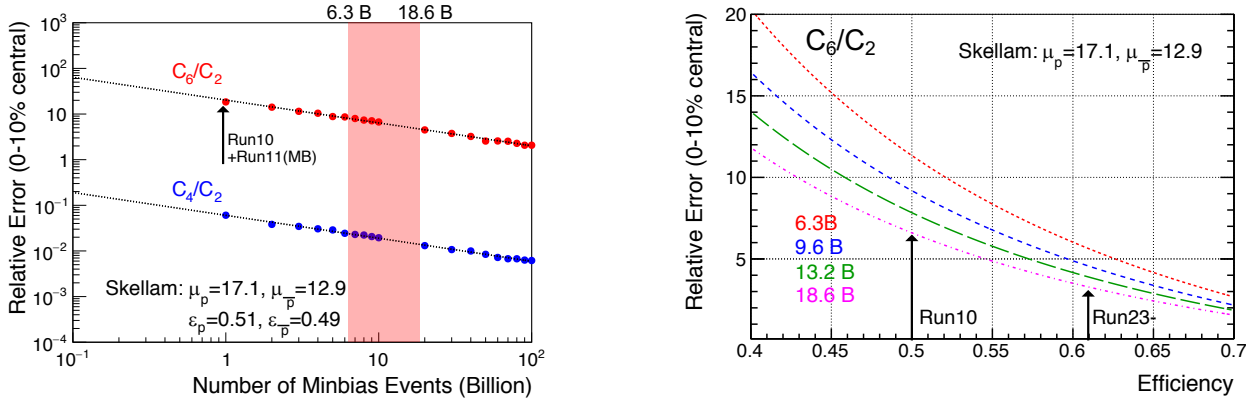

Figure 20: Projection for measurement of ratio of sixth order over second order cumulants of net-proton distribution.

baryon chemical potential, while only STAR measurements can explore the finite $\mu_{\rm B}$ region. Our measurement at $\sqrt{s_{\rm NN}} = 200$ GeV has the potential to establish the first experimental observation of QCD chiral crossover transition at $\mu_{\rm B} \approx 20$ MeV.

1.1.8 What Can We Learn About the Strong Interaction?

The strong interaction between baryons leads to a residual force; the most common example is the force between a nucleon and a hyperon (NY). The same force is responsible for binding n-p into d. So far, understanding the strong interaction has been limited to the effective theories related to nucleons and the scattering experiments, which are very challenging due to the short lifetime of those baryons (a few cm decay length). One of the current challenges is to evaluate the strong interaction between hyperons, as very little is known experimentally about NY and YY interactions. Hypernuclei (a hyperon bound inside an atomic nucleus) are proof of attractive interaction of NY. Measurements of NN and NY interactions have crucial implications for the possible formations of bound states. Studies of the strong interaction potential via two-particle correlations in momentum space measured in relativistic heavy-ion and elementary collisions have proven to be useful in gaining access to the interactions between exotic and rare particles. Possible combinations can be: $p\Lambda$, $p\Sigma$, $p\Omega$, $p\Xi$, $\Lambda\Lambda$, $\Xi\Xi$. In contrast to $p\Lambda$, the nature of $p\Sigma$, $p\Omega$, $\Lambda\Lambda$ still need experimental verification. Even if scattering experiments are available, they are not very conclusive.

Figure 21 shows the preliminary $p\Xi$ correlation function. All available statistics, 3 B events accumulated overall previous runs were used for the $p\Xi$ and $p\Omega$ cases. Combining datasets from different years leads to run-to-run variations, resulting in large systematic uncertainties in the detector responses. A long run with similar detector conditions during Run-23 and 25 will avoid such issues. Statistical uncertainties of the current measurements remain large, and the number of points used to build the correlation function is minimal. This means that the current results are not precise enough to study the strong interaction parameters in detail. The collection of 20 B events will make possible the construction of

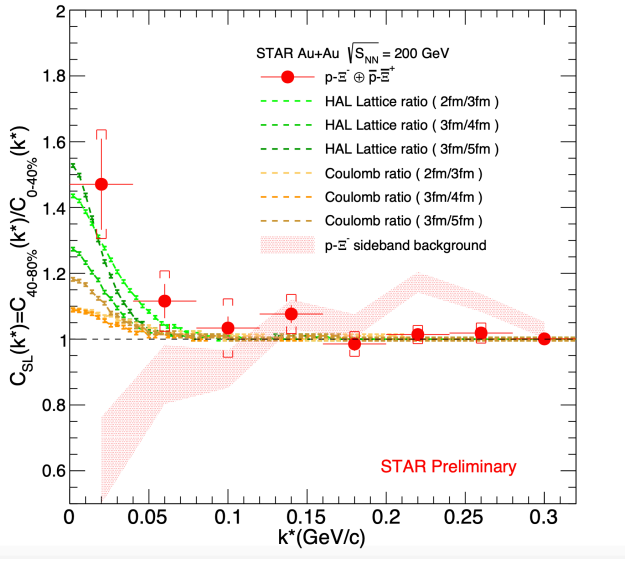

Figure 21: Solid circles represent the ratio (R) of the small system (40-80% collisions) to the large system (0-40% collisions) for proton–Ξ and $\bar{p}$–Ξ correlations. The bars correspond to the statistical uncertainties. The shaded area represents R for background candidates from the side band of the Ξ invariant mass distribution. Coulomb-induced R are shown in yellow and orange colors. HAL Lattice predictions of R are shown in green.

correlation functions of the $p\Xi$ case with double the number of points and smaller statistical uncertainties than the current measurement. The $p\Omega$ system is even more statistics-hungry. Previous STAR measurements of $p\Omega$ correlations show that the parameters of the strong interaction can be barely studied. More precise and detailed studies would require the large dataset to be collected in Run-25.

The description of the $\Lambda\Lambda$ interaction is still an open issue. Such a description is fundamental since it plays a decisive role in understanding the nature of hyperons that appear in neutron stars. If many hyperons appear close to each other and their fraction becomes significant, the YY interactions are expected to play an essential role in describing the equation of state of the dense system. Figure 22 shows preliminary $\Lambda\Lambda$ (left) and $\Xi\Xi$ (right) correlation functions. For current $\Lambda\Lambda$ and $\Xi\Xi$ measurements, data from all previous runs were combined, which also suffers from aforementioned run-to-run variations. The expected large sample of 20 B events is more critical for the $\Xi\Xi$ analysis, and it will enable the reduction of statistical uncertainties significantly and makes it possible to determine parameters of the strong interaction with high precision. Having this large dataset will also allow the hypotheses about possible bound states to be tested. Figure 23, left panel, shows error projections for the correlation functions of $\Lambda\Lambda$ combined with $\bar{\Lambda}\bar{\Lambda}$ and $\Xi\Xi$ with $\bar{\Xi}\bar{\Xi}$ assuming at least 2 correlated particles in the event. Compared to the results based on Run-11, Run-14, and Run-16 datasets, the relative statistical errors are expected to decrease by about a factor of 4 to 5 using Run-25 data. The reduction of the statistical uncertainties for the lowest

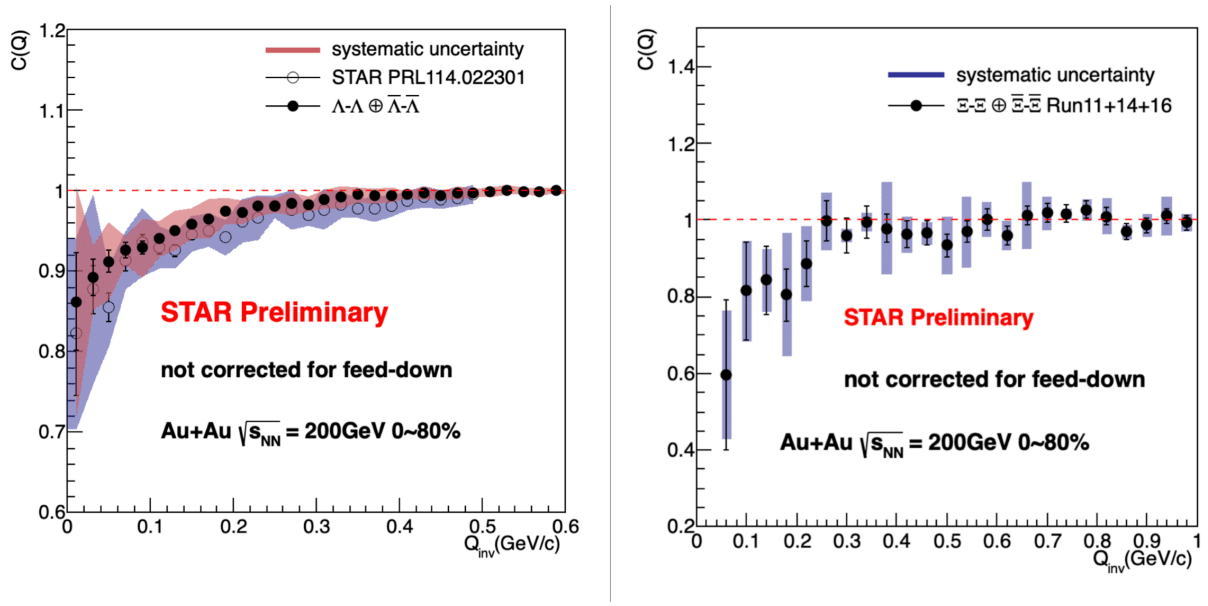

Figure 22: Left: combined $\Lambda\Lambda$ and $\bar{\Lambda}\bar{\Lambda}$ preliminary correlation functions with systematic uncertainties compared with published results. Right: combined $\Xi\Xi$ and $\bar{\Xi}\bar{\Xi}$ correlation functions with systematic uncertainties.

relative pair momentum is shown in the right panel of Fig. 23.

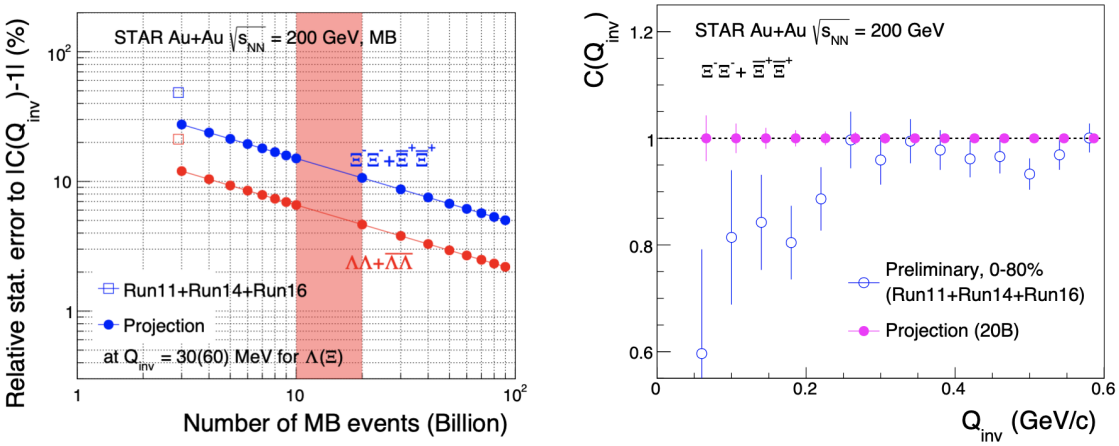

Figure 23: Left: error projections for $\Lambda\Lambda$ together with $\bar{\Lambda}\bar{\Lambda}$ and $\Xi\Xi$ together with $\bar{\Xi}\bar{\Xi}$ as a function of event statistics. Right: Error projections for $\Xi\Xi$ together with $\bar{\Xi}\bar{\Xi}$ as a function of $Q_{\rm inv}$.

1.2 Ultra-Peripheral Collisions

One of the most important scientific goals in high-energy nuclear physics is to understand the nuclear structure under extreme conditions. Thanks to ultra-relativistic heavy-ion collider facilities, e.g., the Relativistic Heavy-Ion Collider, one direction is to create a system that has

an extremely high temperature of partons, and study its deconfined properties of strongly interacting quarks and gluons. However, the other direction is to reveal the property of nucleons and nuclei before such violent collision happens, where the initial-state dynamics inside these particles may provide ultimate understanding of the Quantum Chromodynamics (QCD) in generating the visible matter. These two aspects are usually known as the heavy-ion hot Quark-Gluon-Plasma (QGP) physics and cold QCD physics, respectively. Both of them are indispensable building blocks of our fundamental understanding of nuclear physics. In this section, we will focus on the initial-state physics program via the ultra-peripheral collision in nucleus-nucleus (AA) interactions.

In relativistic heavy-ion collisions, a large fraction of the total cross section or interaction between the two colliding nucleus is provided by photon-induced reactions. Most of these events are removed by the requirement of inelastic collisions, because the hot quark-gluon-plasma (QGP) can be more likely, if not only, to be produced in such high parton density system. However, these events are difficult to understand if one wants to separate effects related to the initial state, e.g., nuclear parton distribution functions (nPDFs), from final-state interactions, such as fragmentation, medium-induced collective effects, etc. One way to overcome this difficulty is to "turn off" the QGP and use a simple and clean probe to examine the nuclear target - photon-nucleus collisions, which is also known as the "ultra-peripheral collisions" (UPC).

Typically, the UPC takes places when the impact parameter between the two colliding nucleus is greater than the sum of their radii. The interaction is initiated by one or multiple photons emitted from the moving charged ions, where the photon interacts with the other nucleus. Due to the large mass of the heavy nucleus, the emitted photons have very small virtualities or very small p_T. This process is regarded as *photoproduction*. For example, diffractive Vector Meson (VM) photoproduction has been extensively studied at the RHIC and at the LHC, where the gluon density distribution of the nucleon and nucleus target can be directly probed. In recent analyses carried out by the LHC collaborations [73–80], photoproduction of the J/ψ meson has been measured in UPCs of heavy ions. The resulting cross sections were found to be significantly suppressed with respect to that of a free proton. [73,74,78,79] Leading Twist Approximation (LTA) calculations strongly suggest that the suppression is caused by the gluon shadowing effect [81–83], while other models, e.g., the Color Dipole Model with gluon saturation and nucleon shape fluctuations [84], can also describe the UPC data qualitatively. The mechanism of gluon density modification in the nuclear environment remains unknown.

However, there are other processes of photoproduction that are sensitive to the nPDFs. For example, inclusive and diffractive back-to-back jets (dijets) in nuclei are sensitive to both quark and gluon distribution, and it is theoretically easier to be used in the global PDF analysis. Recent studies from Refs. [85–87] have shown the uncertainty of nPDFs can be reduced by a factor of 2 by having these experimental measurements. In addition, the incoming low-virtuality photons can have properties of a point-like particle (direct process) or a hadron with partonic substructure (resolved process). The dijets photoproduction process can be extremely useful in constraining the photon structure, which still remains poorly known

to-date. Finally, the diffractive dijets contribution is a sensitive experimental observable to understand the QCD factorisation breaking and the diffractive nPDFs.

Last but not least, inclusive particle photoproduction at high energy provides important insights to the *soft physics* of photon-nucleus interactions, where cold nuclear matter and Intra-Nuclear Cascade can be studied via fragmentation in both current and target fragmentation regions. One recent study led by Chang et al [88] has shown the difficulty of describing the charged particle production in nuclei of existing E665 experimental data. Although the experimental data of E665 is with higher photon virtualities, particle photoproduction in UPC at high energy can be complementary to the understanding of nuclear fragmentation in general. Furthermore, inclusive high-p_T charged particle or J/ψ photoproduction can be a baseline for comparison to the diffractive VM production, where different theoretical models have drastically different prediction, e.g., gluon saturation model [84] verse nuclear shadowing model. [81–83] The UPC data can provide important insights to the studies of non-linear gluon effects before the EIC. At the EIC, together with different VM productions and with different level arm of photon virtualities, this measurement will be extended much further and hopefully definitive.

Hereby, we propose to utilize the unique capability of the RHIC experimental program in the upcoming 2023-2025 runs with the STAR detector and its recent forward upgrades, to study photoproduction processes in details. The major advantage is that the top RHIC energy can access a kinematic regime that is hardly, if not at all, accessible by the LHC experiments, and provide a seamless transition to the physics at the EIC.

Photoproduction of Vector-Meson

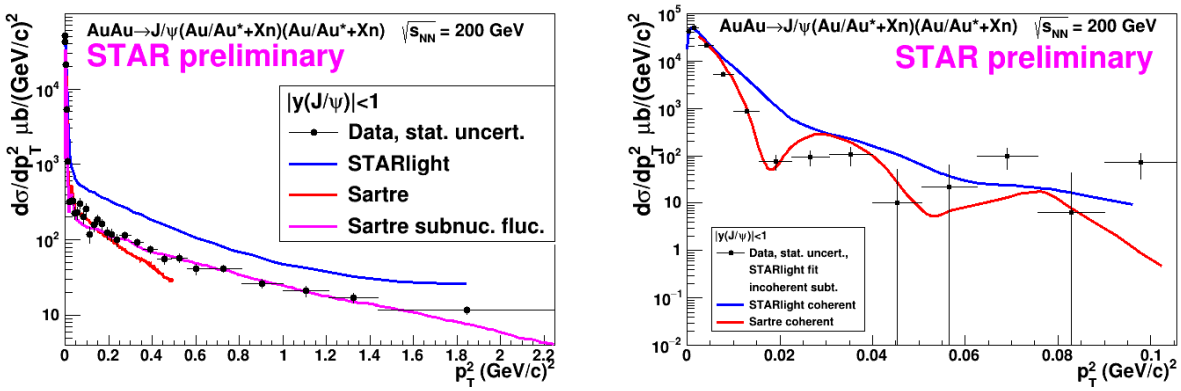

Figure 24: Left: differential cross section $d\sigma/dp_T^2$ of J/ψ photoproduction as a function of p_T^2 in Au+Au UPC at 200 GeV. Right: the same cross section but with incoherent contribution subtracted.

One of the most important and direct measurements of the gluon density in the initial-state of nuclei is the photoproduction of Vector-Meson, e.g., ρ^0, ϕ, and J/ψ. The process can be generally considered in a color dipole picture, where the quasi-real photon emitted

from the heavy nucleus fluctuates into a quark and anti-quark pair (leading order). The quark and anti-quark pair scatters off the nucleus with a Pomeron exchange and becomes a Vector-Meson; the cross section of this process is directly sensitive to the gluon density and its spatial distribution.

In previous STAR publications, there has been studies on ρ^0 meson, e.g., the most recent analysis in Ref. [75] for coherent photoproduction. Although the measurement has provided important insights to the structure of the gold nucleus, e.g., the impact parameter distribution from a Fourier transform of the momentum transfer $-t$ distribution, the general theoretical concern is that the process lacks of a hard scale because the mass of ρ^0 is rather small. Therefore, perturbative calculations of QCD are difficult to be carried out. In addition, the scale dependence of the photoproduction process is also of great interest, which can be only achieved by varying the mass of the Vector-Meson in photoproduction. Therefore, heavier vector-mesons, e.g., J/ψ, are important to be measured.

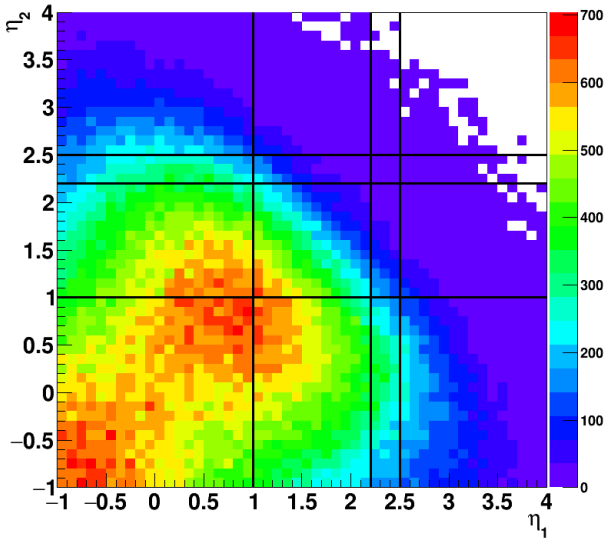

Figure 25: Pseudorapidity distribution of daughter electrons from the J/ψ decay using STARLight MC simulations. Lines are boundary acceptance of Barrel, Endcap, and Forward upgrade detectors.

In Fig. 24, the STAR preliminary results on J/ψ photoproduction are shown in Au+Au UPC at 200 GeV. The differential cross section of $d\sigma/dp_T^2$ as a function of p_T^2 is presented, with the total contribution (left) and coherent contribution only (right). The data has been compared with leading Monte Carlo models STARlight and Sartre, where a much better description by Sartre is found. This is the first differential measurement of J/ψ photoproduction off gold nucleus at the center-of-mass energy between photon and nucleon (proton or neutron), $W \sim 25$ GeV, which provides important constraints to the gluon density and its spatial distribution at this kinematic region, $x_g \sim 0.01$. The observed suppression of the gluon density from this data, compared to the Impulse Approximation, is found to be 15-20%.

Since the data presented above was taken in 2016, the acceptance of J/ψ is limited to rapidity $y < 1$ due to the η acceptance of the daughter electrons. However, this can be significantly improved in Run-23+2025 Au+Au at 200 GeV with the endcap EMC, inner TPC, and forward upgrade detectors. The extension of acceptance in rapidity to $1 < y < 1.5$ can lead to a lower x down to 4×10^{-3}, which overlaps with the LHC kinematics, as well as going to higher x up to 0.05. With the forward upgrades, $y > 2.5$, the kinematic coverage will be even wider, where STAR can cover a regime that is complementary to the LHC, e.g., the anti-shadowing region $x_g \sim 0.1$.

In Fig. 25, it shows the pseudorapidity distribution of both daughter electrons from the J/ψ decay, simulated by the STARLight MC model. The lines are boundaries of the barrel, endcap, and forward detector acceptances. By extending to the endcap and forward, there is a significant improvement in the J/ψ acceptance. Based on the established UPC J/ψ trigger using both barrel and endcap, a high statistics event sample can be collected.

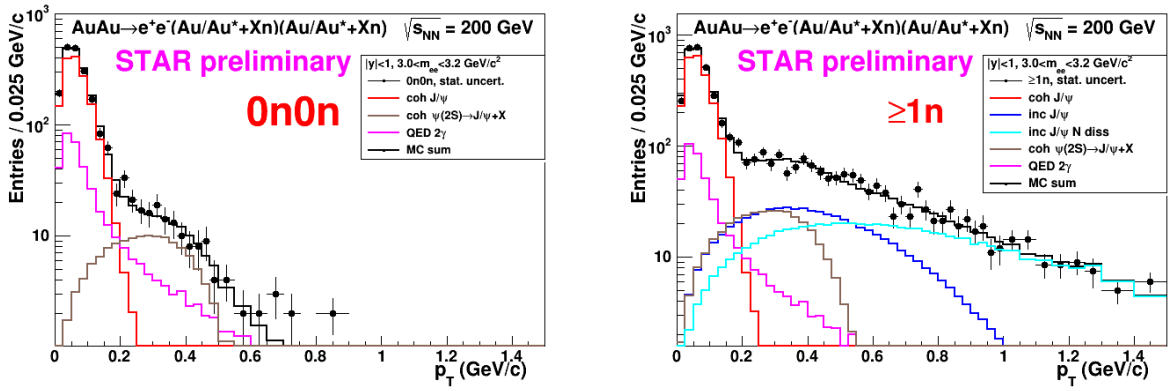

Figure 26: Uncorrected p_T of J/ψ mesons fitted with different contributions in Au+Au UPC at 200 GeV with no neutron on either side (left) and at least 1 neutron on either side (right).

When extending the acceptance of J/ψ to higher rapidity, there is a long standing issue of photon energy ambiguity. At a J/ψ rapidity that $y \neq 0$, the photon energy can be $(M_J/2)e^{\pm y}$, which corresponds to a higher and lower photon energy, respectively. However, thanks to the neutron tagging in the ZDCs, this ambiguity can be resolved by considering different neutron multiplicities and their theoretical expected photon fluxes. [89] The STAR analysis using this method has just begun. In order to qualitatively see the difference by introducing different neutron tagging classes, see Fig. 26. For details of this method, see Ref. [89].

Finally, for the STAR upcoming Run-23+25, there is an opportunity for measuring the photoproduction of ϕ meson for the first time. The experimental challenge of this measurement is that ϕ is usually reconstructed via the kaon channel. However, for photoproduction process, the momentum of the kaon daughters are very soft, ~ 100 MeV/c, such that reconstructing the daughter tracks has been impossible with only the TPC. However, for the upcoming runs, the inner TPC could push the low momentum tracking down to ~ 100 MeV/c. There are two ways to achieve a statistical significant event sample of UPC ϕ meson.

The first one is to use ZDC coincidence trigger with no TOF requirement at the full magnetic field in STAR, while the second one is to use the standard TOF-base UPC Vector-Meson trigger at half-field. At full field, although the inner TPC can reconstruct tracks down to ~ 100 MeV/c, it would not reach TOF for triggers due to the small bending radius. Therefore, events can be collected without a dedicated UPC ϕ trigger. This requires a large integrated luminosity to reach a few thousand raw ϕ events, based on the recent study using 2019 Au+Au data. However, if STAR can be run at half field, the TOF-base trigger might be applicable. See Fig. 27 for illustration of the TOF-based trigger acceptance in kaon p_T. Half-field running is not currently being proposed, but detailed simulations are in progress to fully evaluate.

With all three Vector-Meson (ρ^0, ϕ, and J/ψ) measured at STAR in Au+Au UPC, they will provide an unprecedented understanding of the diffractive process off the gold nucleus in photoproduction, providing valuable experimental inputs to such physics at the EIC.

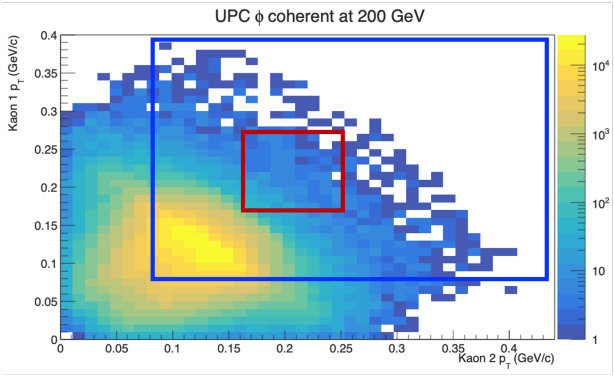

Figure 27: UPC ϕ meson decay p_{T} distributions of daughter 1 vs 2. The red box is the acceptance in p_{T} if requiring track to reach the location of TOF at STAR's full magnetic field; blue box is showing the same but with STAR at the half-field running.

Vetor-Meson decay: probing gluon distribution inside the nucleus

STAR recently observed a significant $\cos 2\Delta\phi$ azimuthal modulation in $\pi^+\pi^-$ pairs from photonuclear ρ^0 and continuum production. The structure of the observed modulation as a function of the $\pi^+\pi^-$ pair $P_\perp$, appears related to the diffractive pattern. Recent theoretical calculations [90], which implemented linearly polarized photons interacting with the saturated gluons inside a nucleus, have successfully described the qualitative features of the observed modulation (see Fig. 28), and indicate that the detailed structure of the $\cos 2\Delta\phi$ modulation vs. $P_\perp$ is sensitive to the nuclear geometry and gluon distribution. Data from Run-23 and Run-25 would allow the additional statistical reach needed to perform multi-differential analysis, providing stronger theoretical constraints. Specifically, multi-differential analysis of the $\cos 2\Delta\phi$ modulation with respect to pair rapidity and pair mass are needed. Multi-differential analysis with respect to pair mass is needed to separate the ρ^0 production from the continuum Drell-Soding production. Multi-differential analysis with respect

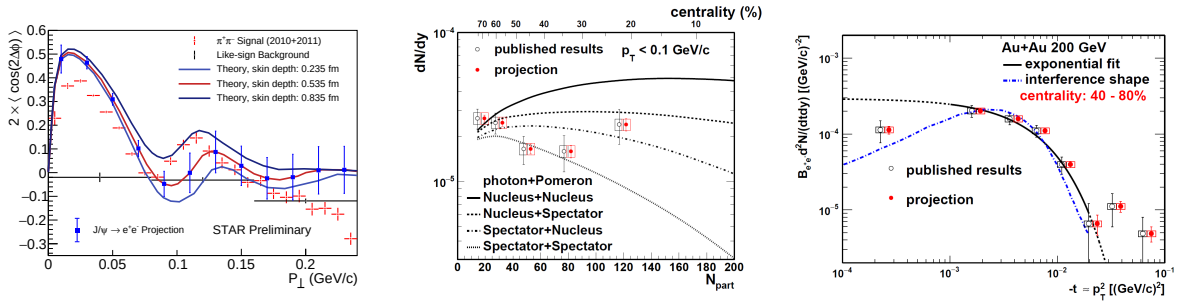

Figure 28: Left: Measurement of the $\cos 2\Delta\phi$ modulation of $\pi^+\pi^-$ pairs from photonuclear ρ^0 and continuum production compared to theoretical predictions [90]. Projections are shown for a similar measurement of the azimuthal modulation of e^+e^- pairs from photonuclear production of the J/ψ. Center: Projection of the dN/dy of photoproduced J/ψ in non-UPC events vs. the event centrality (N_{part}) compared to various theoretical production scenarios. Right: Projection of the t spectra of photoproduced J/ψ in $40-80\%$ central collisions.

to the pair rapidity is needed to quantitatively investigate how the double-slit interference mechanism effects the structure of the observed azimuthal modulation. Additional statistical precision is also needed for measurement of the higher harmonics. Similar measurements with $J/\Psi \to e^+e^-$ can be performed and such measurements at higher mass provide better comparison with more reliable QCD calculation.

Ultraperipheral AA collisions, where photons generated by the Lorentz-boosted electromagnetic field of one nucleus interact with the gluons inside the other nucleus, can provide certain 3D gluonic tomography measurements of heavy ions, even before the operation of the future EIC. STAR has performed experimental measurements of the photoproduction of J/ψ at low p_T in non-UPC heavy-ion collisions [91], accompanying the violent hadronic collisions. A detailed study with p_T distributions has shown that the $|t|$ distribution in peripheral collisions is more consistent with the coherent diffractive process than the incoherent process. Although models [92,93] incorporating different partial coherent photon and nuclear interactions could explain the yields, it remains unclear how the coherent process happens and whether final-state effects play any role. [94] Resolving this puzzle with high statistical data and detailed $|t|$ distributions at different centralities at RHIC as projected for Run-23+25 in Fig. 28 may be important for understanding what defines the coherentness of the photoproduction, how vector mesons are formed in the process and how exclusive the similar process has to be in future EIC experiments with forward neutron veto/tagging.

Photoproduction of dijets

In addition to photoproduction of Vector-Meson, photoproduction of back-to-back jets has been increasingly interested in the context of nuclear PDF. The process is a two-to-two hard scattering between a direct or resolved photon from the projectile (photon from UPC) and the quarks or gluons from the nucleus target. The final-state is a pair of back-to-back jet, which is directly sensitive to the photon and nuclear structure in terms of parton distribution

functions. At the LHC, this process corresponds to the kinematic region $x_A \sim 10^{-3}$, which is the gluon dominated regime. Here we propose to measure the photoproduction dijets at STAR, where kinematic regions, e.g., the anti-shadowing and the EMC region, can be reached. This measurement has never been done at RHIC and will provide a significant constraints to the nPDFs of heavy nucleus at this kinematics for photoproduction.

The pseudo-data from eA collisions used here is generated by BeAGLE (**B**enchmark **eA** **G**enerator for **LE**ptoproduction) [88], based on the lepton and gold beam energy of 18× 100 GeV, where the input PDF for the the exchanged photon is the CTEQ 5 from the LHAPDF library [95] and EPS09 for the nuclear PDF.

Jets are reconstructed by FastJet [96] with the anti-k_T algorithm, which is based on the energy distribution of final state particles in the angular space. All the stable and visible particles produced in the collisions with $p_T > 250$ MeV/c and $-1.5 < \eta < 1.5$ and $2.5 < \eta < 4.0$ in the laboratory system are taken as input. The jet cone radius parameter has been set to $R_{\rm jet} = 1$ in the jet finding algorithm. To obtain the events in Au+Au UPC collisions at $\sqrt{s_{\rm NN}} = 200$ GeV from simulations of eAu at 18×100 GeV, an event-by-event weight is applied according to the photon flux difference between eA and Au+Au UPC collisions.

After reweighing we obtain the dijet events with the pesudorapidity of jets ($\eta^{\rm jet}$) from -1.5 to 1.5 in middle rapidity region and $2.5 < \eta^{\rm jet} < 4.0$ in the forward region. In each event, the jet with the highest p_T is called the trigger jet, the jet with the second highest p_T is called the associate jet. Events are selected with the requirement that the trigger jet has $p_T^{\rm trig} > 5$ GeV/c and the associated one has $p_T^{\rm asso} > 4.5$ GeV/c. 100 M event are generated, after all cuts applied, we found ~ 5600 dijet events corresponding to the integrated luminosity $L = 9$ nb^{-1}. Therefore, with STAR Run-23+25 Au+Au collisions, an event sample of dijets of 50-60k is expected.

In 200 GeV Au+Au UPC collisions, the distributions of jets' pesudorapidity and p_T can be found in Fig. 29. Jets dominate at $\eta \sim 0.5$ with the maximum $p_T \sim 20$ GeV/c.

In BeAGLE, depending on the wave function components for the incoming virtual photon, the major hard processes are divided into three classes: the direct processes, the soft VMD processes and the resolved processes (hard VMD and anomalous). The direct photon interacts as a point-like particle with the partons of the nucleon, major subprocesses in direct category: LO DIS, Photon-Gluon Fusion (PGF) and QCD Compton (QCDC). While the VMD and anomalous components interact through their hadronic structure. Resolved photon processes play a significant part in the production of hard high-p_T processes at $Q^2 \approx 0$. The following hard subprocesses are grouped in the resolved processes category: $qq \to qq$, $q\bar{q} \to q\bar{q}$, $q\bar{q} \to gg$, $qg \to qg$, $gg \to q\bar{q}, gg \to gg$. The examples of Feynman diagrams of resolved and direct processes are shown in Fig. 30.

The momentum fraction of the parton from the exchanged photon (x_γ) and the momentum fraction of the parton from the gold beam ($x_{\rm Au}$) can be reconstructed knowing the momentum and angles of dijets as

$$x_\gamma = \frac{1}{2E_\gamma}(p_T^{\rm tirg} e^{-\eta_{\rm trig}} + p_T^{\rm asso} e^{-\eta_{\rm asso}}) \quad (1)$$

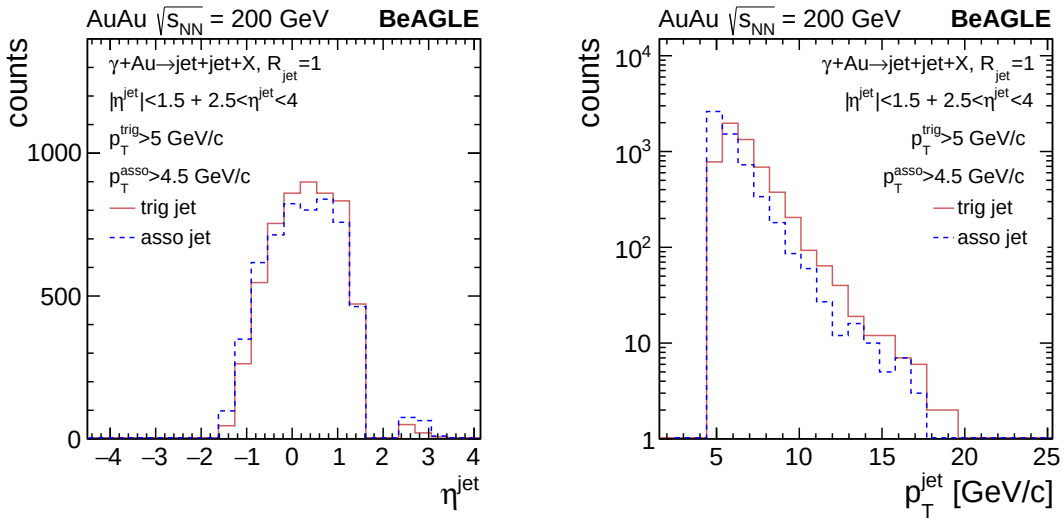

Figure 29: In Au+Au UPC collisions at $\sqrt{s_{\rm NN}}$ = 200 GeV, the dijet events are selected with $|\eta^{\rm jet}| < 1.5 + 2.5 < \eta^{\rm jet} < 4.0$. For the trigger jet: $p_T^{\rm trig} > 5$ GeV/c, associate jet: $p_T^{\rm asso} > 4.5$ GeV/c. Left: the pesudorapidity distributions of the trigger and associated jets; right: the p_T distributions of the trigger and associated jets.

$$x_{\rm Au} = \frac{1}{2E_{\rm Au}}(p_T^{\rm tirg} e^{\eta_{\rm trig}} + p_T^{\rm asso} e^{\eta_{\rm asso}}) \tag{2}$$

where E_γ is the photon energy which can be determined from the hadronic final-state, see later for details. Eq. 1 and Eq. 2 are valid in the lab frame in LO.

The reconstructed x_γ and $x_{\rm Au}$ in AuAu UPC dijet events can be seen from Fig. 31. The reconstructed x_γ covers a wide range from 0.2 to 0.9 in resolved process, and dominates at high x in direct process. The reconstructed $x_{\rm Au}$ distributions contain two peaks as there are two pseudorapidity regions. The forward pseudorapidity ($2.5 < \eta^{\rm jet} < 4.0$) leads to the peak at high $x_{\rm Au} \sim 0.5$, while middle rapidity jets ($|\eta^{\rm jet}| < 1.5$) contribute the peak at $x_{\rm Au} <\sim 0.2$. With the Run-23 and 25 data of Au+Au and Run-24 p$^\uparrow$+Au at STAR, this will become the first measurement at this kinematic region at RHIC with good statistical precision.

Taking one step further, the exclusive or diffractive dijets can also be measured in $p^\uparrow p^\uparrow$, p$^\uparrow$+Au, and Au+Au at $\sqrt{s_{\rm NN}} = 200$ GeV. The process is diffractive such that there are only two jets in the event, where the target nucleon or nucleus stay intact. Similar to exclusive Vector-Meson production discussed earlier, the exclusive dijets can provide a large impact in understanding the nucleon and nuclear structure over a wide range of kinematics. In addition, with the unique target polarization at RHIC, the exclusive dijets could be sensitive to Generalized Parton Distributions and p_T Dependent PDFs. This process is expected to be complementary to the process discussed in Sec. 2.1. In Fig. 32, the diffractive dijets photoproduction in p+Au UPCs are shown, with the transverse energy ($E_{\rm T}$) on the left panel and the dijet η separation distribution on the right panel. For a first look, the STAR Upcoming run 2024 would have enough luminosity to achieve reasonable statistics of this

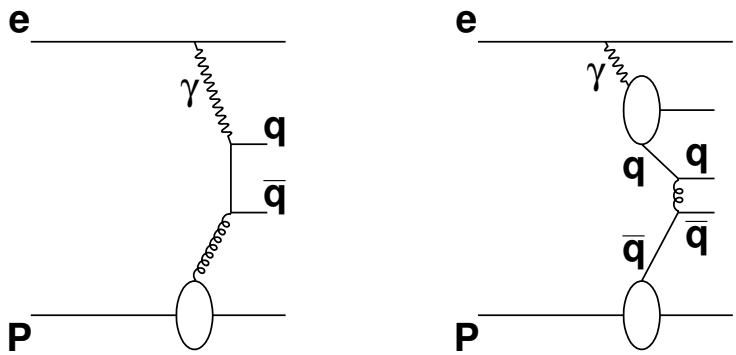

Figure 30: Examples of diagrams for direct (left) and resolved (right) processes in electron-proton scattering. In UPC, the photon emitter is replaced with the Au nucleus.

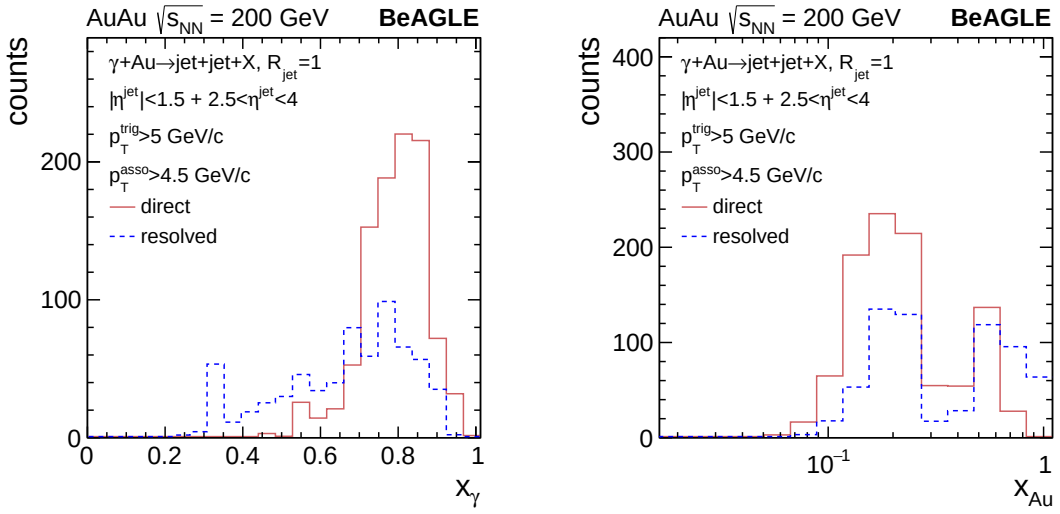

Figure 31: In AuAu UPC collisions at $\sqrt{s_{\rm NN}} = 200$ GeV, the dijet events are selected with $|\eta^{\rm jet}| < 1.5 + 2.5 < \eta^{\rm jet} < 4.0$. For the trigger jet: $p_T^{\rm trig} > 5$ GeV/c, associate jet: $p_T^{\rm asso} > 4.5$ GeV/c. Left: the x_γ distributions in resolved and direct processes; right: he $x_{\rm Au}$ distributions in resolved and direct processes.

measurement; the same measurement can be done in p+p and Au+Au collisions.

Additional opportunities are available for STAR Run-23+25 based on UPC jets, e.g., measurement of diffractive dijets off polarized proton target, and azimuthal correlation of the dijets, which will be sensitive to nPDFs, diffractive nPDFs, QCD factorisation breaking, and spin structure of the proton. Here we do not elaborate them in details but defer the readers to Refs. [86, 87, 97–100] for both UPCs and at the EIC.

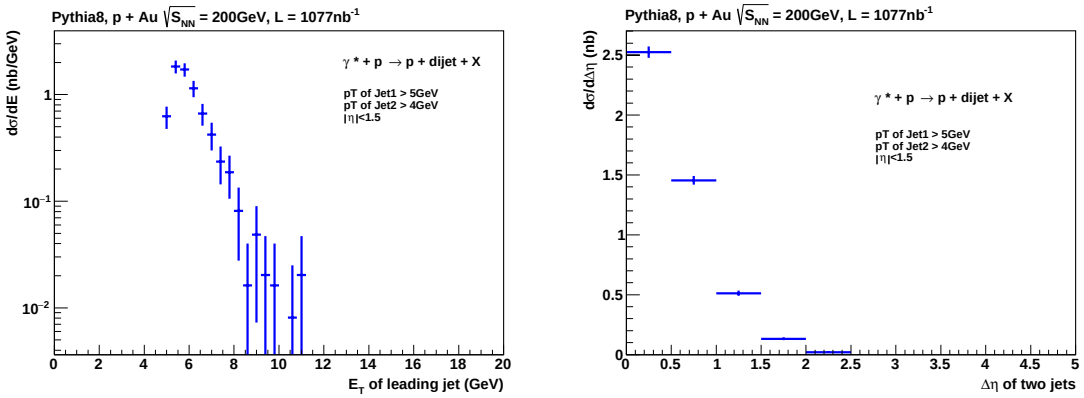

Figure 32: In p+Au UPC collisions at $\sqrt{s_{\rm NN}}$ = 200 GeV, the diffractive dijet events are selected with the trigger jet: $p_T^{\rm trig} > 5$ GeV/c and associate jet: $p_T^{\rm asso} > 4.0$ GeV/c. The $E_{\rm T}$ distributions of the leading jet (left) and $\Delta\eta$ of the dijets distributions (right) are shown with ~ 1 μb^{-1} integrated luminosity.

Photoproduction of inclusive charged particles and cross sections

Inclusive photoproduction processes in high-energy ep collisions have been extensively studied at HERA, e.g., charged particle productions, inclusive cross section, heavy-flavor production, etc. Recently, there have been efforts re-analyzing the HERA data in photoproduction and deep inelastic scattering to look for collectivity in terms of azimuthal correlations [101], inspired by the outstanding flow phenomena in heavy-ion collisions. At the LHC, experiments have just begun using the UPCs to look at collisions between photons and heavy nuclei in photoproduction, primarily to search for the collective phenomena. However, inclusive photoproduction processes in nuclei at high energy remains largely unexplored.

Inclusive photoproduction process is generally challenging for the UPC in heavy-ion experiments. At HERA, photoproduction in ep scattering can be unambiguously identified by the small angle electron taggers, where event kinematics can be reconstructed. However, in heavy-ion UPCs, the photon emitting nucleus is invisible to the experiment, leaving the kinematics, e.g., W, largely unconstrained. In a recent study using general-purpose eA MC model BeAGLE, it is found that the event kinematic reconstruction in UPC can be approached based on the hadronic final-state (HFS).

In Fig. 33 left, it shows the photon energy distribution based on MC simulation of BeAGLE of eAu 18 $\times$ 100 GeV. In addition, by using the photon flux generated by the UPC at 200 GeV Au+Au collisions, the photon energy spectra is reweighted and shown as the open circle. The low photon energy is greatly enhanced due to the large flux generated by the heavy nucleus, while the spectra is much steeper than in the eAu collisions. In Fig. 33 right, the HFS method has been adopted to reconstruct the kinematic variable W, based on the STAR acceptance including the forward upgrade detectors. The smearing from truth to reconstructed W is visible and stronger at large W. However, by selecting on the re-

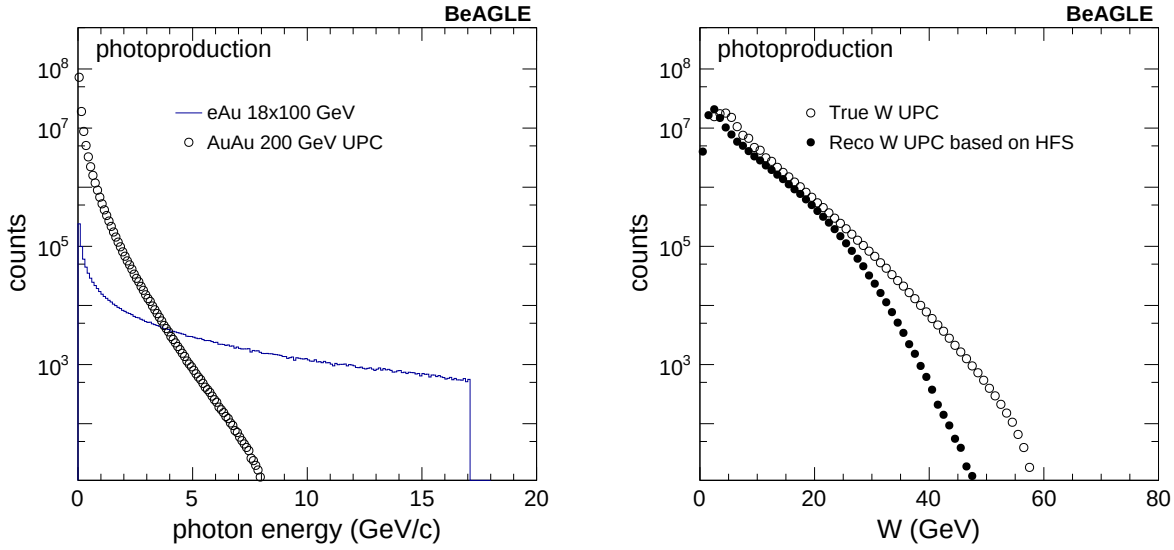

Figure 33: Left: photon energy distribution in eA and Au+Au UPC. Right: The truth level W in Au+Au UPC and the corresponding reconstructed level based on the HFS method.

constructed W, the event kinematics can be better controlled than using the average only. Unfolding technique can be used here for correcting the bin migration in W as well. Note that there is no detector simulations shown here.

In the upcoming RHIC Run-23 and Run-25, the inclusive photoproduction is of great interest. The cross section of such events is generally large, while a different trigger is required comparing to the standard minimum-bias hadronic collision trigger. The baseline trigger has been developed during the Au+Au 200 GeV data taken in 2019, where only a ZDC coincidence was required. For Run-23 and 25, asymmetry BBC response could be added to more efficiently select the inclusive photoproduction process.

Search for collectivity and signatures of baryon junction in photo-nuclear (γ+Au) processes

Until the EIC is built, high-energy photoproduction processes (low virtuality limit of the deep inelastic scattering) can be studied using ultra-peripheral ion collisions (UPCs) that occur when two heavy ions interact at large impact parameters. Such collisions can be considered as γ+Au processes but unlike at the EIC, the photons involved in UPCs are quasi-real. For UPCs at top RHIC energies one expects the energy of the quasi-real photon to be approximately $E_\gamma \approx 3$ GeV. The typical range of the center of mass energy of the photon-nucleon system will therefore be $W_{\gamma N} \approx 40$ GeV. Therefore, Au+Au collisions at $\sqrt{s_{NN}} = 200$ GeV will provide access to the γ+Au process at 40 GeV center of mass energy. Our specific interest is high activity inclusive γ+Au process to search for collectively and improve our understanding of the mechanism of baryon stopping.

A satisfactory microscopic explanation of how collectivity originates from the basic processes of QCD and evolves with collision system size is a topic of broad interest in the community of high energy nuclear physics. The formation of a quark-gluon plasma medium and its fluid-dynamic expansion explain the origin of collectivity in Au+Au collisions. Results from RHIC small system scan indicate fluid-dynamic expansion are essential to drive collectivity in ^{3}He/d/p+Au collisions. [102] A search for collectivity in γ+Au interactions at RHIC will be a natural continuation of the recent system size scan [102], extending it at the small end to complete the hierarchy: Au+Au > ^{3}He+Au > d+Au > p+Au > γ+Au. This will help better address how collectivity originates and evolves with system size. If collectivity is observed in γ+Au processes it can provide a way to explore the creation of a many-body system exhibiting fluid behavior in photon-induced processes. [103] A recent calculations in Ref [103] assumes γ+A processes are equivalent to collisions of vector meson with ions (ρ+A collisions) and describe first measurements of harmonic coefficients v_n in photonuclear processes measured by the ATLAS collaboration. [104] The hypothesis of γ+A process as ρ+A collisions and the formation of a fluid-dynamic medium can be tested at RHIC in a data-driven way. This can be done by comparing measurements in γ+Au processes at $W_{\gamma N}$ $\approx$40 GeV and in d+Au collisions at $\sqrt{s_{\rm NN}}$39 GeV. The former will be possible if a high statistics data set is collected for Au+Au collisions at $\sqrt{s_{\rm NN}}$200 during the Run-23 and 25 and the latter can be performed with the existing RHIC data on tape. It is known from RHIC measurements, argument based on initial geometry and, fluid dynamic calculations that elliptic anisotropy coefficient follow a hierarchy of v_2(d+Au) > v_2(p+Au) at a fixed collision energy and multiplicity. [102, 105] Following a similar argument one expects v_2(d+Au) > v_2(ρ+Au). In the fluid dynamic picture of Ref [103] the elliptic anisotropy coefficient will show the following hierarchy: v_2(d+Au) > v_2(γ+Au). A similar test by comparing v_2(p+Pb) and v_2(γ+Pb) at the LHC is difficult since the center of mass energy differs by a factor of six between p+Pb and γ+Pb collisions.

Photonuclear processes can also be used to study the origin of baryon stopping and baryon structure in general. One proposed mechanism for explaining the baryon stopping is the baryon junction: a nonperturbative Y-shaped configuration gluons which is attached to all three valence quarks. In this picture it is the baryon junction that carries the baryon number rather than the valence quarks. The existence of baryon junctions and their interaction with the incoming target or projectile are theorized to be an effective mechanism for substantial baryon stopping in pp and AA [106], but this has yet to be confirmed experimentally. Photonuclear processes allow us to study baryon stopping in the simplest possible process. The vast majority of these collisions occur through what is called the resolved process where the quasi-real photon fluctuates into a quark-antiquark pair which then collides with the other ion. [107] If the baryon number were carried by the three valence quarks, then this quark-antiquark pair would not be able to stop the baryons, but it is possible for the quark-antiquark pair to interact with the junction and produce a midrapidity baryon. An added benefit is that photonuclear processes are highly asymmetric and baryons only enter from one side of the collision. The baryon-junction stopping mechanism is predicted to cause an exponential damping of the cross section with rapidity $\sim \exp\left(-\alpha_0^J(y - Y_{\rm beam})\right)$,

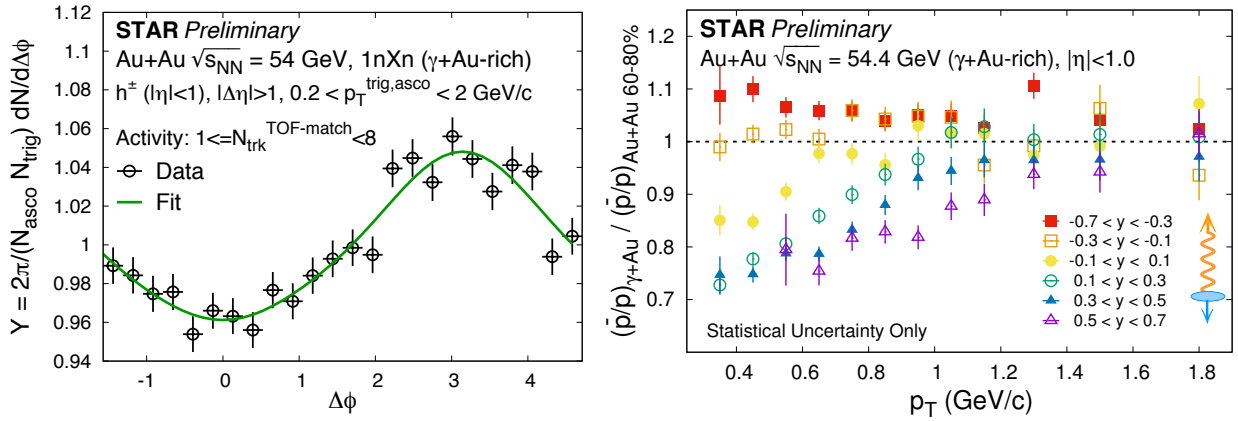

Figure 34: (Left) STAR preliminary data on normalized yield of long range di-hadron correlations in γ+Au-rich events with a relative pseudroapidity gap of $|\Delta\eta| > 1$ between two hadrons. The events are selected by applying asymmetric cuts on the energy deposition of neutrons in ZDCs (1nXn) and on TPC tracks matched with TOF $N_{\rm trk}^{\rm TOF-match}$ in the window of $1 <= N_{\rm trk}^{\rm TOF-match} < 8$. The green curve represents a fit to data using a function: $1 + 2\sum a_n \cos(n\Delta\phi)$. No signatures of collectivity associated with enhancement of correlation near relative azimuthal angle $\Delta\phi \sim 0$ is observed. (Right) The double ratio of antiprotons to protons in γ+Au-rich events compared to peripheral Au+Au events, indicating significant enhancement of protons at low p_T and at mid-rapidity. The enhancement shows a strong rapidity dependence while going from the photon to ion direction.

where $\alpha_0^J \simeq 1/2$ is the Regge intercept of the baryon junction. [106] In a symmetric hadronic collision, baryons are traveling from either direction so the stopping of both the target ($\sim \exp\left(-\alpha_0^J(y - Y_{\rm beam})\right)$) and the projectile ($\sim \exp\left(\alpha_0^J(y - Y_{\rm beam})\right)$) will likely compensate for each other, leading to a nearly symmetric distribution. But in an asymmetric system like a photonuclear collision, this exponential shape should be visible.

A handful of data sets exist on the disk with the appropriate event trigger selection for studying photonuclear processes at RHIC. In Fig. 34 we present preliminary results on γ+Au-rich interactions using Au+Au 54 GeV data from STAR shown at the Quark Matter 2022 conference. By identifying the single neutron peak for individual ZDCs, we require the cuts equivalent to 1nXn. We apply an asymmetric cut on east and west BBCs to improve the purity. We also make sure the position of the primary vertex along collision direction V_z from TPC and VPD detectors differs by about 10 cm. After applying such cuts on Au+Au 54 GeV data we perform measurements in γ+Au-rich events.

Figure 34 (left) shows the normalized yield, differential in relative azimuthal angle of the trigger and associated particles $Y(\Delta\phi) = 2\pi/N_{\rm trig}/N_{\rm asco} dN^{\rm pair}/d\Delta\phi$ integrated over a relative pseudorapidity window of $|\Delta\eta| > 1$. For this analysis, the p_T of trigger and associated particles is chosen to be within $0.2 < p_T^{\rm trig,asco} < 2$ GeV/c. The distribution $Y(\Delta\phi)$ is shown for two different bins of activity characterized by the number of TPC tracks matched with the TOF $1 <= N_{\rm trk}^{\rm TOF} < 8$ (low activity). The distribution is fitted using a Fourier function of the form $(1 + 2\sum a_n \cos(n\Delta\phi))$ (green curve). No ridge-like component associated with a significant enhancement of $Y(\Delta\phi)$ near $\Delta\phi = 0$ that is related to the signature of collectivity

is seen.

Figure 34 (right) shows the measurement of the yield of anti-protons-to-protons ($\bar{p}/p$) with $p_{\rm T}$. The quantity plotted is a double ratio of $\bar{p}/p$ for the measurements in γ+Au-rich events over the same in 60–80% peripheral Au+Au events. We see a suppression of the $\bar{p}/p$ yield in γ+Au events at low $p_T < 0.6$ GeV/c and for the symmetric window of $-0.1 < y < 0.1$ around mid-rapidity. The suppression of $\bar{p}/p$ yield gets stronger while going from the photon to the ion direction, with the double ratio dropping by a factor 0.75 at low p_T. We have checked that this trend is not seen for π^-/π^+, K^-/K^+ and not explained by PYTHIA 6 model. This important observation provides the necessary impetus for further exploration using various available data sets. In particular, we would like to test if this strong rapidity dependence of the $\bar{p}/p$ yield is consistent with the picture of baryon junction that predicts an exponential dependence of stopping with rapidity of form $\exp(-\alpha(y - Y_{\rm beam}))$ with α =0.5.

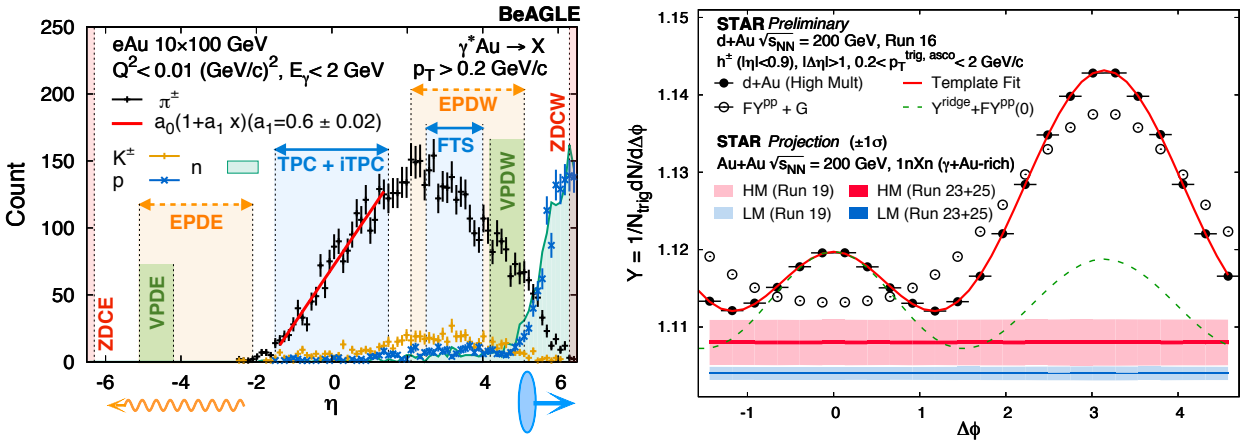

Figure 35: (Left) Pseudorapidity distribution of different particles using the state-of-the-art BeAGLE [88,108] event generator for the EIC in e+Au events. By restricting the virtuality and energy of the photon (γ^*) we try to mimic the kinematics of a $\gamma + Au$ (Au+Au UPC) event. The purpose of this plot is to demonstrate how different STAR detectors will be used to identify such UPC processes. (Right) STAR preliminary data on per-trigger yield estimated using di-hadron correlations in d+Au (hadronic) 200 GeV collisions. The correlation function in p+p collisions (open circle) is used as a template to fit the same in relatively high multiplicity d+Au collisions (solid circle) and to extract the long-range ridge-like component. The red and blue band show projections for $\gamma + Au$ enriched events for two different multiplicity bins. The aim is to use the correlation function from the low multiplicity $\gamma + Au$ to perform template fit in the high multiplicity bin.

Our aim will be extend these measurements with high statistics γ+Au-rich event samples using Run-23 and 25 data on Au+Au collisions at $\sqrt{s_{\rm NN}}$ = 200 GeV. Fig. 35(left) shows the pseudorapidity (η) distribution of identified particles with $p_T > 0.2$ GeV/c in inclusive e+Au photoproduction (γ^*+Au, where γ^* refers to a virtual photon) processes simulated using the EIC Monte Carlo BeAGLE event generator [88, 108] with electron and ion beam energy of 10 and 100 GeV, respectively. The virtuality of the exchanged photon is restricted to be $Q^2 < 0.01$ GeV/c^2 and photon energy is restricted to be $E_\gamma < 2$ GeV to mimic

γ+Au interactions in Au+Au UPCs at $\sqrt{s_{NN}}$=200 GeV. This figure demonstrates how the combination of the inner Time Projection Chamber (iTPC), the new highly granular Event-Plane Detectors (EPD) and forward tracking system (FTS) and the Zero-Degree Calorimeters (ZDC) can be used to isolate γ+Au events from peripheral Au+Au events (symmetric in η with no gaps). In terms of triggering the γ+Au interactions, the most stringent selection criterion is that the ZDCE detector should be restricted to have a single neutron hit (1n), while no restriction (Xn) should be placed on the ZDCW to trigger on γ+Au candidates with east-going photons, and vice versa. We perform a feasibility study using Run=19 data on min-bias Au+Au collisions using about 130 M events. Figure 35 shows STAR preliminary data on the per-trigger yield in di-hadron correlations in d+Au events where a clear ridge can be seen after template fitting. On the same plot we show projections of uncertainties for the di-hadron correlations in possible γ+Au-rich events using Au+Au 200 GeV data from Run 19 (130 M events) and using Au+Au 200 GeV data from anticipated Run=23+25 (20 B events). Projections are shown for high activity (HM) and low activity (LM) event classes determined by the uncorrected track multiplicity in TPC matched with TOF of $15 <= N_{\rm trk}^{\rm TOF} < 25$ and $1 <= N_{\rm trk}^{\rm TOF} < 8$, respectively. Even without any dedicated trigger, 20 B minbias Au+Au events can already give us enough $\gamma + Au$ candidates to significantly reduce the uncertainties shown by the red and blue projection bands in Fig. 35. This will enable us to perform differential measurements of di-hadron correlations with different combinations of triggers and associated p_T and perform a search for collectivity and in addition to testing the baryon-junction conjecture.

Other inclusive photoproduction measurements

Besides the search for collectivity in photon-nucleus collisions, there are many other inclusive photoproduction processes are of great interest. In the upcoming Run-23 and Run-25, inclusive photoproduction processes only require a large sample of "minimum-bias" photo-nucleus collision events, instead of special triggered events.

For example, one measurement that will have a large impact is the inclusive J/ψ photoproduction. Note that STAR has results on exclusive J/ψ photoproduction, the complementary inclusive measurement (together with exclusive measurements) can be sensitive to the saturation or non-linear gluon dynamics. The observable is as follows,

$$\frac{\sigma_{\rm J/\psi}^{\rm exclusive}/\sigma_{\rm J/\psi}^{\rm inclusive}|_{\rm Au}}{\sigma_{\rm J/\psi}^{\rm exclusive}/\sigma_{\rm J/\psi}^{\rm inclusive}|_{\rm p}}. \tag{3}$$

The J/ψ inclusive and exclusive photoproduction both provide a hard scale that theoretical calculations can be performed. Qualitatively, the nuclear shadowing model (Leading Twist Approximation [81–83]) predicts this double ratio to be below unity, while saturation models predict above unity. [109] This is one of the very few observables that qualitatively separates these two long standing models. In the upcoming STAR runs of Au+Au and p+Au collisions, this measurement will play an important role in understanding the saturation phenomena before the EIC. For the similar EIC measurement, see Fig. 36 for details.

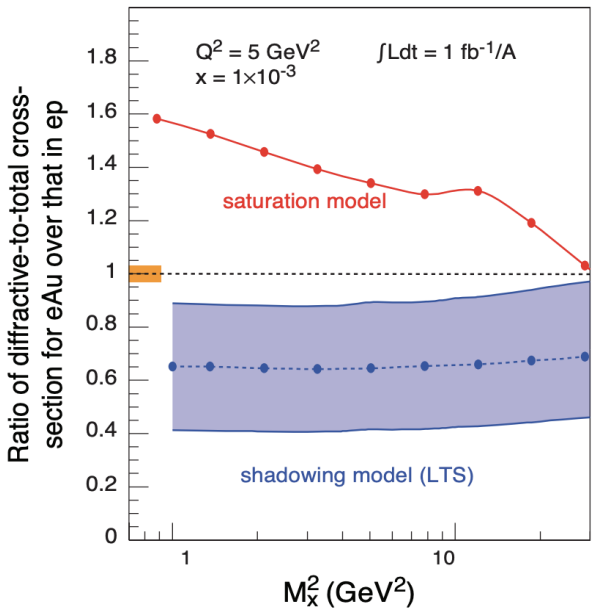

Figure 36: Figure from the EIC White Paper - Fig 1.6 [109]. The ratio of diffractive over total cross-section for DIS on gold normalized to DIS on proton plotted for different values of M_x^2, the mass squared of hadrons produced in the collisions for models assuming saturation and non-saturation. The statistical error bars are too small to depict and the projected systematic uncertainty for the measurements is shown by the orange bar. The theoretical uncertainty for the predictions of the LTS model is shown by the grey band.

The reason we can do this similar measurement in UPCs is because we can replace the DIS measurement (finite Q^2) with photoproduction of J/ψ (both exclusive and inclusive), where the charm quark mass provides the hard scale. Even though the UPC measurement cannot provide a wide range of diffractive mass state (M_x^2), this can provide important insights to the underlying physics mechanism, e.g., gluon saturation and nuclear shadowing effect.

2 Run-25 Request for Polarized p+Au Collisions at 200 GeV

The exploration of the fundamental structure of strongly interacting matter has always thrived on the complementarity of lepton scattering and purely hadronic probes. As the community eagerly anticipates the future Electron Ion Collider (EIC), an outstanding scientific opportunity remains to complete "must-do" measurements in p+Au physics during the final year of RHIC. These measurements will be essential if we are to fully realize the scientific promise of the EIC, by providing a comprehensive set of measurements in hadronic collisions that, when combined with future data from the EIC, will establish the validity and limits of factorization and universality. Much of the physics program outlined here combined with the recently completed Run-24 program is, on the one hand, unique to proton-proton and proton-nucleus collisions and offers discovery potential on its own. On the other hand, these studies will lay the groundwork for the EIC, both scientifically and in terms of refining the experimental requirements of the physics program, and thus are the natural next steps on the path to the EIC. When combined with data from the EIC these STAR results will provide a broad foundation to a deeper understanding of fundamental QCD.

The separation between the intrinsic properties of hadrons and interaction-dependent dynamics, formalized by the concept of factorization, is a cornerstone of QCD and largely responsible for the predictive power of the theory in many contexts. While this concept and the associated notion of universality of the quantities that describe hadron structure have been successfully tested for unpolarized and, to a lesser extent, longitudinally polarized parton densities, its experimental validation remains an unfinished task for much of what the EIC is designed to study – the three-dimensional structure of the proton and the physics of dense partonic systems in heavy nuclei. To establish the validity and limits of factorization and universality, it is essential to have data from *both* lepton-ion and proton-ion collisions, with experimental accuracy that makes quantitative comparisons meaningful.

Run-25, with polarized p+Au collisions at $\sqrt{s_{\rm NN}} = 200$ GeV, will be the last RHIC run. This run can provide STAR with the unique opportunity to investigate this 200 GeV collision system with the Forward Upgrade providing full tracking and calorimetry coverage over the region $2.5 < \eta < 4$ and the iTPC providing enhanced particle identification and expanded pseudorapidity coverage at mid-rapidity. These powerful detection capabilities, when combined with substantially increased sampled luminosity compared to Run-15, will enable critical measurements to probe universality and factorization in transverse spin phenomena and nuclear PDFs and fragmentation functions, as well as low-x non-linear gluon dynamics characteristic of the onset of saturation. This will provide unique insights into fundamental QCD questions in the near term, and essential baseline information for precision universality tests when combined with measurements from the EIC in the future.

We therefore request an extension of 5 weeks for polarized p+Au data-taking at $\sqrt{s_{\rm NN}} =$ 200 GeV at the end of Run-25. The projections in this section also include other scenarios like 10.5 weeks as prepared for Run-24 request. Also, effectively we would request approximately equal nucleon-nucleon luminosities for Run-25 p+Au and Run-24 p+p which is essential to

optimize several critical measurements that require comparisons of the same observable in (polarized or unpolarized) p+p and p+Au collisions described in the following sections.

The p+Au running will involve radially polarized protons. This will maximize the figure-of-merit for the measurements of ultra-peripheral J/ψ production with the Forward Upgrade, and also minimize important systematic uncertainties for the Collins asymmetry measurement using the Forward Upgrade. In Run-24, we collected a sample of 164 pb^{-1} of p+p collisions and for Run-25 we expect 0.22 pb^{-1} of p+Au collisions. These totals represent 3.1 times the luminosity that STAR sampled during transversely polarized p+p collisions in Run-15 and 0.5 times the luminosity that STAR sampled during transversely polarized p+Au collisions in Run-15.

2.1 Spin Physics with Polarized p+Au Collisions at 200 GeV

Together with the previous run, Run-25 will enable STAR to probe the physics questions that can be assessed in the transversely polarized p+p and p+Au collisions with a far more capable detector and much larger datasets than were available during Run-15. With the overlapping kinematic coverage for both p+p and p+Au data, this program is critical to set the stage for related future measurements at the EIC. Here we give brief descriptions of several of the opportunities presented by the completion of this program in Run-25.

2.1.1 Forward Transverse-Spin Asymmetries

The experimental study of spin phenomena in nuclear and particle physics has a long history of producing important, and often surprising, results. Attempts to understand such data have pushed the field forward, forcing the development of both new theoretical frameworks and new experimental techniques. Recent detector upgrades at STAR, at mid- and forward-rapidity, coupled with the versatility of RHIC, will allow us to gain new insights into long-standing puzzles, and to probe more deeply the complexities of emergent behavior in QCD.

Results from PHENIX and STAR have shown that large transverse single-spin asymmetries (TSSA) for inclusive hadron production, first seen in p+p collisions at fixed-target energies and modest p_{T}, extend to the highest RHIC center-of-mass energies, $\sqrt{s} = 510$ GeV, and surprisingly large p_{T}. Figure 37 summarizes the world data for the inclusive neutral pion asymmetries A_N as a function of Feynman-x. The asymmetries are seen to be nearly independent of $\sqrt{s}$ over the very wide range of roughly 19 to 500 GeV.

To understand the observed TSSAs, one needs to go beyond the conventional leading-twist (twist-2) collinear parton picture for the hard-scattering processes. Two theoretical formalisms have been developed to try to explain these sizable asymmetries in the QCD framework: transverse-momentum-dependent (TMD) parton distribution and fragmentation functions, such as the Sivers and Collins functions; and transverse-momentum-integrated (collinear) quark-gluon-quark correlations, which are twist-3 distributions in the initial state proton or in the fragmentation process. For many of the experimentally accessible spin asymmetries, several of these functions can contribute, and need to be disentangled in order to understand the experimental data in detail, in particular the observed p_T dependence.

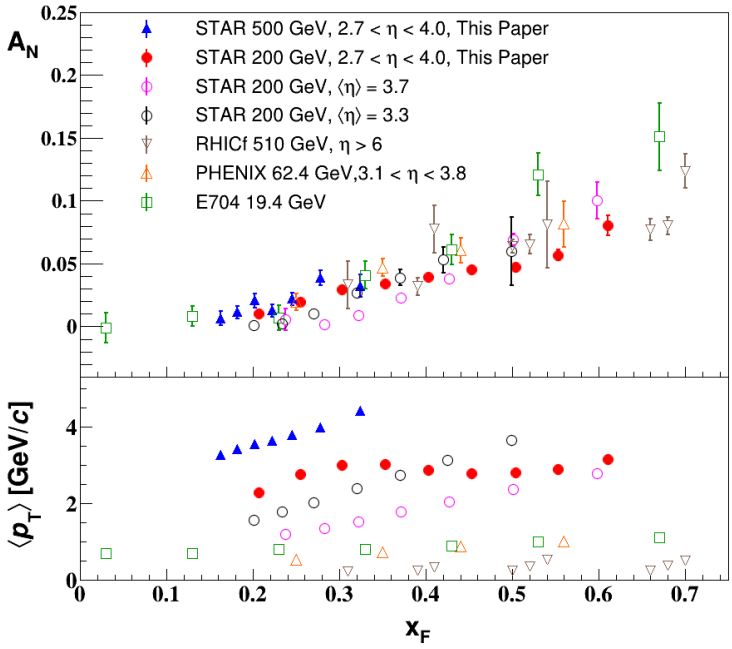

Figure 37: Transverse single-spin asymmetry A_N measurements for neutral pion in p+p collisions at different center-of-mass energies as a function of Feynman-x [110].

These functions manifest their spin dependence either in the initial state–for example, the Sivers distribution and its twist-3 analog, the Efremov-Teryaev-Qiu-Sterman (ETQS) function [111]–or in the final state via the fragmentation of polarized quarks, such as in the Collins function and related twist-3 function $\hat{H}_{FU}(z, z_z)$.

Incorporating the fragmentation term within the collinear twist-3 approach demonstrated the ability of this formalism to describe the large values of A_N for π^0 production observed at RHIC [112]. In this work, the relevant (non-pole) 3-parton collinear fragmentation function $\hat{H}_{FU}(z, z_z)$ was fit to the RHIC data. The so-called soft-gluon pole term, involving the ETQS function $T_{q,F}(x_1, x_2)$, was also included by fixing $T_{q,F}$ through its well-known relation to the TMD Sivers function $f_{1T}^{\perp}$. The authors obtained a very good description of the data due to the inclusion of the non-pole fragmentation function and based on this work they were able to make predictions for π^+ and π^- production asymmetries A_N at the forward rapidities covered by the STAR upgrades, $2.5 < \eta < 4$. The results are shown in Fig. 38 for $\sqrt{s}$= 200 and 500 GeV for two rapidity ranges, $2 < \eta < 3$ and $3 < \eta < 4$.

STAR recently published a pair of papers discussing forward transverse-spin asymmetries in p+p, p+Al, and p+Au collisions measured with the Forward Meson Spectrometer (FMS). One paper focuses on the dynamics that underlie the large asymmetries that have been seen to date [110]. The data show that A_N for forward π^0 production in p+p collisions at 200 and 500 GeV is substantially larger when the π^0 is isolated than when it is accompanied by additional nearby photons. The same analysis also shows that A_N for inclusive electromagnetic jets (EM-jets) in 200 and 500 GeV collisions is substantially larger than that for EM-jets

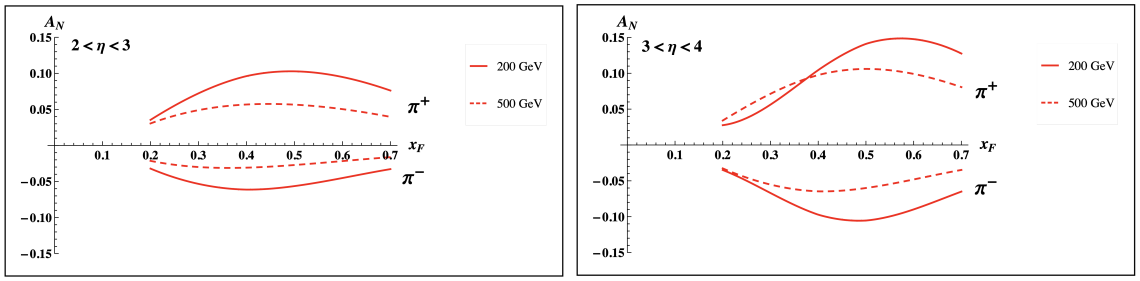

Figure 38: Predictions for A_N for π^+ and π^- production over the ranges $2 < \eta < 3$ (left) and $3 < \eta < 4$ (right) at $\sqrt{s} = 200$ GeV (solid lines) and 500 GeV (dashed lines).

that contain three or more photons and that the Collins asymmetry for π^0 in EM-jets is very small. The other paper focuses on the nuclear dependence of A_N for π^0 in $\sqrt{s_{NN}} = 200$ GeV collisions [113]. It presents a detailed mapping of A_N as functions of x_F and p_T for all three collision systems. It is shown that the observed nuclear dependence is very weak. The same analysis shows that isolated *vs.* non-isolated π^0 behave similarly in p+Al and p+Au collisions as they do in p+p collisions.

These two papers provide a wealth of new data to inform the ongoing discussion regarding the origin of the large inclusive hadron transverse-spin asymmetries that have been seen in p+p collisions at forward rapidity over a very broad range of collision energies. Nonetheless, the STAR Forward Upgrade is a game changer for such investigations. It enables measurements of A_N for $h^{+/-}$, in addition to π^0. It enables isolation criteria to be applied to the $h^{+/-}$ and π^0 that account for nearby charged, as well as neutral, fragments. It enables full jet asymmetry and Collins effect measurements, again for $h^{+/-}$ in addition to π^0, rather than just EM-jet measurements. It will permit all of these measurements to be performed in both p+Au (during Run-25) and p+p (measured during Run-24).

At 200 GeV we will perform the full suite of measurements in p+Au to identify any nuclear effects. Furthermore, it is important to stress that the 200 GeV running with the Forward Upgrade will give the unique opportunity for jet reconstruction studies at the exact same rapidity that is critical for the future EIC. The data will provide an extraordinary possibility to exercise new reconstruction techniques incorporating AI/ML methods and train the next generation of scientists.

2.1.2 Transversity and Collins Function

A complete picture of nucleon spin structure at leading twist must include contributions from the unpolarized and helicity distributions, as well as those involving transverse polarization, such as the transversity distribution [114–116]. The transversity distribution can be interpreted as the net transverse polarization of quarks within a transversely polarized proton. The difference between the helicity and transversity distributions for quarks and antiquarks provides a direct, x-dependent connection to nonzero orbital angular momentum components in the wave function of the proton [117]. Recently, the first lattice QCD calculation of the transversity distribution has been performed [118]. In addition, the measurement of transver-

sity has received substantial interest as a means to access the tensor charge of the nucleon, defined as the integral over the valence quark transversity: $\delta q^a = \int_0^1 [\delta q^a(x) - \delta \bar{q}^a(x)]\, dx$ [115, 119]. Measuring the tensor charge is very important for several reasons. First, it is an essential and fundamental quantity to our understanding of the spin structure of the nucleon. Also, the tensor charge can be calculated on the lattice with comparatively high precision, due to the valence nature of transversity, and hence is one of the few quantities that allow us to compare experimental results on the spin structure of the nucleon directly to *ab initio* QCD calculations. Finally, the tensor charge describes the sensitivity of observables in low-energy hadronic reactions to beyond the standard model physics processes with tensor couplings to hadrons. Examples are experiments with ultra-cold neutrons and nuclei.

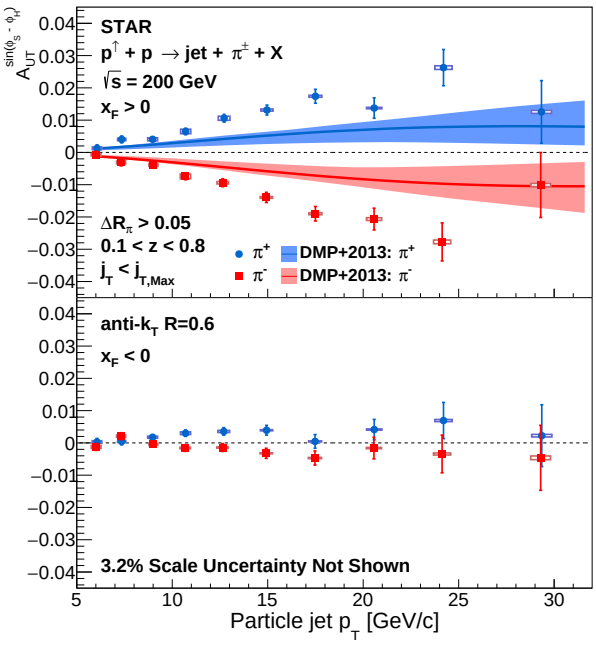

Figure 39: Collins asymmetry plotted for identified π^+ (blue) and π^- (red) particles as a function of jet p_{T} for jets that scatter forward relative to the polarized beam ($x_F > 0$) in the upper panel and those that scatter backward ($x_F < 0$) in the lower panel, extracted from data collected in 2012 and 2015 [120]. The full ranges of both z and j_{T} are integrated over. Theoretical evaluations from [121] with their uncertainties are presented for π^+ (blue) and π^- (red). Source: [120].

Transversity is difficult to access due to its chiral-odd nature, requiring the coupling of this distribution to another chiral-odd distribution. Semi-inclusive deep-inelastic scattering (SIDIS) experiments have successfully probed transversity through two channels: asymmetric distributions of single pions, convoluting the TMD transversity distribution with the TMD Collins fragmentation function, and azimuthally asymmetric distributions of di-hadrons, coupling transversity to the so-called Interference Fragmentation Function (IFF) in the framework of collinear factorization. Yet in spite of a wealth of lepton-scattering data, the kinematic reach of existing SIDIS experiments limits the precision with which the proton's transversity can be extracted, as the range of Bjorken-x values that can be accessed does not extend above $x_{\mathrm{Bj}} \sim 0.3$.

In p+p and p+Au collisions, the quark transversity distribution may be accessed via the single-spin asymmetries of the identified pions, kaons, and protons in high-energy jets through the coupling to the transverse momentum dependent Collins fragmentation function [121–

123]. This makes the Collins asymmetry in p+p and p+Au collisions a more direct probe of the Collins fragmentation function than SIDIS as the convolution with the TMD transversity distribution does not enter, and provides an ideal tool to explore the fundamental QCD questions of TMD factorization, universality, and evolution.

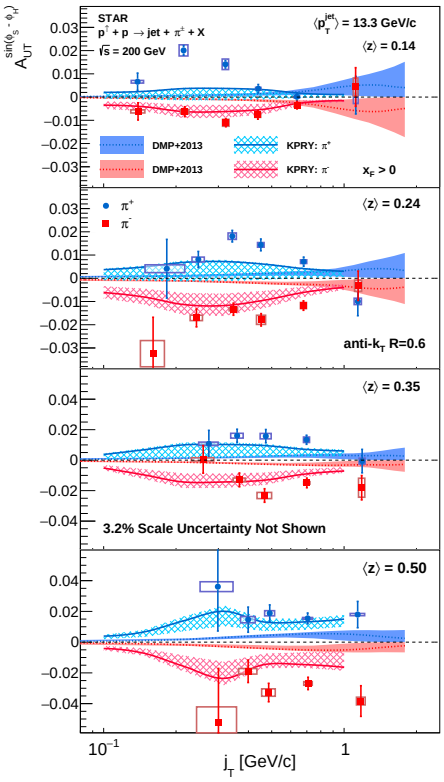

Figure 40: Collins asymmetry plotted for identified π^+ (blue) and π^- (red) particles as a function of j_T for four separate bins of hadron z, in jets with $p_T > 9.9$ GeV/c and $0 < \eta < 0.9$. Theoretical evaluations from [123] and [121] are also shown. Source: [120].

Figure 39 shows the recent results on combined 2012 and 2015 Collins asymmetries for charged pions within jets as a function of jet p_T [120]. By integrating over the hadron longitudinal and transverse momenta within the jets, Fig. 39 is sensitive primarily to the quark transversity. The measured asymmetries for jets that scatter forward relative to the polarized beam are larger than theoretical predictions [121], which are based on the transversity and Collins fragmentation function from SIDIS and e^+e^- processes within the TMD approach. Alternatively, the asymmetries can be expressed as functions of the fraction z of jet momentum carried by the hadron, and the momentum j_T of the pion transverse to the jet axis, as shown in Fig. 40. This provides a direct measurement of the kinematic dependence of the Collins fragmentation function. The findings include the j_T dependence which appears to vary with z, contrary to the assumptions of most current phenomenological models [121–123].

STAR has also published Collins asymmetry measurements from a smaller 500 GeV data set collected in 2011 [124]. With relatively limited statistics, the results are consistent with those at 200 GeV for overlapping x_T, despite sampling Q^2 that is larger by a factor of 6. Fig. 41 shows new preliminary results with much higher statistics 510 GeV data collected in 2017. The results are nicely aligned with 200 GeV results versus x_T, indicating almost no

energy dependence. These data provide unique insight into the Q^2 evolution of the Collins TMD fragmentation function. Analysis is also underway to determine the unpolarized TMD fragmentation functions.

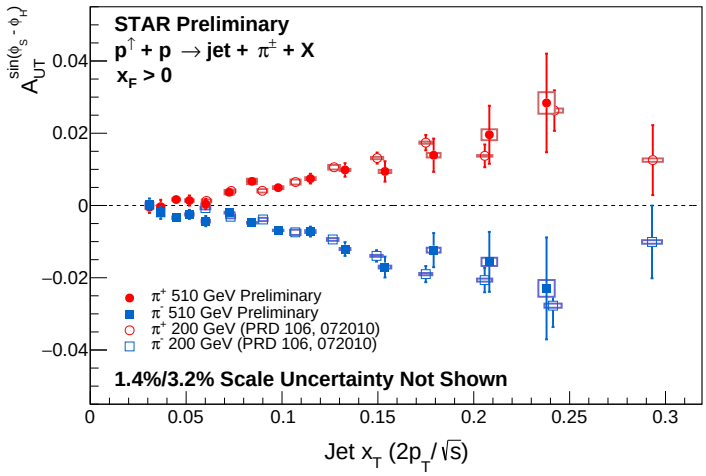

Figure 41: Collins asymmetries, $A_{UT}^{\sin(\phi_S-\phi_H)}$, as a function of jet x_T ($\equiv \frac{2p_T}{\sqrt{s}}$) for π^+/π^- in pp collisions at $\sqrt{s} = 510$ GeV (solid points), compared with previous results at $\sqrt{s} = 200$ GeV (open points). Vertical bars show the statistical uncertainties; boxes show the systematic uncertainties in x_T and A_{UT}. Source: [125].

Figure 42 shows that 200 GeV p+p /p+Au collisions interpolate between the kinematic coverage achieved with Run-22 data at high-x with the Forward Upgrade and at low-x with the STAR mid-rapidity detectors. They will also provide a coverage that spans in Q^2 by a factor of 6. This will provide valuable information about evolution effects, as well as cross-checks between measurements for various kinematic coverage. Furthermore, for most of the overlapping x region, 200 GeV p+Au and p+p collisions will also provide the greatest statistical precision (see for example Fig. 43), thereby establishing the most precise benchmark for future comparisons to ep data from the EIC. It is important to also recognize that the hadron-in-jet measurements with the STAR Forward Upgrade will provide valuable insight into jet detection close to beam rapidity that will guide the planning of future jet measurements in similar kinematics at the EIC.

STAR has a unique opportunity to extend the Collins effect measurements to nuclei. This will provide an alternative look at the universality of the Collins effect in hadron-production by dramatically increasing the color flow options. Breaking of factorization has been predicted for TMD PDFs similar to that for the Sivers effect [126, 127]. This will also explore the spin dependence of the hadronization process in cold nuclear matter. STAR collected a proof-of-principle data set during the 2015 p+Au run that is currently under analysis. Those data will provide a first estimate of medium-induced effects. However, the small nuclear effects seen by STAR for forward inclusive π^0 A_N [113] indicate that greater precision will likely be needed. Figure 43 shows the projected Run 15 and Run 24 statistical

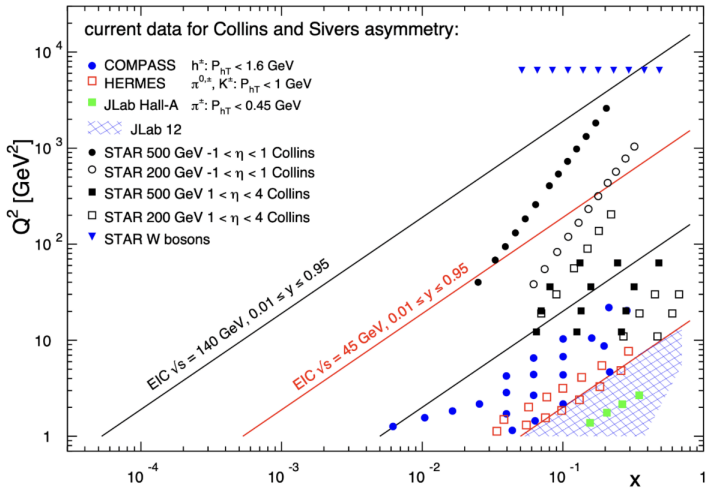

Figure 42: $x - Q^2$ coverage of RHIC measurements compared to existing Collins and Sivers effect measurements in SIDIS and the future coverage of the EIC.

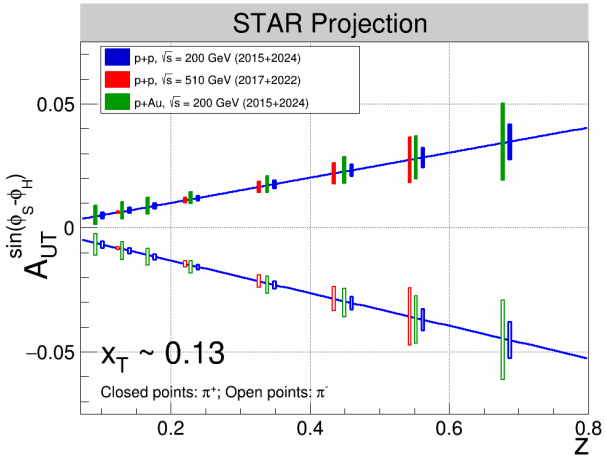

Figure 43: Projected statistical uncertainties for STAR Collins asymmetry measurements at $0 < \eta < 0.9$ in p+p at $\sqrt{s} = 200$ and 510 GeV and p–Au at $\sqrt{s_{\rm NN}} = 200$ GeV. The points have arbitrarily been drawn on the solid lines, which represent simple linear fits to the STAR preliminary 200 GeV p+p Collins asymmetry measurements from 2015. (Note that only one bin is shown spanning $0.1 < z < 0.2$ for 510 GeV p+p whereas three bins are shown covering the same z range for the 200 GeV measurements).

uncertainties for the p+Au Collins asymmetry measurement at $\sqrt{s_{\rm NN}} = 200$ GeV, compared to those for the p+p at the same energy.

2.1.3 Ultra-peripheral Collisions

The formalism of generalized parton distributions (GPDs) provides a theoretical framework which addresses some of the above questions [128–131]. Constraints on GPDs have mainly been provided by exclusive reactions in DIS, e.g. deeply virtual Compton scattering. RHIC, with its unique capability to collide transversely polarized protons at high energies, has the opportunity to measure A_N for exclusive J/Ψ production in ultra-peripheral collisions (UPCs) [132]. In such a UPC process, a photon emitted by the opposing beam particle (p or Au) collides with the polarized proton. The measurement is at a fixed $Q^2 \sim M^2_{J/\psi} \approx 10$

GeV^2 and $10^{-4} < x < 10^{-1}$. A nonzero asymmetry would be the first signature of a nonzero GPD E_g for gluons, which is sensitive to spin-orbit correlations and is intimately connected with the orbital angular momentum carried by partons in the nucleon and thus with the proton spin puzzle.

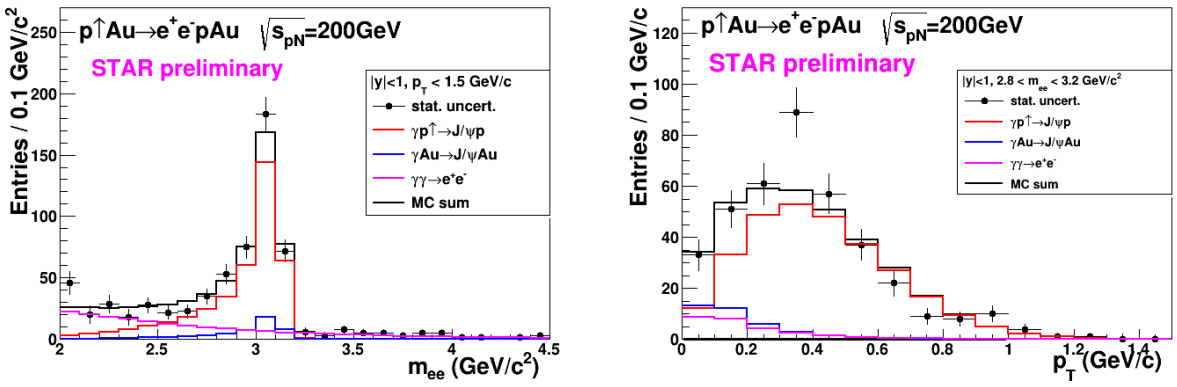

Figure 44: Mass distribution of selected e^+e^- pairs (left), and p_T distribution of the J/ψ mass peak (right). The colored histograms are the indicated processes modelled by STARlight and the sum fit to the data.

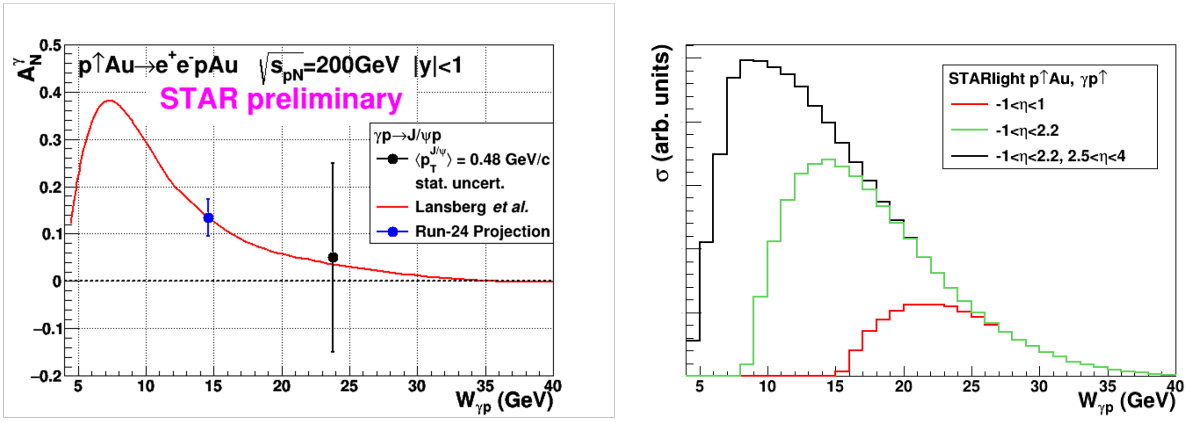

Figure 45: Left: The measured J/ψ transverse asymmetry A_N^γ and a prediction based on a parameterization of E_g. Right: The accepted cross section for γ+p↑→ J/ψ for various detector pseudorapidity η ranges; the black curve shows the result for the full STAR detector with the Forward Upgrade and the iTPC.

The Run-15 $p^\uparrow$+Au data allowed a proof-of-principle of such a measurement. A trigger requiring back-to-back energy deposits in the Barrel Electromagnetic Calorimeter selected J/Ψ candidates. The e^+e^- mass distribution after selection cuts is shown in the left of Fig. 44, and the pair p_T distribution of the J/ψ mass peak is shown on the right of that figure. The data are well described by the STARlight model [133] (colored histograms in the figure), including the dominant γ+p↑→J/ψ signal process and the γ+Au→J/ψ and γ+γ→e^+e^-

background processes. The left of Fig. 45 shows the STAR preliminary measurement (solid circle marker) of the transverse asymmetry A_N^γ for the J/ψ signal, which have a mean photon-proton center-of-mass energy $W_{\gamma p} \approx 24$ GeV. The result is consistent with zero. Also shown is a prediction based on a parameterization of E_g [134]; the present data provide no discrimination of this prediction.

This measurement can be greatly improved with a high statistics transversely polarized $p^\uparrow$–Au Run-25. The integrated luminosity for the UPC trigger used for the Run-15 measurement was 140 nb^{-1}; Run-25 will provide about 5 times more sampled luminosity (scenario 0 in Fig. 52), allowing for a moderate reduction of statistical uncertainty in the same $W_{\gamma p}$ range, but not allowing accurate comparison with the GPD model in that $W_{\gamma p}$ bin. However, the Forward Upgrade and iTPC will also provide a significant extension of the $W_{\gamma p}$ range of the measurement. The right panel of Fig. 45 shows the accepted cross section for γ+$p^\uparrow \rightarrow J/\psi$ for various detector pseudorapidity ranges. With the upgraded detector, the sensitive cross section is a factor of five times higher than the central barrel alone and the expected asymmetry is substantially larger. The projected statistical uncertainty on A_N^γ as shown in the left of Fig. 45 (blue square marker) offers a powerful test of a non-vanishing E_g. Also, the accepted region has a lower mean $W_{\gamma p} \approx 14$ GeV. Predictions based on E_g parameterizations such as shown in figure 45 have a larger asymmetry at lower $W_{\gamma p}$. Alternatively, the increased statistics will enable a differential measurement of A_N^γ as a function of $W_{\gamma p}$.

The UPC cross section scales with Z^2 of the the nucleus emitting the photon; for protons this is $1/79^2$ relative to Au nuclei, which makes analogous measurements in p+p collisions extremely luminosity-hungry. Therefore, the p+Au run is important for this measurement.

2.2 Physics Opportunities with Unpolarized p+Au Collisions

Our quest to understand QCD processes in Cold Nuclear Matter (CNM) centers on the following fundamental questions:

- Can we experimentally find evidence of a novel universal regime of non-linear QCD dynamics in nuclei?
- What is the role of saturated strong gluon fields, and what are the degrees of freedom in this high gluon density regime?
- What is the fundamental quark-gluon structure of light and heavy nuclei?
- Can a nucleus, serving as a color filter, provide novel insight into the propagation, attenuation and hadronization of colored quarks and gluons?

Various aspects of these questions have been addressed by numerous experiments and facilities around the world, most of them at significantly lower center-of-mass energies and kinematic reach than RHIC. Deep inelastic scattering on nuclei addresses some of these questions with results from, for instance, HERMES at DESY [135–137], CLAS at JLab [138],

and in the future from the JLab 12 GeV. This program is complemented by hadron-nucleus reactions in fixed target p+A at Fermilab (E772, E886, and E906) [139] and at the CERN-SPS.

In the following we propose a measurement program unique to RHIC to constrain the initial state effects in strong interactions in the nuclear environment. We also highlight the complementarity to the LHC p+Pb program and stress why RHIC data are essential and unique in the quest to further our understanding of nuclei. The uniqueness of the RHIC program is based on the flexibility of the RHIC accelerator to run collisions of different particle species at very different center-of-mass energies. This in combination with the enhanced STAR detector capabilities in Run-25 allows to disentangle nuclear effects in the initial and final state as well as leading twist shadowing from saturation effects in a kinematic regime where all these effects are predicted to be large. Most of the discussed measurements critically rely on the Forward Upgrade.

2.2.1 The Initial State of Nuclear Collisions

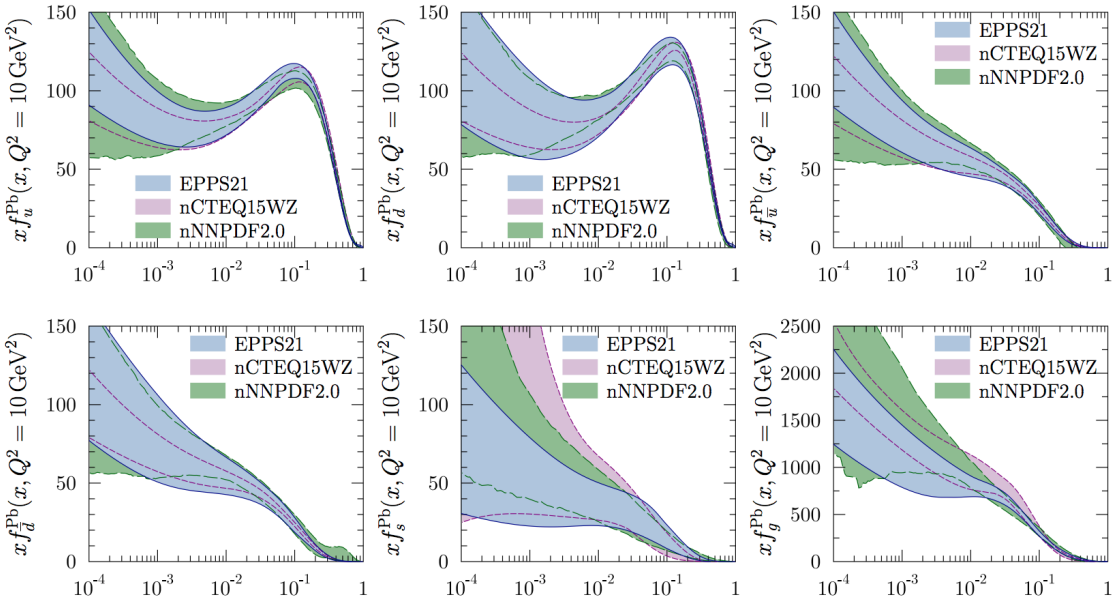

Figure 46: Summary of the most recent sets of nPDFs at 90% confidence-level. [140]

Nuclear parton distribution functions: A main emphasis of the Run-15 and later p+A runs is to determine the initial conditions of the heavy ion nucleus before the collision to support the theoretical understanding of the A–A program both at RHIC and the LHC. In the following, the current status of nPDFs will be discussed, including where the unique contributions of RHIC lie, in comparison to the LHC and the future EIC.

Our current understanding of nuclear parton distribution functions (nPDFs) is still very limited, in particular, when compared with the rather precise knowledge of PDFs for free protons collected over the past 30 years. Figure 46 shows an extraction of nPDFs from available data, along with estimates of uncertainties. All results are shown in terms of the nuclear modification ratios, i.e., scaled by the respective PDF of the free proton. The kinematic coverage of the data used in the EPPS21 fits [140] are shown in Fig. 47. Clearly, high precision data at small x and for various different values of Q^2 are needed to better constrain the magnitude of suppression in the x region where non-linear effects in the scale evolution are expected. In addition, such data are needed for several different nuclei, as the A-dependence of nPDFs cannot be predicted from first principles in pQCD and, again, currently relies on assumptions. The PHENIX midrapidity $\pi^0 R_{dAu}$ data [141], are the only data which can probe the gluon in the nucleus directly, but these data also suffer from unknown nuclear effects in the final state (see [142]). Therefore, it is critical to have high precision data only sensitive to nuclear modification in the initial state over a wide range in x and intermediate values of Q^2 (away from the saturation regime) to establish the nuclear modification of gluons in this kinematic range.

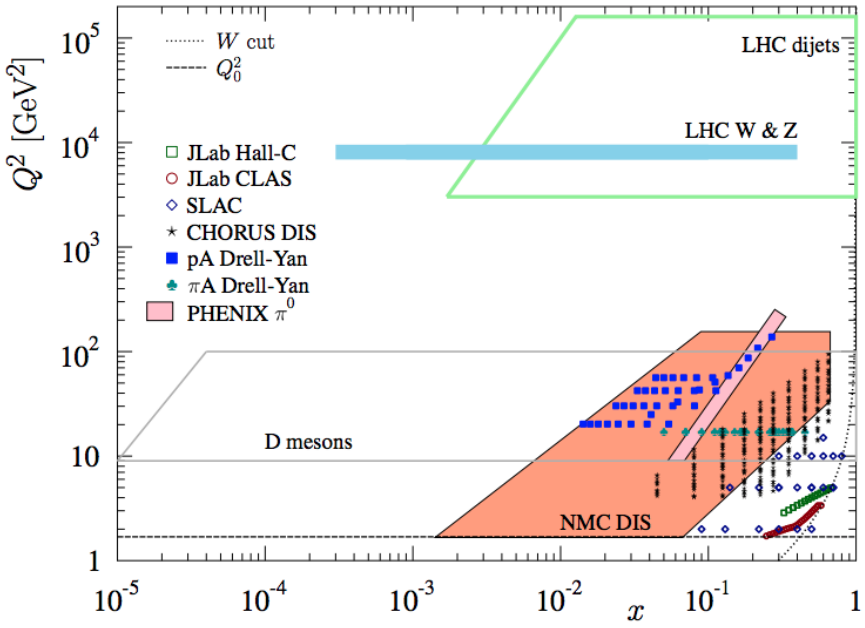

Figure 47: The kinematic x and Q^2 coverage of data used in the EPPS21 nPDF fits. [140]

It is important to realize that the measurements from RHIC are compelling and essential even when compared to what can be achieved in p–Pb collisions at the LHC. Due to the higher center-of-mass system energy most of the LHC data have very high Q^2, where the nuclear effects are already reduced significantly by evolution and are therefore very difficult to constrain.

RHIC has the *unique* capability to provide data in a kinematic regime (moderate Q^2 and

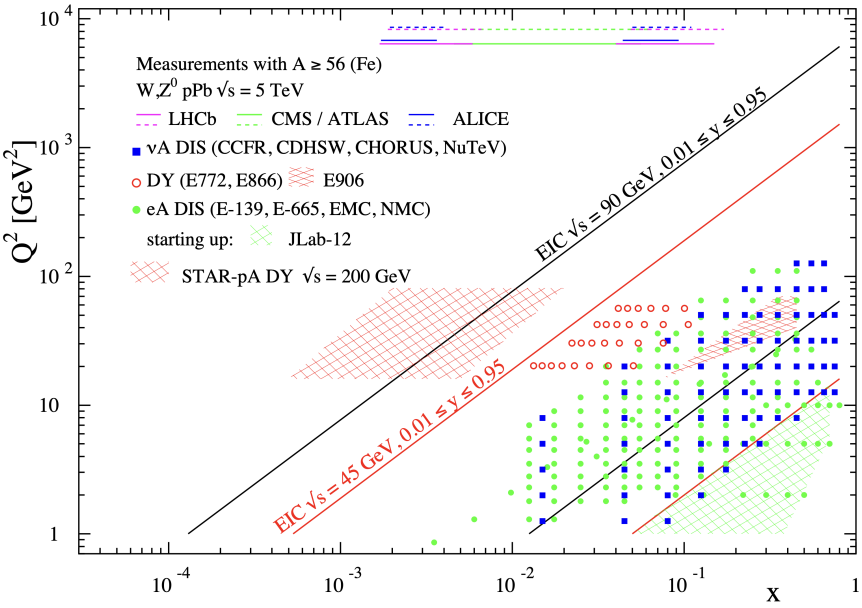

Figure 48: The kinematic coverage in $x - Q^2$ of past, present and future experiments constraining nPDFs with access to the exact parton kinematics event-by-event and no fragmentation in the final state.

medium-to-low x) where the nuclear modification of the sea quark and the gluon is expected to be sizable. In addition, and unlike the LHC, RHIC has the potential to vary the nucleus in p+A collisions and as such also constrain the A-dependence of nPDFs.

Extraction of this information is less ambiguous if one uses processes in which strong (QCD) final-state interactions can be neglected or reduced. Such golden channels would include a measurement of R_{pA} for Drell-Yan production at forward pseudo-rapidities with respect to the proton direction ($2.5 < \eta < 4$) to constrain the nuclear modifications of sea-quarks. Moreover, the R_{pA} for direct photon production in the same kinematic regime will help constrain the nuclear gluon distribution. Data for the first measurement of R_{pA} for direct photon production have already been taken during the p+Au and p+Al Run-15, with recorded luminosities by STAR of $L_{pAu} = 0.45$ pb^{-1} and $L_{pAl} = 1$ pb^{-1}, respectively. Like all other inclusive probes in p+p and p+A collisions, e.g., jets, no access to the exact parton kinematics can be provided event-by-event but global QCD analyses easily account for that. After the p+Au Run-25, the statistical precision of the prompt photon data will be sufficient to contribute to a stringent test of the universality of nuclear PDFs when combined with the expected data from the EIC (see Figure 2.22 and 2.23 in Ref [143]). The Forward Upgrade with its tracking at forward rapidities will also provide the possibility to measure R_{pA} for positive and negatively charged hadrons. Approximately equal nucleon-nucleon luminosities for p+p and p+Au are important for the optimization of R_{pA} measurements as they directly compare the same observable - yields - in both collision systems.

Figure 48 shows the kinematic coverage in x–Q^2 of past, present, and future experiments capable of constraining nuclear parton distribution functions. The shown experiments provide measurements that access the initial state parton kinematics on an event-by event basis (in a leading order approximation) while remaining insensitive to any nuclear effects in the final state. Some of the LHC experiments cover the same x-range as DY at forward pseudo-

rapidities at RHIC but at a much higher scale Q^2, where nuclear modifications are already significantly reduced [144–146]. At intermediate Q^2, DY at STAR will extend the low-x reach by nearly one decade compared to EIC.

The biggest challenge of a DY measurement is to suppress the overwhelming hadronic background: the total DY cross-section is about 10^{-5} to 10^{-6} smaller than the corresponding hadron production cross-sections. Therefore, the probability of misidentifying a hadron track as a lepton has to be suppressed to the order of 0.1% while maintaining reasonable electron detection efficiencies. To that end, we have studied the combined electron/hadron discriminating power of the Forward Upgrade. It was found that by applying multivariate analysis techniques to the features of EM/hadronic shower development and momentum measurements we can achieve hadron rejection powers of 200 to 2000 for hadrons of 15 GeV to 50 GeV with 80% electron detection efficiency.

The potential impact of the DY R_{pA} data for the EPPS-19 sets of nPDFs was studied through a re-weighting procedure. [147] We expect a significant impact on the uncertainties of R_{pA} DY upon including the projected and properly randomized data. Clearly, the DY data from RHIC will be instrumental in reducing present uncertainties in nuclear modifications of sea quarks. Again, these data will prove to be essential in testing the fundamental universality property of nPDFs in the future when EIC data become available.

STAR's unique detector capabilities provide data on J/Ψ-production in ultra-peripheral collisions. This measurement can provide access to the spatial gluon distribution by measuring the t-dependence of $d\sigma/dt$. To study the gluon distribution in the gold nucleus, events need to be tagged where the photon is emitted from the proton (γ+Au$\rightarrow$ J/ψ). However, with the signal-to-background ratio in p+Au collisions (see the contribution from the γ+Au$\rightarrow$ J/ψ process and the background processes in Fig. 44), we expect much better sensitivity to the gluon distributions in Au from the Au+Au program. In addition to J/ψ photoproduction in UPC for exclusive reactions, photoproduction of back-to-back jets is also sensitive the PDFs (nPDFs in Au+Au UPC). This measurement has never been performed at RHIC experiments, where the kinematic coverage can go to moderate to high-x. The anti-shadowing region in nuclei, for example, is of great interest by comparing to this measurement in the proton. Furthermore, we can possibly extend the measurement from inclusive photoproduction dijets to diffractive dijets in p+p and p+Au collisions, which will be sensitive to the QCD factorisation breaking [86]. For details, see Sec. 1.2 for discussion in UPCs.

Non-linear QCD effects: Our understanding of the proton structure and of the nuclear interactions at high energy would be advanced significantly with the definitive discovery of the saturation regime. [148–154] Saturation physics would provide an infrared cutoff for perturbative calculations, the saturation scale Q_s, which grows with the atomic number of the nucleus A and with decreasing value of x. If Q_s is large it makes the strong coupling constant small, $\alpha_s(Q_s^2) << 1$ allowing for perturbative QCD calculations to be under theoretical control.

It is well known that PDFs grow at small-x. If one imagines how such a high number of

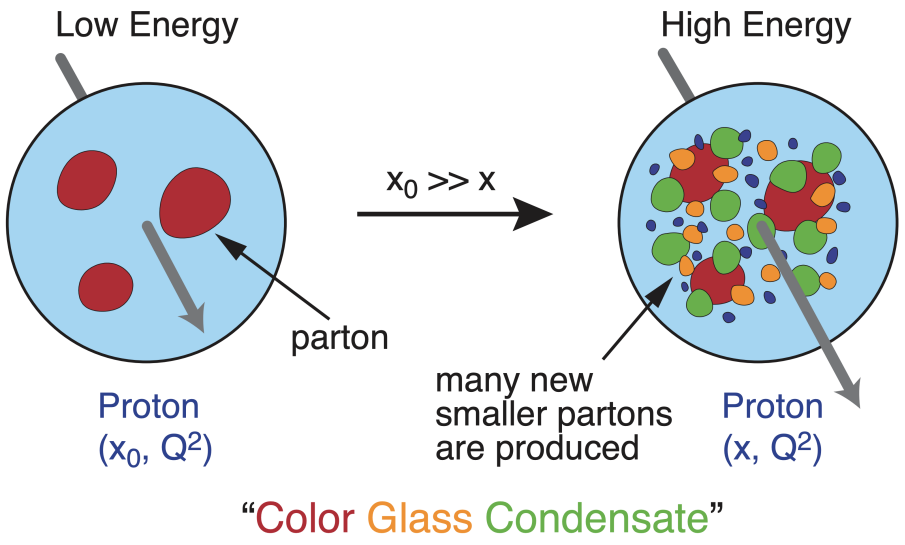

Figure 49: Proton wave function evolution towards small-x.

small-x partons would fit in the (almost) unchanged proton radius, one arrives at the picture presented in Fig. 49: the gluons and quarks are packed very tightly in the transverse plane. The typical distance between the partons decreases as the number of partons increases, and can get small at low-x (or for a large nucleus instead of the proton). One can define the saturation scale as the inverse of this typical transverse inter-parton distance. Hence Q_s indeed grows with A and decreasing x.

The actual calculations in saturation physics start with the classical gluon fields (as gluons dominate quarks at small-x) [155–161], which are then evolved using the nonlinear small-x BK/JIMWLK evolution equations. [162, 163, 163–171] The saturation region can be well-approximated by the following formula: $Q_s^2 \sim (A/x)^{1/3}$. Note again that at small enough x the saturation scale provides an IR cutoff, justifying the use of perturbative calculations. This is important beyond saturation physics, and may help us better understand small-x evolution of the TMDs.

While the evidence in favor of non-linear QCD effects has been gleaned from the data collected at HERA, RHIC and the LHC, the case for saturation is not sealed and alternative explanations of these data exist. The EIC is slated to provide more definitive evidence for saturation physics. [109] To help the EIC complete the case for saturation, it is mandatory to generate higher-precision measurements in p+Au collisions at RHIC. These higher-precision measurements would significantly enhance the discovery potential of the EIC as they would enable a stringent test of universality of the CGC. We stress again that a lot of theoretical predictions and results in the earlier Sections of this document would greatly benefit from this physics: the small-x evolution of TMDs in a longitudinally or transversely polarized proton, or in an unpolarized proton, can all be derived in the saturation framework [172] in a theoretically better-controlled way due to the presence of Q_s. Hence non-linear QCD effects may help us understand both the quark and gluon helicity PDFs as well as the Sivers

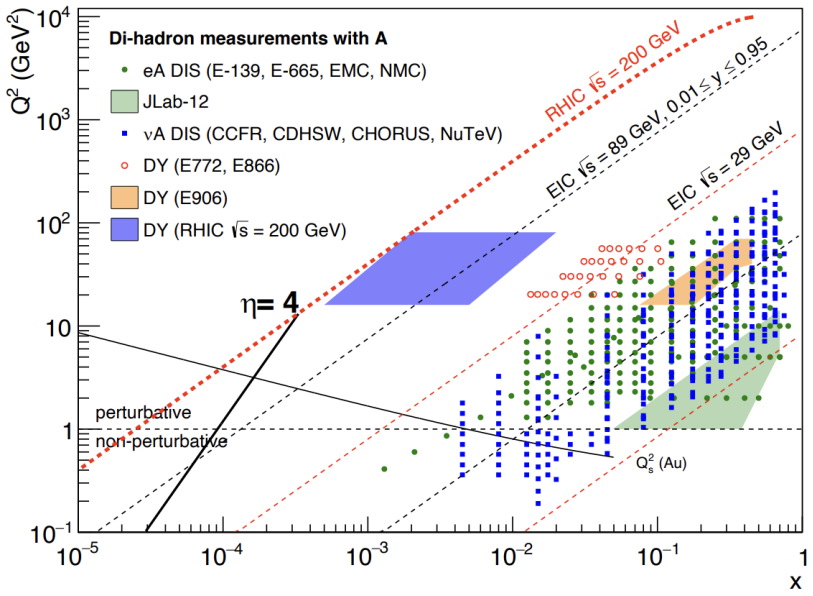

Figure 50: Kinematic coverage in the $x - Q^2$ plane for p+A collisions at RHIC, along with previous e+A measurements, the kinematic reach of an electron-ion collider, and estimates for the saturation scale Q_s in Au nuclus and the line illustrating the range in x and Q^2 covered with hadrons at rapidity $\eta = 4$.

and Boer-Mulders functions.

The saturation momentum is predicted to grow approximately like a power of energy, $Q_s^2 \sim E^{\lambda/2}$ with $\lambda \sim 0.2 - 0.3$, as phase space for small-x (quantum) evolution opens up. The saturation scale is also expected to grow in proportion to the valence charge density at the onset of small-x quantum evolution. Hence, the saturation scale of a large nucleus should exceed that of a nucleon by a factor of $A^{1/3} \sim 5$ (on average over impact parameters). RHIC is capable of running p+A collisions for different nuclei to check this dependence on the mass number. This avoids potential issues with dividing, e.g., p–Pb collisions in N_{part} classes . [173] Figure 50 shows the kinematic coverage in the $x - Q^2$ plane for p+A collisions at RHIC, along with previous e+A measurements and the kinematic reach of an EIC. The saturation scale for a Au nucleus is also shown. To access at RHIC a kinematic regime sensitive to non-linear QCD effects with $Q^2 > 1$ GeV^2 requires measurements at forward rapidities. For these kinematics the saturation scale is moderate, on the order of a few GeV^2, so measurements sensitive to non-linear QCD effects are by necessity limited to semi-hard processes.

Until today the golden channel at RHIC to observe strong hints of non-linear QCD effects has been the angular dependence of two-particle correlations, because it is an essential tool for testing the underlying QCD dynamics. [173] In forward-forward correlations facing the $p(d)$ beam direction one selects a large-x parton in the $p(d)$ interacting with a low-x parton in the nucleus. For $x < 0.01$ the low-x parton will be back-scattered in the direction of the large-x parton. Due to the abundance of gluons at small x, the backwards-scattered partons are dominantly gluons, while the large-x partons from the $p(d)$ are dominantly quarks. The measurements of di-hadron correlations by STAR and PHENIX [174, 175], have been compared with theoretical expectations using the CGC framework based on a fixed saturation scale Q_s and considering valence quarks in the deuteron scattering off low-x gluons in the nucleus with impact parameter $b = 0$. [176, 177] Alternative calculations [178]

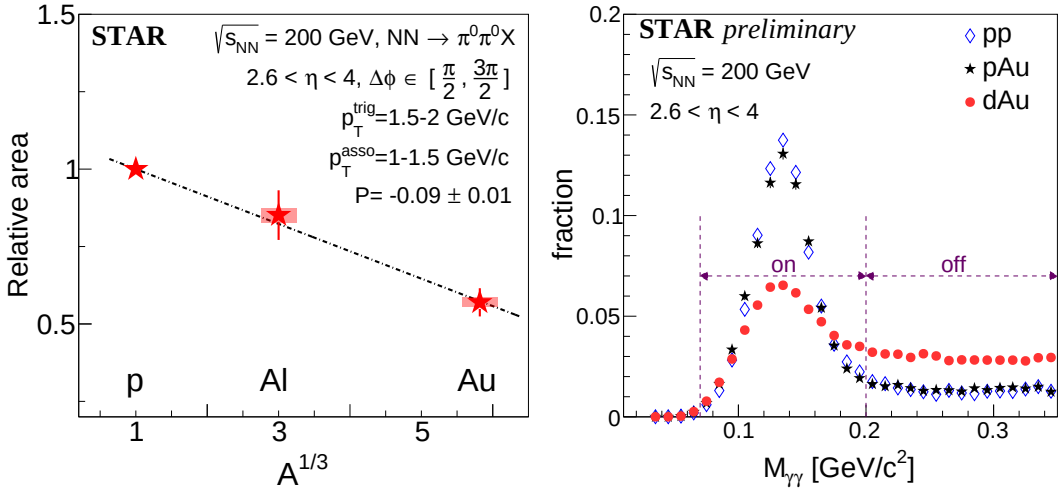

Figure 51: Left: Relative area of back-to-back di-π^0 correlations at forward pseudorapidities ($2.6 < \eta < 4.0$) in p+Au and p+Al relative to p+p collisions for $p_T^{\rm trig}$ = 1.5−2 GeV/c and $p_T^{\rm asso}$ = 1−1.5 GeV/c. The vertical bars for the Al and Au ratios indicate the statistical uncertainties and the vertical bands indicate the systematic uncertainties. The data points are fitted by a linear function, whose slope (P) is found to be -0.09 ± 0.01. Right: The invariant mass spectra for di-photon in p+p, p+Au, and d+Au. The on mass range is chosen as 0.07-0.2 GeV/c^2, the off mass range is 0.2-0.35 GeV/c^2.

based on both initial and final state multiple scattering that determine the strength of this transverse momentum imbalance, in which the suppression of the cross-section in d+Au collisions arises from cold nuclear matter energy loss and coherent power corrections, have also been very successful to describe the data.

The p+A Run-15 at RHIC has provided unique opportunities to study this channel in more detail at STAR. The high delivered integrated luminosities allow one to vary the trigger and associated particle p_T from low to high values and thus crossing the saturation boundary as shown in Fig. 50 and reinstate the correlations for central p+A collisions for forward-forward π^0's. Studying di-hadron correlations in p+A collisions instead of d+A collisions has a further advantage. In reference [179], the authors point out that the contributions from double-parton interactions to the cross-sections for $dA \rightarrow \pi^0\pi^0 X$ are not negligible. They find that such contributions become important at large forward rapidities, and especially in the case of d+A scattering. Figure 51 left shows the relative area of back-to-back di-π^0 correlations in p+Al and p+Au collisions relative to p+p collisions. The results show suppression with increasing A, and an enhanced suppression that scales as $A^{1/3}$. This behavior is consistent with different calculations based on the CGC formalism and is a clear hint of non-linear effects. A comparison between p+p (Run-15), p+Au (Run-15), and d+Au (Run-16) collisions can help provide insight into the contributions from multiple parton scattering [179]. Figure 51 shows the invariant mass spectra for final p+p and p+Au results and the preliminary d+Au. It is clear from the comparison that there is significantly more background in the the d+Au data than the p+p and p+Au data. This combinatoric

correlation dominates in d+Au collisions, which makes it very challenging to identify the signal correlation. The forward di-π^0 correlation measurement favors the cleaner p+A collisions rather than d+A collisions. Run-25 will be able to measure di-hadron correlations taking advantage of the cleaner p+Au collisions and the extended pseudorapidity reach of the Forward Upgrade detectors.

The statistical projections of di-π^0 and di-$h^{\pm}$ measurements for Run-24 p+p and Run-25 p+Au data are shown in Fig. 53 with various assumptions regarding Run-25 p+Au data taking. Five scenarios for were considered, with the details shown in Tab. 2. Note that these scenarios were prepared specifically for Run-24 with three conditions for the total Cyro weeks as 28, 24, and 20, and split p+p and p+Au data taking to provide equal nucleon-nucleon luminosities. During the just ended-Run24, we collected 164 pb^{-1} of p+p data, i.e., achieving the Scenario S0 with p+p . The effects of different p+Au physics weeks in Run-25, persist in the projections of Fig. 53.

Table 2: Five scenarios for the data taking during Run-24:

Scenarios	Cyro weeks [w]	Set-up [w]	p+p [w]	p+A [w]	Details
S0	28	5.5	12	10.5	equal nucleon-nucleon luminosity
S1	28	5.5	11.3	11.2	equal time
S2	28	5.5	17.5	5	request from the last PAC
S3	24	5.5	9.5	9	equal nucleon-nucleon luminosity
S4	20	5.5	7.5	7	equal nucleon-nucleon luminosity

	p+p			p+Au		
Year	2015	2024		2015	2024	
$\sqrt{s}$ [GeV]	200	200		200	200	
Lumi/week [$\frac{pb^{-1}}{week}$]	-	(25+17)/2 = 21		-	(0.14+0.1)/2 = 0.12	
Num of weeks Integrated Lumi. [pb^{-1}]	Num of weeks 10.9 Integrated Lumi. [pb^{-1}] 105	Num of weeks S0: 12 S1: 11.3 S2: 17.5 S3: 9.5 S4: 7.5	Integrated Lumi. [pb^{-1}] S0: 142 S1: 132 S2: 216 S3: 108 S4: 81	Num of weeks 5.1 Integrated Lumi. [pb^{-1}] 0.45	Num of weeks S0: 10.5 S1: 11.2 S2: 5 S3: 9 S4: 7	Integrated Lumi. [pb^{-1}] S0: 0.69 S1: 0.75 S2: 0.27 S3: 0.58 S4: 0.42

Figure 52: Estimated sampled luminosity of p+p and p+A in Run-24.

For each scenario, the estimated sampled luminosity for p+p and p+Au can be found in Fig. 52. The luminosity per week for Run-24 p+p and p+Au comes from the latest projection from CAD, which is the averaged number between maximum and minimum luminosity per week. According to CAD's luminosity guidance for Run-24, the maximum luminosity per

week for p+p is 25 pb^{-1} and the minimum luminosity per week is 17 pb^{-1}; the maximum luminosity per week for p+Au is 0.14 pb^{-1} and the minimum luminosity per week is 0.1 pb^{-1}, which indicates the performance is going to be worse than Run-15. Especially for S2, which was requested to be considered by the last PAC meeting, the integrated luminosity for p+Au is 0.27 pb^{-1} which is only 60% of the luminosity we collected in Run-15. Please note that, with the updated CAD projection for Run-25, the expected p+Au luminosity with 5 weeks p+Au data taking is 0.22 pb^{-1}.

In Fig. 53, the back-to-back di-π^0 and di-$h^{\pm}$ yields in p+Au with respect to p+p collisions are presented as a function of the associated particle's p_T. The black open circles represent the data points published with Run-15 data with only statistical errors [180]. The rest are the projected statistical errors for Run-24, with the central value located on the fitting function from the Run-15 data. For the di-π^0 channel, S0 and S1 show similar performance in reducing the statistical uncertainty 13%-14% compared to Run-15 results. S2 with only 5 weeks of p+Au running indicates a 2% increase of the statistical error compared to Run-15, which leads no improvement. The conclusion is worse for those analyses that only depend on p+Au data, without comparison to p+p such as the GPD and Collins asymmetry measurements.

Figure 53(right) presents the projected statistical errors for the di-$h^{\pm}$ channel, which is the golden channel to quantitatively probe gluon saturation. The forward tracking system enables us to detect charged hadrons in the forward region ($2.6 < \eta < 4.0$) at low p_T (down to 0.2 GeV/c). Lower p_T enables us to probe the lower x region in the phase space, where saturation is predicted to be stronger. So, with this channel, we are expecting to observe the largest suppression of the back-to-back di-$h^{\pm}$ correlations in p+Au with respect to p+p collisions at RHIC energy. With enough statistics for Run-25, STAR can further investigate the nonlinear QCD phenomena in the region closer to gluon saturation, where Run-15 data cannot access. In the extreme case of only 5 weeks for p+Au physics running in Run-25, a reasonable precision can still be obtained with this channel.

In Fig. 53(right), the statistical errors are estimated through a different way compared to the di-π^0 channel, as for low p_T (< 1 GeV/c) we will use min-bias triggered data and for high p_T (> 1 GeV/c) we will use high-p_T data triggered by the forward calorimeters. Considering the prescale, we used the estimated number of events for Run-25 compared with the number of events recorded in Run-15 for both p+p and p+Au collisions, to calculate the statistical errors of Run-25. The number of events for Run-25 is

$$N_{evt} = \text{event rate} \times N_{week} \times N_{day} \times N_{min} \times N_{sec} \times t_{up} \times t_{live} \times eff_{trk} \tag{4}$$

where the recorded min-bias event rate is assumed to be 500 Hz, $t_{up} = 50\%$, $t_{live} = 70\%$, and the tracking efficiency is $eff_{trk} = 90\%$. Since the yield of di-$h^{\pm}$ pairs is much larger than di-π^0, overall we will obtain much smaller statistical errors for the Run-25 di-$h^{\pm}$ channel compared to di-π^0 results from Run-15.

It is important to note that for the measurements to date in $p(d)$+A collisions both initial and final states interact strongly, leading to severe complications in the theoretical treatment (see [182,183], and references therein). As described in detail in the Section above, in p+Au collisions, these complications can be ameliorated by removing the strong interaction from

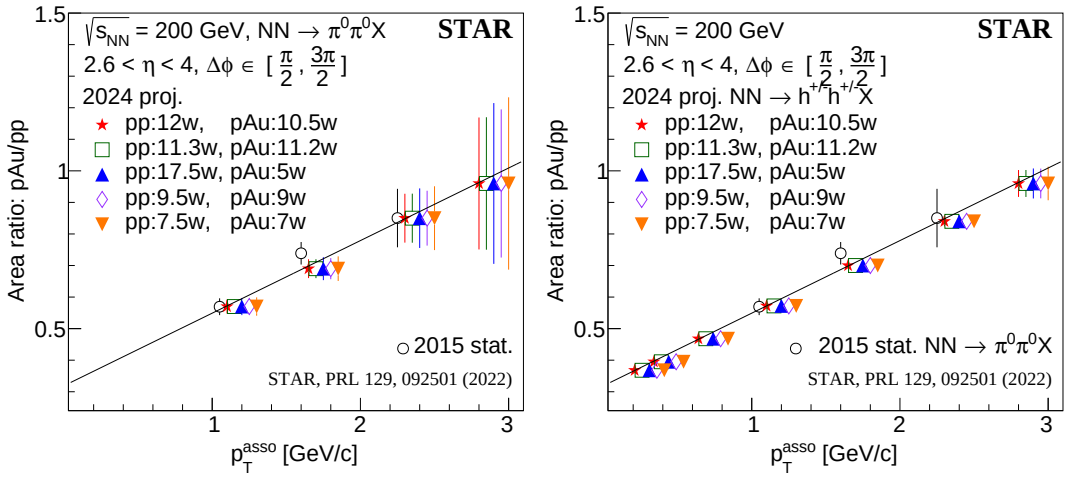

Figure 53: Relative area of back-to-back di-π^0 (Left) and di-$h^{\pm}$ (Right) correlations at forward pseudorapidities ($2.6 < \eta < 4.0$) in p+Au for Run-25 data with respect to p+p collisions (Run-24), in comparison with the published Run-15 di-π^0 results. The black open circles represent the published Run-15 di-π^0 data points with statistical errors only. The rest of the data points come from the projected statistical errors under different data-taking assumptions (Tab. 2) for Run-24.

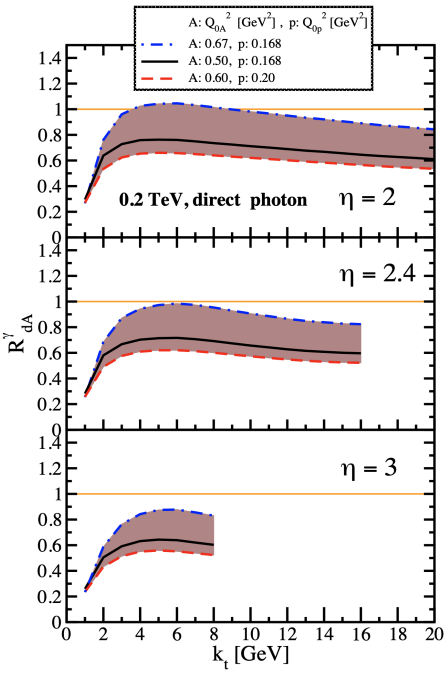

Figure 54: Nuclear modification factor for direct photon production in $p(d)$+A collisions at various rapidities at RHIC $\sqrt{s} = 200$ GeV. The curves are the results obtained from Eq. (12) in Ref. [181] and the solution to rcBK equation using different initial saturation scales for a proton Q_{op} and a nucleus Q_{oA}. The band shows our theoretical uncertainties arising from allowing a variation of the initial saturation scale of the nucleus in a range consistent with previous studies of DIS structure functions as well as particle production in minimum-bias p+p, p+A and A+A collisions in the CGC formalism, see Ref. [181] for details.

the final state, by using photons and Drell-Yan electrons. The Run-15 p+Au run will for the first time provide data on R_{pA} for direct photons and therefore allow one to test CGC based predictions on this observable as depicted in Fig. 54 (taken from Ref. [181]). The higher delivered integrated luminosity for the upcoming p+Au Run-25 together with the Forward Upgrade will enable one to study more luminosity hungry processes and/or complementary probes to the di-π^0 correlations, i.e. di-hadron correlations for charged hadrons, photon-jet, photon-hadron and di-jet correlations, which will allow a rigorous test of the calculation in the CGC formalism. It is important to stress that the comparison of these correlation probes in p+p and p+Au requires approximately equal nucleon-nucleon luminosities for these two collision systems for optimal measurements. It is noted that these results are crucial for the equivalent measurements at an EIC, which are planned at close to identical kinematics, because only if non-linear effects are seen with different complementary probes, i.e., $e + A$ and $p + A$, one can claim a discovery of saturation effects and their universality.

We use direct photon plus jet (direct γ+jet) events as an example channel to indicate what can be done in Run-25. These events are dominantly produced through the gluon Compton scattering process, $g + q \rightarrow \gamma + q$, and are sensitive to the gluon densities of the nucleon and nuclei in p+p and p+A collisions. Through measurements of the azimuthal correlations in p+A collisions for direct γ+jet production, one can study non-linear effects at small-x. Unlike di-jet production that is governed by both the Weizsäcker-Williams and dipole gluon densities, direct γ+jet production only accesses the dipole gluon density, which is better understood theoretically. [181, 184] On the other hand, direct γ+jet production is experimentally more challenging due to its small cross-section and large background contribution from di-jet events in which photons from fragmentation or hadron decay could be misidentified as direct photons. The feasibility to perform direct γ+jet measurements with the Forward Upgrade in unpolarized p+p and p+Au collisions at $\sqrt{s_{\rm NN}} = 200$ GeV has been studied. PYTHIA-8.189 [185] was used to produce direct γ+jet and di-jet events. In order to suppress the di-jet background, the leading photon and jet are required to be balanced in transverse momentum, $|\phi^{\gamma} - \phi^{jet}| > 2\pi/3$ and $0.5 < p_T^{\gamma}/p_T^{jet} < 2$. Both the photon and jet have to be in the forward acceptance $1.3 < \eta < 4.0$ with $p_T > 3.2$ GeV/c in 200 GeV p+p collisions. The photon needs to be isolated from other particle activities by requiring the fraction of electromagnetic energy deposition in the cone of $\Delta R = 0.1$ around the photon is more than 95% of that in the cone of $\Delta R = 0.5$. Jets are reconstructed by an anti-k_T algorithm with $\Delta R = 0.5$. After applying these selection cuts, the signal-to-background ratio is around 3:1 [186]. The expected number of selected direct γ+jet events is around ~ 0.9M at $\sqrt{s_{\rm NN}} = 200$ GeV in p+Au collisions for the proposed Run-25. We conclude that a measurement of direct photon-jet correlation from p+Au collisions is feasible, which is sensitive to the gluon density in $0.001 < x < 0.005$ in the Au nucleus where parton saturation is expected.

There are other potential opportunities with the upcoming p+Au runs that can provide a clean baseline for studying the gluon saturation phenomena in Au+Au using ultra-peripheral collisions (UPC). For example, one of the most powerful measurements proposed at the EIC for discovery of gluon saturation is to look at the double ratio between a heavy nucleus

and proton in terms of diffractive processes, see details in Sec. 1.2. With STAR Run-25, the p+Au UPC may provide two important measurements, e.g., exclusive and inclusive J/ψ production off the proton target, which will serve as a baseline for no saturation. The same measurement will be performed in Au+Au UPC with Run-20 and 25. The different system comparison with STAR data may provide strong evidence for gluon saturation.

2.2.2 The Final State-Fragmentation Functions

Fragmentation functions: In spite of the remarkable phenomenological successes of QCD, a quantitative understanding of the hadronization process is still one of the great challenges for the theory. Hadronization describes the transition of a quark or gluon into a final state hadron. It is a poorly understood process even in elementary collisions. RHIC's unique versatility will make it possible to study hadronization in vacuum and in the nuclear medium, and additionally with polarized beams (see Sect. 2.1 for the latter).

It has long been recognized that the hadron distributions within jets produced in p+p collisions are closely related to the fragmentation functions that have typically been measured in e^+e^- collisions and SIDIS. The key feature of this type of observable is the possibility to determine the relevant momentum fraction z experimentally as the ratio of the hadron to the jet transverse momentum. Recently [187] a quantitative relationship has been derived in a form that enables measurements of identified hadrons in jets in p+p collisions to be included in fragmentation function fits on an equal footing with e^+e^- and SIDIS data. Furthermore, hadrons in p+p jets provide unique access to the gluon fragmentation function, which is poorly determined in current fits [188], in part due to some tension found in the inclusive high p_T pion yields measured by the PHENIX and ALICE collaborations. Here, the proposed measurements can provide valuable new insight into the nature of this discrepancy.

This development motivated STAR to initiate a program of identified particle fragmentation function measurements using p+p jet data at 200 and 500 GeV from Run-11, Run-12, and Run-15. Figure 55 shows the precision that is anticipated for identified π^+ and π^- in 200 GeV p+p collisions for three representative jet p_T bins after the existing data from Run-12 and Run-15 are combined with 200 GeV p+p data from Run-24. Identified kaon and (anti)proton yields will also be obtained, with somewhat less precision, over a more limited range of hadron z. Once the Run-17 data are fully analyzed, the uncertainties for 510 GeV p+p collisions will be comparable to that shown in Fig. 55 at high jet p_T, and a factor of $\sim$ 2 larger than shown in Fig. 55 at low jet p_T. Identified hadron yields will also be measured multi-dimensionally vs. j_T, z, and jet p_T, which will provide important input for unpolarized TMD fits.

Data from the HERMES experiment [135, 137, 189] have shown that production rates of identified hadrons in semi-inclusive deep inelastic $e + A$ scattering differ from those in ep scattering. These differences cannot be explained by nuclear PDFs, as nuclear effects of strong interactions in the initial state should cancel in this observable. Only the inclusion of nuclear effects in the hadronization process allows theory to reproduce all of the dependencies (z, x, and Q^2) of R_{eA} seen in SIDIS, as shown in Fig. 56.

It is critical to see if these hadronization effects in cold nuclear matter persist at the higher

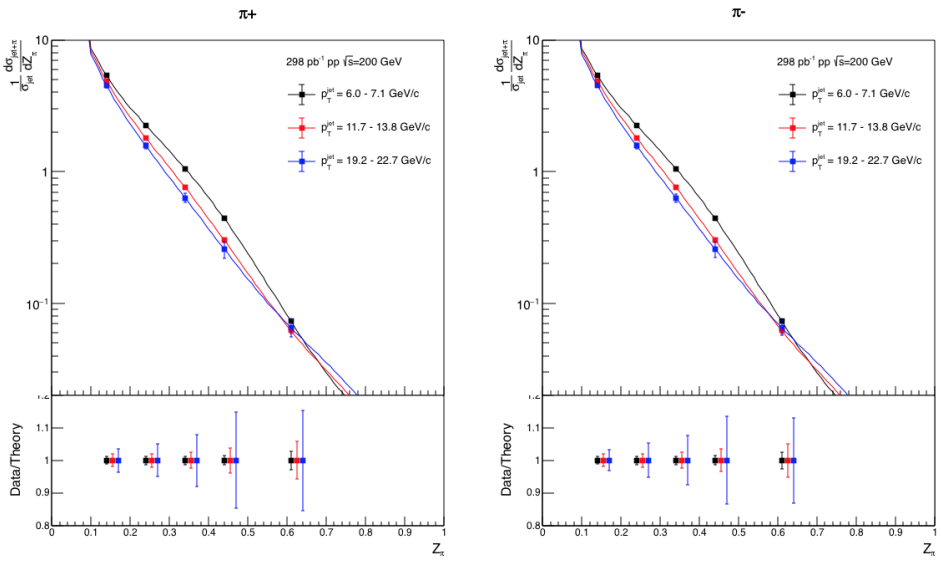

Figure 55: Anticipated precision for identified π^+(left) and π^-(right) within jets at $|\eta| < 0.4$ in 200 GeV p+p collisions for three representative jet p_T bins. The data points are plotted on theoretical predictions based on the DSSV14 pion fragmentation functions [187,188]. Kaons and (anti)protons will also be measured, over the range from $z < 0.5$ at low jet p_T to $z < 0.2$ at high jet p_T, with uncertainties a factor of ∼3 larger than those for pions.

$\sqrt{s}$ and Q^2 accessed at RHIC and EIC – both to probe the underlying mechanism, which is not understood currently, and to explore its possible universality. The combination of p+p jet data from RHIC and future SIDIS data from EIC will also provide a much clearer picture of modified gluon hadronization than will be possible with EIC data alone. Using the Run-15 200 GeV p+Au data, STAR will be able to make a first opportunistic measurement of these hadron-jet fragmentation functions in nuclei, but the precision will be limited. Additional p+Au data will be needed in Run-25 in order to provide a sensitive test for universality, as shown in Fig. 57.

2.2.3 QGP Droplet Substructure

Toroidal vorticity: In addition to cold QCD effects, a high-statistics measurement of p+Au collisions will be highly valuable to explore novel fluid configurations that have recently been predicted [193]. In particular, the data is needed to discover vortex rings or tubes at midrapidity, included by shear in the asymmetric initial state.

It has been suggested [194] that p+A collisions at RHIC form the "smallest QGP droplets." This claim is often based on anisotropic yields, which resemble those from A+A collisions that are attributed to hydrodynamic collective flow. Indeed, with well-chosen initial conditions and tuned parameters, three-dimensional viscous hydro calculations can reproduce the measured anisotropies from small, asymmetric collisions [195] at RHIC. However, a claim of QGP formation in such small systems would be much more compelling if it were based on

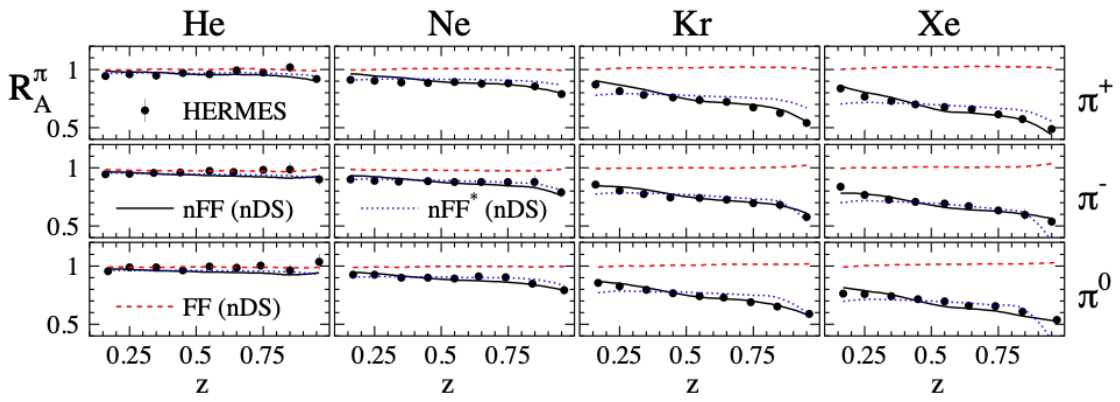

Figure 56: R_{eA} in SIDIS for different nuclei in bins of z as measured by HERMES [135, 137, 189]. The solid lines correspond to the results using effective nuclear FF [142] and the nDS medium modified parton densities [190]. The red dashed lines are estimates assuming the nDS medium modified PDFs but standard DSS vacuum FFs [191, 192] and indicate that nPDFs are insufficient to explain the data

more than one observable, especially since other, non-hydrodynamic mechanisms contribute to v_n in these systems, e.g. [196].

As Helmholtz observed more than 150 years ago [197], vortex rings are ubiquitous in hydrodynamic systems subject to initial conditions characterized by a "push down the middle," such as a smoker blowing a ring. Clear observation of this novel phenomenon would constitute important evidence that the smallest systems at RHIC truly do form a fluid system.

This signature probes aspects of particular and fundamental importance to the RHIC program, as well. The vortex ring structure is sensitive to the degree and timescale of equilibration in these small systems, as well as the extreme shear fields in the initial state [198]. Fluctuations in the vortical fields probe hydrodynamic structures at the smallest possible scales, as they arise directly from rotational derivatives in the "surface" of the flux tube.

The experimental signature of toroidal vortex structure is the so-called "ring parameter" [193]:

$$\overline{\mathcal{R}}^z_\Lambda \equiv \left\langle \frac{\vec{S}'_\Lambda \cdot (\hat{z} \times \vec{p}'_\Lambda)}{|\hat{z} \times \vec{p}'_\Lambda|} \right\rangle, \tag{5}$$

where $+\hat{z}$ is the direction of the proton beam, and the average is taken over all particles and events. This is the average polarization relative to the hyperon production plane. Rings will be most clear for central collisions, but the detailed centrality dependence of the effect is currently under investigation [198]. We focus on 0-10% centrality.

Figure 58 shows $\overline{\mathcal{R}}^z_\Lambda$ calculated [193] for completely central Au+Au and p+Au collisions at $\sqrt{s_{NN}} = 200$ GeV. Calculations were done with MUSIC [199], a three-dimensional relativistic viscous hydrodynamics simulation that locally conserves baryon number, and calculation of the thermal vorticity along the freezeout hypersurface.

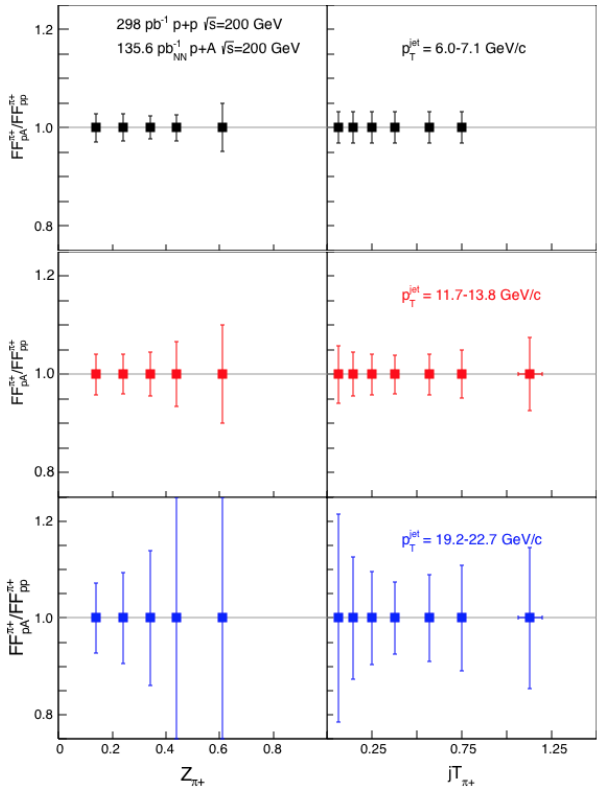

Figure 57: Anticipated precision for measurements of π^+ fragmentation functions in p+Au(Run-25),p+p (Run-24) at $|\eta| < 0.4$ vs. z and j_T for three representative jet $p_{\rm T}$ bins. Uncertainties for π^- will be similar to those shown here for π^+, while those for kaons and (anti)protons will be a factor of ~ 3 larger. Note that, to be species independent, the nucleon-nucleon equivalent luminosity is specified for p+Au.

Initial condition (a) corresponds to the usual Bjorken "boost-invariant" flow profile used in most A+A simulations, whereas condition (b) features strong shear fields generated in the initial condition, leading to observable vortex toroids. Both initial conditions generate identical $dN/d\eta$ distributions, but the latter is argued [193] to be more natural.

The statistical requirement to discover these toroidal vortex structures may be estimated by STAR's previous hyperon polarization measurements. The uncertainty on global polarization measurements $\delta\overline{P}_\Lambda \propto N_\Lambda^{-1/2} \cdot R_{\rm EP}^{-1}$, where N_Λ is the total number of hyperons in the analysis, and $R_{\rm EP}$ is the event plane resolution [3]. Because there is no event plane involved in the production plane polarization, on the other hand, the uncertainty on the ring observable goes as $\delta\overline{\mathcal{R}}_\Lambda^z \propto N_\Lambda^{-1/2}$. For the same-magnitude signal, then, $\overline{\mathcal{R}}_\Lambda^z$ enjoys an effective $R_{\rm EP}^{-2}$ "statistical advantage" over $\overline{P}_\Lambda$. Since STAR measured [33] $\overline{P}_\Lambda \approx 1\%$ at $\sqrt{s_{NN}} = 11$ GeV with 3.5σ significance, with the same number of hyperons in the analysis, we should be able to measure $\overline{\mathcal{R}}_\Lambda^z \sim 1\%$ with 7σ significance. The 11-GeV analysis involved 6M Λs, and we estimate 0.02 Λs per central $(0-10\%)$ p+Au collision at $\sqrt{s_{NN}} = 200$ GeV. Therefore, the 7σ measurement will require $6M/0.02 = 300M$ central p+Au collisions.

Also crucial to this measurement is that data must be collected with both polarities of STAR's magnetic field. This is because of large and highly nontrivial decay-topology-dependent detector effects, which will give a "false" production plane polarization signal. The magnitude of the artifact is an order of magnitude larger than the physical signal of interest, and it is highly sensitive to momentum, PID, and topological cuts. We could not

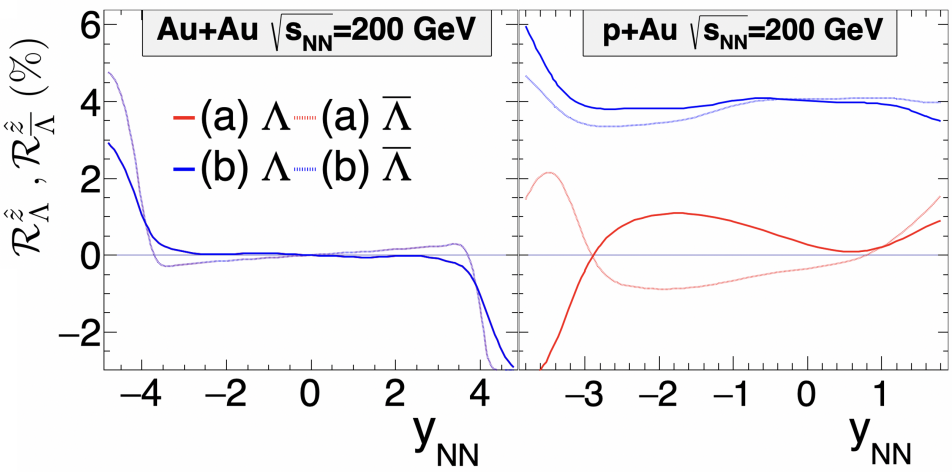

Figure 58: The "ring parameter" $\overline{\mathcal{R}}^z_\Lambda$ for $b = 0$ Au+Au and p+Au collisions at top RHIC energy. Blue (red) curves correspond to a scenario in which a toroidal vortex structure is (is not) generated by shear forces in the initial state. Solid (dashed) curves correspond to Λ ($\overline{\Lambda}$); note that baryon current is locally conserved in these collisions, so small differences between Λ and $\overline{\Lambda}$ are expected at finite baryon density. From [193].

feel confident applying such large and complex "correction factors" based solely on detector simulations, if we claim a completely novel signature with far-reaching physical implications. Fortunately, the sign of this artifact flips with the magnetic field polarity.

Figure 59 illustrates these points. Au+Au collisions at $\sqrt{s_{NN}} = 27$ GeV were recorded by STAR using opposite polarities of the magnetic field. For Λs, the quantity $\hat{p}_{\rm p} \cdot (\hat{p}_\Lambda \times \hat{z})$, where $\hat{p}_{\rm p}$ is the daughter proton momentum, is proportional to $\overline{\mathcal{R}}^z_\Lambda$. For $\overline{\Lambda}$s, the quantity $\hat{p}_{\overline{\rm p}} \cdot (\hat{p}_{\overline{\Lambda}} \times \hat{z})$, where $\hat{p}_{\rm p}$ is the daughter proton momentum, is proportional to $-\overline{\mathcal{R}}^z_{\overline{\Lambda}}$.

A rapidity cut symmetric about midrapidity ($|y| < 0.5$) was used; for a symmetric system, the physical production plane polarization vanishes by symmetry– any nonvanishing value results purely from topologically-sensitive efficiency effects.

Consider first the Λ curve from BES-I, the blue points in the left panel. Clearly, the effect has a nontrivial dependence on invariant mass; note even the asymmetry about $m_{\rm inv} = m_\Lambda$. Equally clearly, it is large, corresponding to values $\overline{\mathcal{R}}^z_\Lambda = \frac{8}{\pi\alpha_\Lambda}\hat{p}_{\rm p} \cdot (\hat{p}_\Lambda \times \hat{z}) \approx 50\%$, an order of magnitude larger than the predicted value of physical effect of interest.

In terms of topologically-sensitive efficiency effects, substituting $\Lambda \to \overline{\Lambda}$ is equivalent to flipping the sign of the magnetic field. The red datapoints in the left panel are a perfect mirror image to the blue points in that panel, as indicated by the vanishing green points, which are the sum. Further note that naive interpretation of the data in the left panel would suggest that the vortical ring values for the hyperons and antihyperons ($\overline{\mathcal{R}}^z_\Lambda$ and $\overline{\mathcal{R}}^z_{\overline{\Lambda}}$) would be identical in magnitude and sign.

The right panel shows the same colliding system, but measured during the BES-II campaign with the opposite orientation of STAR's magnetic field. As expected from the above discussion, $\overline{\mathcal{R}}^z_\Lambda = -\overline{\mathcal{R}}^z_{\overline{\Lambda}}$. The shape and magnitude of the artifact is different from the BES-I

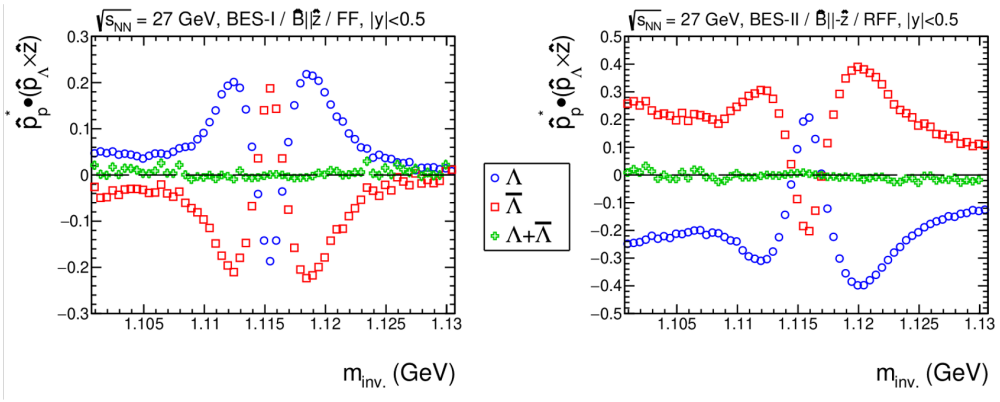

Figure 59: Production-plane polarization (modulo an overall scaling by $\frac{8\pi}{\alpha_\Lambda}$) for Λ (blue) and $\overline{\Lambda}$ (red) candidates, as a function of invariant mass. The data comes from STAR measurements of Au+Au collisions at $\sqrt{s_{NN}}$ in the BES-I (left) and BES-II (right) campaigns. STAR's solenoidal magnetic field was directed to the West and East, respectively, for these two datasets. For the BES-I data, hyperon candidates were identified with "standard" topological cuts, whereas the candidates shown in BES-II were identified using the new KFParticle package.

case, however, because a different method has been used to identify hyperon candidates. This illustrates the cut-dependence of the artifact.

In short, for reliable extraction of the ring vorticity measure, STAR must measure p+Au collisions with both field orientations, in order to cancel the complex efficiency-driven artifacts. Finally, we point out that this sort of cancellation is not unique to this observable. Indeed, there is an analogous effect for the global polarization, which precludes extracting the *first*-order azimuthal dependence of $\overline{P}_\Lambda$; there, the artifact is of order 100%, compared to the physical and measured value of $\sim 2\%$ [200].

For symmetric collisions (e.g. Au+Au), the quantity $\overline{\mathcal{R}}^z_\Lambda$ must be antisymmetric about midrapidity. However, at very forward/backward rapidities, circular vorticity has been reported in hydrodynamic [201–205] and transport [206–212] calculations. This effect, also visible in the left panel in figure 58, arises from strong temperature gradients and edge effects in three-dimensional space. It is of very different origin from the ring voriticity of interest here.

Finally, production plane polarization at large x_F has been observed (primarily) in p+p and (in some) p+A collisions [213–218] at energies up to $\sqrt{s_{NN}} = 41$ GeV. This effect, which is believed to be completely hadronic in origin but remains incompletely understood, is distinguishable from the hydrodynamically-driven ring vorticity discussed here by its rapidity dependence, which is strongly forward-focused, as well as the fact that $\overline{\Lambda}$s do not display production plane polarization at all. Thus, in addition to double-checking topologically-dependent efficiency artifacts (discussed above), it is important that STAR will measure the effect both for hyperons and antihyperons to distinguish hydrodynamic from hadronic phenomena.

3 Future Opportunities

Experience from the BES-II has shown us that the excellent performance from RHIC may allow us to take short datasets that enable unique physics programs with minimal extra running time. Below we outline two such programs, both are of great interest to STAR and the larger nuclear physics community.

3.1 Precision physics and discoveries with new nuclear species

Until shutdown, RHIC remains the only high-energy collider in the world able to rapidly switch between different ion species. For instance, the LHC does not have two ion injectors, and at present would not be able to carry out an isobar campaign like that carried out at RHIC in 2018. In this section, we discuss proposals for the use of approx. 1–2 week of beam time that involve additional nuclear species. Our first proposal simply pertains to the running of Pb+Pb collisions, which would enhance connections with the nuclear program of the LHC, while enabling us to understand much more precisely the large Au+Au data sets, as well as all other data sets collected at RHIC. Our second proposal, which would take more beam time, not only addresses the science cases related to Pb+Pb collisions, but leverages the unique capabilities of RHIC to yield new discoveries. We propose an isobar-like campaign that alternate among ^{208}Pb+^{208}Pb, ^{154}Sm+^{154}Sm, ^{166}Er+^{166}Er collisions to extract precise information about the *triaxial* structure of the ground state of those rare-earth nuclei (Sm and Er). Such a feature is of great interest for nuclear theory and the understanding of the nuclear force, yet very poorly understood.

3.1.1 Lessons from RHIC: how collective flow probes the structure of nuclei

We briefly recall one of the main outcomes of the RHIC science program carried out over twenty years: Relativistic heavy-ion collisions, coupled with multi-particle correlation measurements, give us a new tool to probe the low-energy structure of the colliding nuclei directly in their ground states.

Nuclear structure and the hydrodynamic framework. The hydrodynamic framework of heavy-ion collisions is used today to perform quantitative extractions of initial-state as well as transport properties of the QGP via state-of-the-art multi-system Bayesian analysis approaches (see e.g. [21–23]). Measurements in ^{96}Ru+^{96}Ru, ^{96}Zr+^{96}Zr collisions [219], ^{238}U+^{238}U [220] and ^{129}Xe+^{129}Xe collisions [221–225], in conjunction with dedicated theoretical studies [226–235], have indicated the dramatic impact of nuclear deformations and the nuclear radial profiles on the measured collective flow. For a reliable extraction of transport properties and initial-state physics from the data in multiple systems, nuclear structure becomes part of the problem. Conversely, it becomes possible to utilize high-energy collisions to provide information on properties of nuclei with quantified uncertainties.

It is straightforward to see why the geometry of heavy-ion collisions is sensitive to the nuclear deformation. We refer to the cartoon in Fig. 60. A nucleus can be conveniently

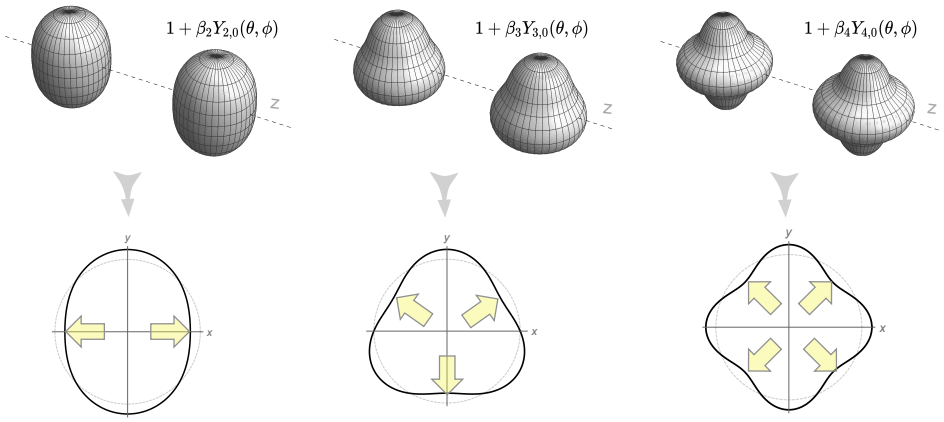

Figure 60: Collision of nuclei with quadrupole (left), octupole (middle) and hexadecapole (right) deformations, with $\beta_n = 0.25$ (we ignore the Lorentz contraction in the z-direction). The bottom row illustrates the initial condition of the medium formed after the collision in the transverse plane. The yellow arrows indicate the direction of maximal pressure gradients, along which the medium expands with the largest velocities, leading to final state harmonic flow v_n with n-fold symmetry.

modeled through a Woods-Saxon density, deformed in the intrinsic nuclear frame:

$$\rho(r,\theta,\phi) = \frac{\rho_0}{1+e^{[r-R(\theta,\phi)]/a_0}},\ R(\theta,\phi) = R_0\left(1+\beta_2[\cos\gamma Y_{2,0}+\sin\gamma Y_{2,2}]+\beta_3 Y_{3,0}+\beta_4 Y_{4,0}\right), \tag{6}$$

where the nuclear surface $R(\theta,\phi)$ includes here quadrupole, $n=2$, octupole, $n=3$ and hexadecapole, $n=4$, deformations. The angle $0 \le \gamma \le \pi/3$ controls the *triaxiality* of the structure, that is, the relative lengths of the three radii R_a, R_b, R_c of the ellipsoid: $\gamma = 0$ corresponds to a prolate shape ($R_a = R_b < R_c$), while $\gamma = \pi/3$ corresponds to an oblate shape ($R_a < R_b = R_c$). The overall radial profile is controlled by the surface diffuseness, a_0, and the half-width radius, R_0. As shown in Fig. 60, in heavy-ion collisions the shape of the deformed ions strongly affects the geometry of overlap. The entire mass distribution is probed simultaneously, and one can use multi-particle correlation observables to infer information about all the above parameters. This way of probing nuclear densities is different from the standard techniques of low-energy physics, where β_n, a_0 and R_0 are inferred from the orientation-averaged form factor data from e+A and hadron+A scatterings, and multipole transition probabilities, $B(En)$, between low-lying rotational states. The ultra-short time scales involved in a high-energy heavy-ion collision ($< 10^{-24}$s) imply that nucleon motions within the colliding ions are frozen (there, the time scale is typically on the order of 10^{-20} s [236]), and that the isotopes are imagined directly in their ground state, which is something hardly attainable in low-energy experiments based on electromagnetic interactions. So far, we understand relatively well the low-energy input used in the simulations of heavy-ion collisions, that is, high-energy data appear quantitatively consistent with nuclear properties that correspond to those actually predicted by low-energy nuclear theory

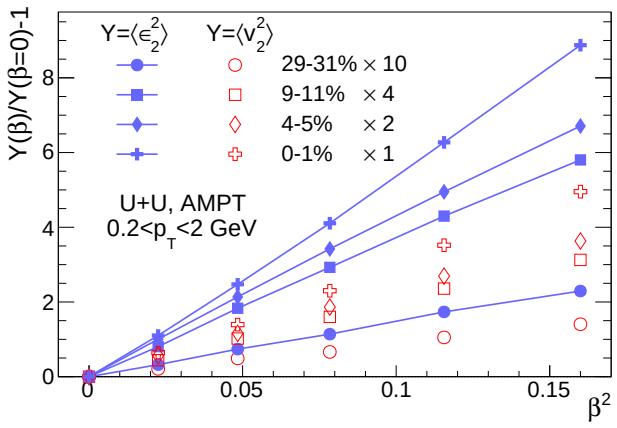

Figure 61: $\langle v_2^2(\beta)\rangle / \langle v_2^2(0)\rangle - 1 = b/a\ \beta_2^2$ (empty symbols) and $\langle \epsilon_2^2(\beta_2)\rangle / \langle \epsilon_2^2(0)\rangle - 1 = b'/a'\ \beta_2^2$ (full symbols) as a function of β_2^2 in U+U collisions from the AMPT model. Different symbols correspond to different centrality classes. Figure taken from Ref. [231].

computations of the ground states of the collided species [225, 237–239].

Quadrupole and octupole deformation. The axial multipoles, β_n, in the colliding ions modify the corresponding spatial anisotropies, ε_n, of the produced QGP, and consequently the final-state flow harmonics, v_n. For $n = 2$, we write [240, 241],

$$\langle \epsilon_2^2 \rangle = a' + b'\beta_2^2, \qquad \langle v_2^2 \rangle = a + b\beta_2^2, \tag{7}$$

where a' and a are the mean-squared eccentricity and elliptic flow in absence of deformation ($\beta_2 = 0$), while b' and b quantify the response of the eccentricity and elliptic flow, respectively, to the nuclear deformation. These relations are largely a consequence of symmetries [242], and as such are model-independent. One realization of these equations is displayed in Fig. 61 within the AMPT model. Relations similar to Eq. 7 can also be written down for v_3 and v_4, which can be used to potentially constrain octupole and hexadecapole deformations [242]. Similarly, let us also stress that a_0 and R_0 in Eq. (6) modify the "radial" flow, or the event-by-event mean transverse momentum [$p_{\rm T}$] [235], as well as the multiplicity distributions.

The STAR collaboration has established a precise method to image the nuclear shapes using so-called *isobar collisions*, as demonstrated by recent measurements in ^{96}Ru+^{96}Ru and ^{96}Zr+^{96}Zr collisions [219]. The crucial point is that since isobar nuclei produce QGP's with essentially identical properties, deviations from unity in the ratio of observables between the two systems must originate from differences in the structure of the isobars. Ratios of many observables between ^{96}Ru+^{96}Ru and ^{96}Zr+^{96}Zr [219, 243] show deviations from unity in an observable- and centrality-dependent manner. Model studies show that these ratios access nuclear structure parameter differences, i.e. $\Delta\beta_n^2 = \beta_{n\rm Ru}^2 - \beta_{n\rm Zr}^2$, $\Delta a_0 = a_{0\rm Ru} - a_{0\rm Zr}$ and $\Delta R_0 = R_{0\rm Ru} - R_{0\rm Zr}$ [244]. As observables should vary smoothly with the nuclear geometry,

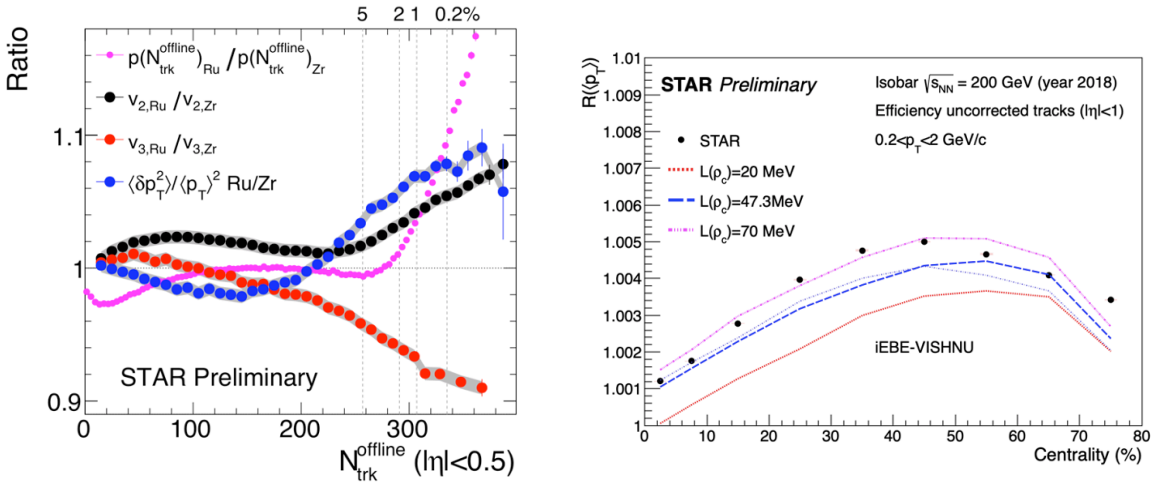

Figure 62: Left panel: STAR preliminary results of isobar ratio of $p(N_{\rm ch})$, v_2, v_3, and variances $\langle\delta p_{\rm T}^2\rangle/\langle p_T\rangle^2$ as a function of $N_{\rm ch}$. Right panel: The centrality dependence of the Ru+Ru/Zr+Zr ratio for $\langle p_T\rangle$, compared with hydrodynamic model calculations [235].

a Taylor expansion is well-suited to capture these effects:

$$R_{\mathcal{O}} \equiv \frac{\mathcal{O}_{\rm Ru}}{\mathcal{O}_{\rm Zr}} \approx 1 + c_1\Delta\beta_2^2 + c_2\Delta\beta_3^2 + c_3\Delta a_0 + c_4\Delta R_0 \ , \tag{8}$$

where the coefficients c_1–c_4 reflect properties of the hydrodynamic framework and are weak functions of system size.

Figure 62 highlights some measurements: ratios of multiplicity distribution, $p(N_{\rm ch})$, v_2, v_3, $\langle\delta p_{\rm T}^2\rangle/\langle p_{\rm T}\rangle^2$, and $\langle p_{\rm T}\rangle$ between the isobar systems. All of them show a non-monotonic centrality dependence, well captured by theoretical calculations that include effects of nuclear skin and deformations [232, 244–246]. In particular, the data imply a larger β_2 in ^{96}Ru, a larger β_3 in ^{96}Zr, and a larger a_0 in ^{96}Zr, driven by the higher neutron number. Note that the neutron skin thickness is directly related to the slope parameter L for the density dependence of the symmetry energy, which is a crucial parameter in the equation of state of neutron stars [247]. The preliminary extraction of L from the measured $\langle p_{\rm T}\rangle$ ratio in the isobar data seems to prefer a value of 47–70 MeV, as shown in Fig. 62, consistent with low-energy nuclear reactions [248], but lower than the PREXII results [249].

Beyond axial symmetry: Triaxiality A powerful probe of quadrupole deformation is the correlation between v_2 and the mean transverse momentum, $[p_{\rm T}]$, typically measured via a Pearson correlation coefficient, $\rho(v_2^2, [p_{\rm T}])$. This observable probes the full quadrupole structure of the colliding ions, i.e., both β_2 and its triaxiality γ in Eq. 6 [241, 250]:

$$\rho(v_2^2, [p_{\rm T}]) \approx a - b\cos(3\gamma)\beta^3, \ a, b > 0. \tag{9}$$

Therefore, prolate deformation in the colliding nuclei is expected to reduce $\rho(v_2^2, [p_{\rm T}])$, while oblate deformation is expected to increase it. A recent STAR measurment of this observable in U+U and Au+Au collisions established unambiguously the large influence of the

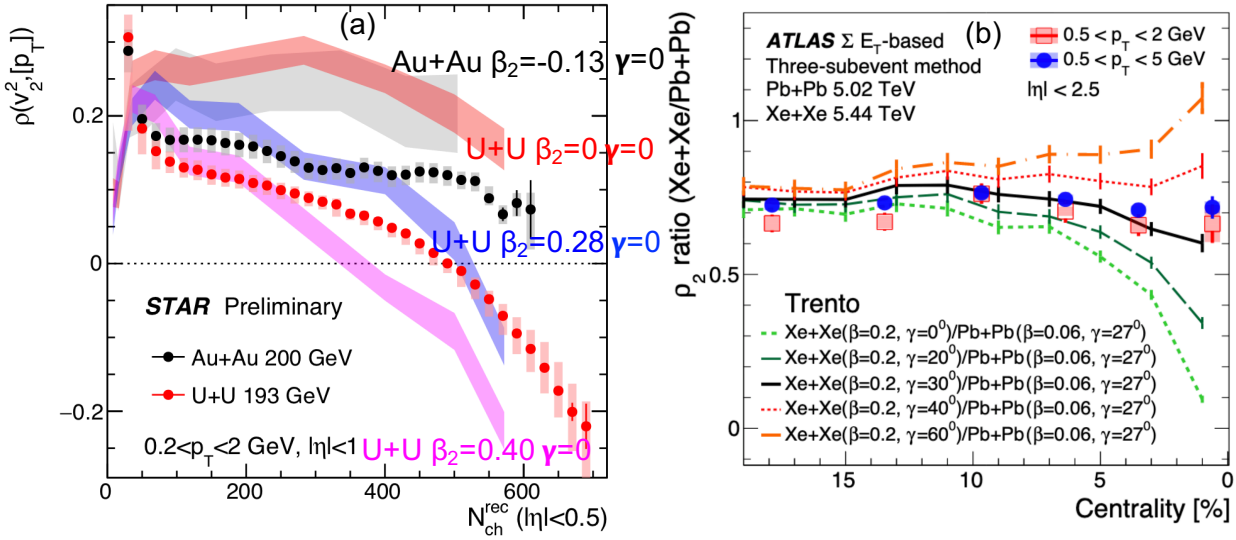

Figure 63: Left panel: STAR preliminary results of Pearson correlation coefficient $\rho(v_2^2, [p_T])$ in U+U and Au+Au collisions, showing a sign-change due to large prolate deformation of ^{238}U. Right panel: ATLAS results of the ratio of $\rho(v_2^2, [p_T])$ between Xe+Xe and Pb+Pb collisions, showing a strong preference for ^{129}Xe being a highly-deformed triaxial ellipsoid.

quadruple deformation, see Fig. 63(a). The large prolate deformation of ^{238}U yields a strong negative contribution to the $v_2 - [p_T]$ correlation, enough to make it change sign. The same measurement was also performed by the ATLAS and ALICE collaborations in ^{129}Xe+^{129}Xe and ^{208}Pb+^{208}Pb collisions [224, 251], see Fig. 63(b). A comparison with a Trento model calculation, based on input from nuclear structure theory [225], provides strong evidence that ^{129}Xe is a highly-deformed triaxial ellipsoid with an overall quadrupole deformation of $\beta_{2\mathrm{Xe}} \sim 0.2$ and triaxiality of $\gamma_{\mathrm{Xe}} \sim \pi/6$.

3.1.2 Proposal #1 – Precision flow studies and baselines with Pb+Pb collisions

The first proposal discusses physics opportunities from a short run of Pb+Pb collisions, which include three main motivations. The point is that Pb+Pb collisions represent a highly cost-effective way to produce results that would leave a lasting impact on the nuclear community, enhancing the legacy of the RHIC machine and of the U.S. high-energy nuclear program as a whole.

Comparison between RHIC and LHC data. One obvious outcome of Pb+Pb collisions at RHIC is that they facilitate comparisons with observables measured at the LHC at CERN. Although these colliders operated in parallel in the past decade, the only common species planned by both machines is ^{16}O. Complementing the O+O results with Pb+Pb results at both energies provide a unique opportunity to study the beam-energy dependence of the initial state of the collisions, going from small to large systems. Two important aspects of the problem will be elucidated by such studies:

- Longitudinal energy deposition and longitudinal energy density fluctuations remain poorly understood in heavy-ion collisions. Having identical species at two beam energies would provide unique insights into this matter, especially as we will be able to vary the system size going from small systems, O+O, to large systems, Pb+Pb.

- Role of nucleon structure and small-x evolution. There should be significant change in the partonic structure of nuclei going from RHIC to LHC energy. However, understanding this aspect requires good control on both theoretical and experimental systematics. Having both large and small species (^{208}Pb and ^{16}O) at different values of x (RHIC vs. LHC) provides the ideal condition to explore the partonic structure of the colliding nuclei, in a way that complements the investigations envisaged at the future EIC.

Neutron skin. In low-energy experiments, the neutron skin of ^{208}Pb, a doubly-magic nucleus with a considerable neutron excess, has been the subject of much work. Dedicated experiments at Jefferson Lab have been devoted to measuring the neutron skin of this nucleus. The result is $\Delta r_{np} = 0.28 \pm 0.07$ fm [249], systematically larger than predictions from energy density functional theories. The properties of neutron stars (e.g., the tidal deformability) resulting from such a constraint on the EOS turn out to be slightly at variance with those inferred from pulsar and gravitational wave observations, which has sparked intense debate in the community.

Our aim is to provide new constraints on the neutron skin of ^{208}Pb by utilizing high-energy collisions. As showcased by Bayesian analyses [238], the skin of ^{208}Pb can be constrained from collective flow results at the LHC. At RHIC, a similar analysis can be performed using Au+Au and Pb+Pb collision data, which can determine the difference Δr_{np}[Pb] $-$ Δr_{np}[Au] with good precision. This information can be combined with another estimate based on the newly developed spin interference enabled nuclear tomography method, which employs the production of ρ_0 mesons in photo-nuclear processes in ultra-peripheral collisions [252]. Fits of the coherent diffractive $|t|$ distribution within a Woods-Saxon geometry model in ultra-peripheral ^{197}Au+^{197}Au collisions lead to Δr_{np}[Au] $= 0.17 \pm 0.03$(stat.) ± 0.08(sys) fm. This method could be readily applied to ^{208}Pb via ultra-peripheral Pb+Pb collisions. It would measure the neutron skin of ^{208}Pb with an uncertainty that is lower than that obtained by the PREX-II experiment [249].

Legacy of RHIC data for precision nuclear studies. RHIC has produced a great deal of experimental results that will play an instrumental role in refining our understanding of the hydrodynamic model of the QGP. Adding Pb+Pb results to the data sets will ensure that RHIC data can indeed be used for that purpose. A recent calculation by the McGill group [239] shows that the correction to $v_2\{2\}$ coming from the quadrupole deformation of the ^{197}Au nucleus is around 40%. This means that a quantitative analysis of Au+Au collisions requires a super-refined knowledge of the low-energy structure of this nucleus. This is clearly a bottleneck. The advantage of ^{208}Pb is that it has possibly the simplest shape of all isotopes in the nuclear chart. Hence, Pb+Pb collisions will enable a precision

calibration of the hydro model via Bayesian analysis of RHIC data. The model constrained by Pb+Pb collisions, supplemented with low-energy nuclear structure input, should then be capable of describing simultaneously U+U, Au+Au Zr+Zr, Ru+Ru (and possibly O+O) data.

Summary and impact of a ≈1-week run:

- Having ^{208}Pb at $\sqrt{s_{\rm NN}} = 200$ GeV provides a crucial bridge with the LHC: comparison between RHIC and the LHC measurements will constrain the energy dependence of initial-state effects, such as longitudinal fluctuations and the nuclear partonic structure.
- We will exploit recently-developed methods to determine the neutron skin of ^{208}Pb both in hadronic collisions via collective flow, as well as in ultra-peripheral collisions via diffractive ρ_0 meson production.
- As ^{208}Pb is nearly spherical, Pb+Pb at RHIC will improve our understanding of the impact of deformation of ^{197}Au in the ultra-high-statistics Au+Au collision datasets. In addition, it will enable us to assess whether the hydrodynamic model can simultaneously describe with %-level precision the observations from U+U to O+O collisions.

3.1.3 Proposal #2 – Uncovering the nuclear force: Triaxiality in rare earths

Triaxiality occurs when the nuclear shape breaks axial symmetry. A fundamental and yet elusive property of atomic nuclei, the importance of triaxiality was highlighted as well in the 2023 U.S. Long Range Plan on nuclear structure. In low-energy nuclear experiments, determinations of the triaxiality of well-deformed nuclei are difficult and barely available, as they require the precise measurement and interpretation of a great number of excited energy levels. High-energy experiments sidestep this difficulty, which access directly many-body correlations in the ground states. We report here a memorandum submitted to us by Prof. Takaharu Otsuka (University of Tokyo), proposing to use RHIC experiments to extract the triaxiality parameter in the rare-earth nuclei ^{154}Sm and ^{166}Er.

[pages=-]figs/Otsuka.pdf

Experimental Proposal The proposal of Prof. Otsuka is timely because it permits STAR to exploit the recent advances in the study of multi-particle correlations. The determination of the triaxiality of these well-deformed nuclei can only be achieved unambiguously via an isobar-like run [219], and requires the same type of analysis of v_2-$[p_{\rm T}]$ correlations recently carried out by the STAR collaboration [253], which relies on the relation:

$$\mathrm{cov}([p_{\rm T}], v_2^2) \propto a_0 - a_1 \beta_2^3 \cos 3\gamma, \tag{10}$$

where a_0 and a_1 are positive coefficients. The impact of quadrupole deformation is directly modulated by γ, to the extent that, for large values of β, even small variations of γ may lead to experimentally-identifiable signals. Rare-earth nuclei such as those analyzed by Prof.

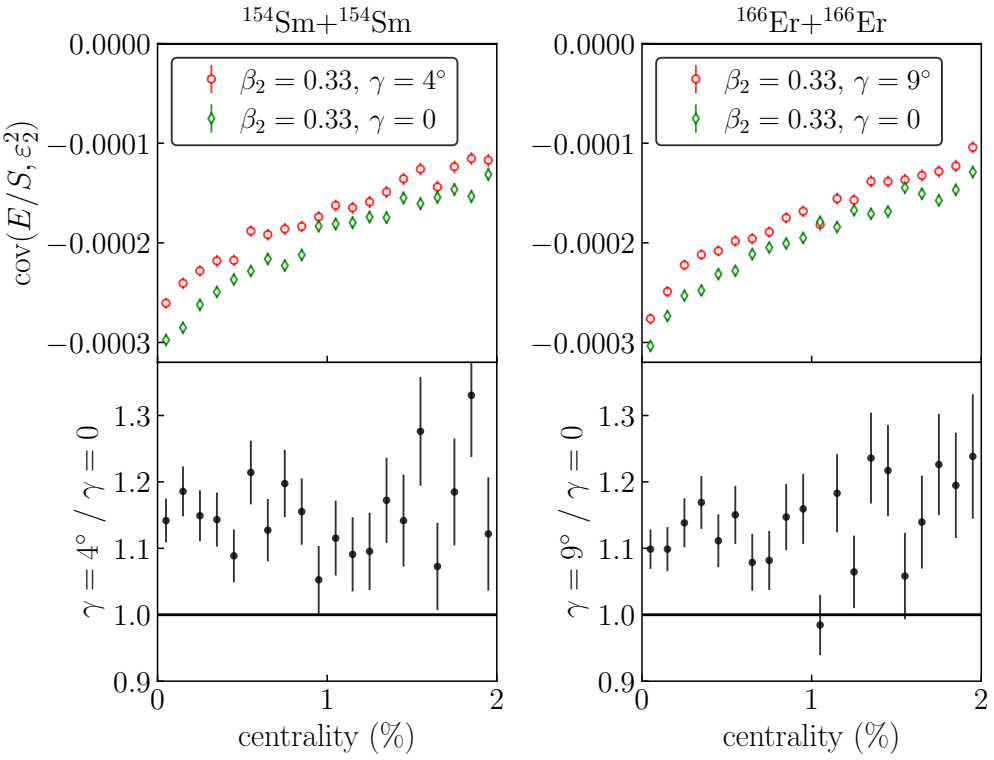

Figure 64: Method to probe the small triaxiality of well-deformed ions. The covariance of the initial-state energy, E, and eccentricity, ε_2^2, provides a good proxy of the experimentally-measured covariance of the average transverse momentum, $[p_\mathrm{T}]$, and squared elliptic flow, v_2^2, in ultra-central collisions (here shown 0-2%). Left: ^{154}Sm+^{154}Sm collisions. Right: ^{166}Sm+^{166}Sm collisions. See text for descriptions. We thank Wouter Ryssens (Université Libre de Bruxelles) for providing us with the intrinsic densities of these isotopes from density functional calculations, and Giuliano Giacalone (CERN) for performing the subsequent numerical simulations of the collisions.

Otsuka have large deformations of order $\beta_2 \approx 0.33$. Hence, determining the triaxiality of these nuclei could be easier than determining the small triaxiality of ^{238}U, which has been successfully achieved by the STAR collaboration [253].

To predict the impact of triaxiality in collisions of ^{154}Sm and ^{166}Er, we estimate the value of $\mathrm{cov}([p_\mathrm{T}], v_2^2)$ via appropriate initial-state geometric estimators within the Trento model. The results are shown in Fig. 64. They show that both a value of $\gamma \approx 4°$ in ^{154}Sm, as well as $\gamma \approx 9°$ in ^{166}Er can be resolved if this observable is measured with a relative precision of 10%. These are the values of γ predicted by the Otsuka *et al.* paper [254]. This could be achieved at RHIC with a few days of running for each species. For robust extractions, the results for $\mathrm{cov}([p_\mathrm{T}], v_2^2)$ should be compared to those obtained in ^{208}Pb+^{208}Pb collisions, which would enable us to fulfill both proposals.

Summary and impact of a ≈ 2-week run: To discover experimentally the triaxiality of well-deformed rare-earth nuclei, we propose the isobar operation mode. We will use spherical

^{208}Pb to provide the baseline. Then, we run alternately Pb+Pb collisions, Sm+Sm collisions, and Er+Er collisions, to obtain data under similar detector conditions that will ensure the cancelation of experimental systematics in the following ratios:

$$\frac{\mathrm{cov}([p_\mathrm{T}], v_2^2)_\mathrm{Sm+Sm}}{\mathrm{cov}([p_\mathrm{T}], v_2^2)_\mathrm{Pb+Pb}}, \qquad \frac{\mathrm{cov}([p_\mathrm{T}], v_2^2)_\mathrm{Er+Er}}{\mathrm{cov}([p_\mathrm{T}], v_2^2)_\mathrm{Pb+Pb}}, \qquad \frac{\mathrm{cov}([p_\mathrm{T}], v_2^2)_\mathrm{Sm+Sm}}{\mathrm{cov}([p_\mathrm{T}], v_2^2)_\mathrm{Er+Er}}. \tag{11}$$

With this, we will fully characterize the deformed structure of these rare-earth isotopes, including their triaxiality. We also envisage discoveries on the octupole and hexadecapole deformations in the ground states of these nuclei, for which there is little knowledge from low-energy experiments.

3.1.4 Summary

If there is room to explore physics with additional ion species before RHIC is shut down, our proposal is to perform, in isobar operation mode, collisions of ^{208}Pb, ^{154}Sm, and ^{166}Er nuclei. This will enable us to complete all the science cases discussed in this section. We stress that this science requires a flexible high-energy collider such as RHIC. These opportunities will be lost once RHIC is no longer in operation. These experiments will crown the efforts of two decades of work on collective phenomena in the soft sector of high-energy heavy-ion collisions.

3.2 Nuclear Data for Space Radiation Protection

This section presents the background and rationale for measurements of differential cross sections measurements of light nuclei relevant for space radiation. This is not part of the STAR physics program in the final RHIC phase but represents an opportunity for RHIC to contribute with some important nuclear data should the resources and time for these brief measurements be available. STAR has made a commitment to execute this should the opportunity materialize.

The 2015 Long Range Plan for Nuclear Science identified four key science questions for the field. The fourth of those questions was "How can the knowledge and technical progress provided by nuclear physics best be used to benefit society?" This question addresses the broader impact of the data and the knowledge generated by field of research. Recently it has come to the attention of the STAR collaboration that fixed-target collisions using light beam and target combinations could benefit the Space Radiation Protection community.

Space radiation is a serious concern to astronauts, electronics, and spacecraft. The term "space radiation" refers to the flux of energetic charges particles in the solar system. NASA has been aware of the dangers of space radiation for several decades. The energy spectrum and species composition have been studied using instruments on balloons, satellites (such as the Advanced Composition Explorer), deep space probes (such as Voyager 1), and the Space Station (Alpha Magnetic Spectrometer). The sun is responsible much of the space radiation (see fig. 65). The solar wind is comprised of protons from 0.5 to 10 keV. Solar flare events produce energetic particles (protons and some light nuclei) with energies up to a few hundred MeV/n. The highest energy portion of the space radiation field in comprised of galactic cosmic rays. 90% of the galactic cosmic ray flux is comprised of energetic protons and another 9% is Helium nuclei, the remaining 1%, is made up of nuclei from Li to Fe. The peak of the energy spectrum of the galactic cosmic rays is about 1 GeV/n, although measurable yield extends for several orders of magnitude. Solar wind particles are stopped in a few microns of material. Additionally, particles from the solar wind are deflected at the bow shock of the Earth's magnetic field, therefore they are not a concern for equipment or personnel in low earth orbit. Energetic particles from solar flares can be anticipated and can be stopped with a few tens of centimeters of shielding. Galactic rays can not effectively be shielded, therefore their affect must be studied or simulated. Although ion make up a small percentage of the GCR flux, their importance is not negligible both because the energy loss is proportional to Z^2 and because additional damage is done by the energetic light nuclei (p, d, t, ^3He, and ^4He) produced through the fragmentation of the target and projectile nuclei. The damage done by the light nuclei becomes increasingly important for higher energy cosmic rays. Light ion cross section measurements represent the largest uncertainty in space radiation estimates.

Space radiation can affect electronics through single event upsets or can induce noise in detectors or scientific equipment. The impact on astronauts is estimated by considering the total ionizing does.

Currently all components going into space are tested for radiation hardness at facilities such as the Michigan State Linac stage 1, the UC Davis cycloton, the Texas A&M K50

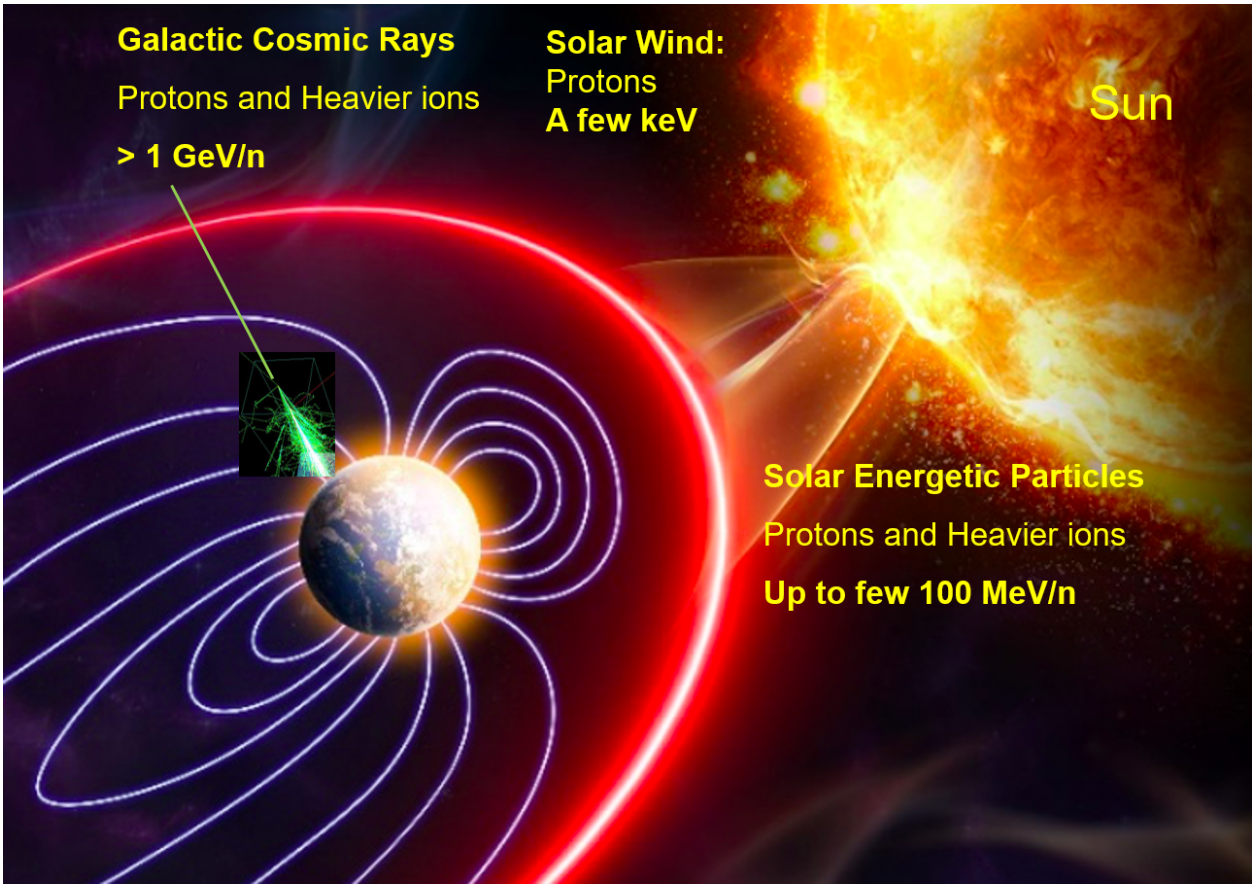

Figure 65: An illustration of the major sources and components of the space radiation flux.

and K500, the LLBNL 88 inch cyclotron and several other lower energy university facilities. Extensive measurements up to 1 GeV/n have been made at BNL at the dedicated NSRL facility which uses the booster when RHIC is not injecting beams. In addition to testing equipment, nuclear cross section data have been compiled for various beams with energies up to roughly 1 GeV/n to allow for detailed simulations of the damage incurred from both the primary particles and the secondaries created as the projectile breaks up. The Space Radiation Community has recently identified higher energy systems, using beams from 3 to 50 GeV/n on C, Al, and Fe targets as one of the next areas of need. [255] This energy range is dominated by Galactic Cosmic Rays (GCR). The requirements would be to measure the cross section for light nucleus (p, d, t, ^3He, and ^4He) production through fragmentation of the target and projectile. These data are needed now as NASA is commencing an ambitious program of long duration manned exploration beyond low earth orbit. The Artemis 1 mission launched on November 16th, 2022 for a twenty-five day unmanned transit to the moon and back. The Artemis II mission will take four astronauts to circle moon and return in late 2024, while Artemis III, in 2025, will land astronauts on the lunar surface. NASA's ambitious program sees the establishment of a lunar base and then a mission to Mars. Can the Hot QCD community provide the data needed by NASA to maximize the safety of these missions?

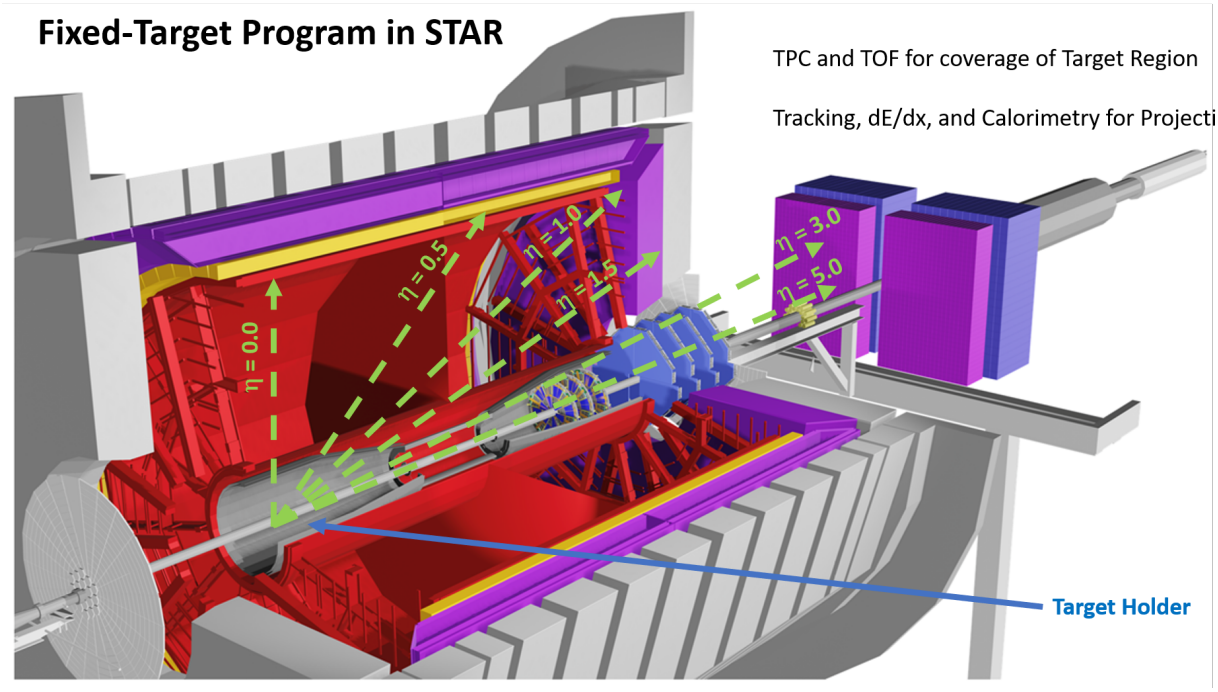

Figure 66: A schematic view of the STAR detector showing the location of the targets and the detector systems which would be needed for the measurements.

The RHIC/STAR FXT program has demonstrated that RHIC can efficiently develop and deliver the beams (C, Al, Fe) and energies (3-50 GeV) of interest, that STAR has excellent particle identification for light nuclei (p, d, t, ^3He, and ^4He) using both dE/dx and time-of-flight (capabilities specifically identified as essential in the NASA report [255], and that there is an efficient conduct of operations. We do note that the acceptance using the TPC and the barrel TOF is only in the target-side of the rapidity distribution. For symmetric systems this is not a problem; the results will be reflected about midrapidity. For asymmetric systems, both the light-on-heavy and heavy-on-light combinations will be run to ensure that both sides of the rapidity distribution will be studied. In addition, the collaboration has decided to install targets on the blue beam side of the detector to allow use of the STAR forward upgrades to make measurements of projectile fragmentation (see Fig. 66). STAR has reached out to the NASA space radiation community on several occasions determine if the STAR detector has sufficient acceptance in p_T and y to meet the needs of the Space Radiation Protection community. An overview of the RHIC/STAR capabilities was presented at the Workshop for Applied Nuclear Data Activities (WANDA2022) conference in February of 2022, at the Nuclear Data Conference (ND2022), and at a special session at DNP2022. The opportunity to make these measurements at RHIC is a unique and time-limited option to obtain critical high-energy data.

NASA had been considering constructing detector systems to make these measurements at the FAIR facility at GSI in Darmstadt, Germany. STAR is an existing detector with the required capabilities and analysis teams that have proven expertise to measure the light nuclei

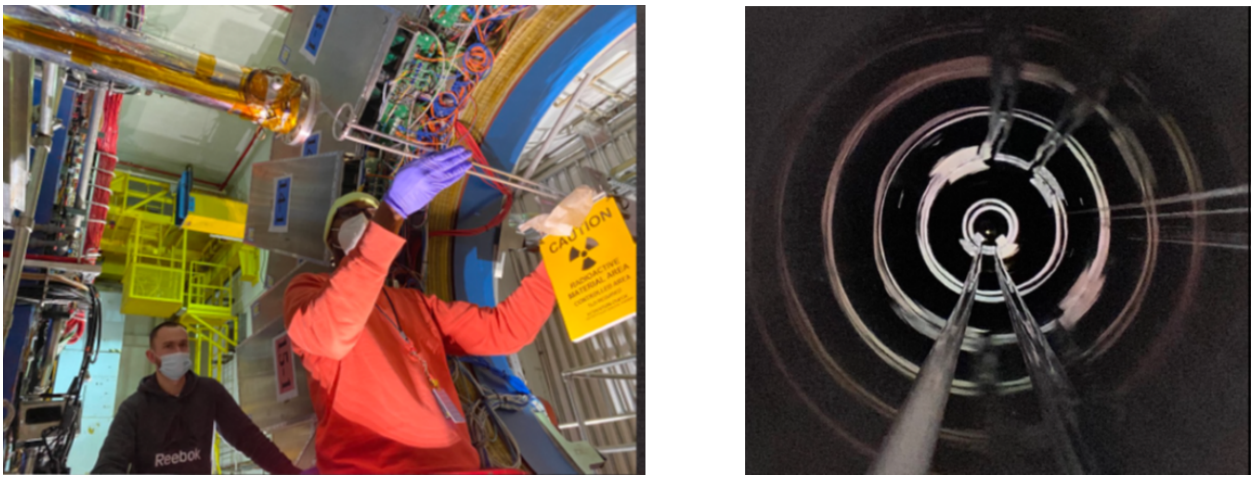

Figure 67: Left panel: Installation of the targets and holder on the East side of the STAR detector. Right Panel: A view down the beam pipe showing the three targets (C, Al, and Ni) installed at STAR.

cross sections in fixed-target experiments. The RHIC facility has demonstrated capability to efficiently deliver the required beams. In addition, there is significant uncertainty about when the SIS-100 accelerator will be available as the construction timeline has been disrupted by the war in Ukraine and the cessation of cooperation between Germany and Russia.

It has been determined that the measurements that could be made at RHIC using the STAR detector will meet the needs of the Space Radiation Protection community. These can be achieved by brief energy scans using C, Al, and Fe beams on light targets (C, Al, and Ni). Because there was a window of opportunity in December of 2022 when there was very little activity in the STAR experimental hall, we took the opportunity to open the vacuum pipe and install the three targets (see fig. 67). The carbon and nickel targets are 1 mm thick; the aluminum target is 1.5 mm thick. All target are approximately 1.8 m to the East of the center of the STAR TPC.

The suggested three energies for each beam are (E_{Tot} = 6, 21, and 51 GeV, E_{Kin} = 5, 20, and 50, or $\sqrt{s_{\rm NN}}$ = 3.6, 6.4, and 9.8 GeV respectively). For each beam species (C, Al, and Fe), the collider would need to develop the beam extraction at both E_{Tot} = 6 GeV and at the nominal injection for RHIC (12.18 GeV for Carbon, 11.729 GeV for Aluminum, and 11.31 GeV for Iron). The work needed to develop extraction could be done behind stores as the ion sources, booster, and AGS are available while beams are circulating in RHIC for the core physics program. Additional beam development time would be needed for each beam species at each energy. The experience with the FXT program suggests that the E_{Tot} = 6 GeV would need 16 hours for beam development in RHIC. The E_{Tot} = 21 GeV add the need to accelerate the beams in RHIC and therefore it is expected that these each would take 20 hours of beam development. The E_{Tot} = 51 GeV beams, would need to be accelerated more in RHIC, but due to the similarities with the E_{Tot} = 21 GeV it is expected to only need 4 hours to develop these beams. In order to get enough statistics on each of the three targets,

6 hours would be needed for each beam-energy combination. Although the grand total for this request would be 11.75 days, due to the large number of beams and the importance of scheduling beam development time, two weeks would be a more appropriate time estimate.

Beam	Energy	Targets	Time
Develop beam	5 GeV		16 hours
Carbon	5 GeV	C, Al, Ni	6 hours each (18 hours)
Develop beam	20 GeV		20 hours
Carbon	20 GeV	C, Al, Ni	6 Hours each (18 hours)
Develop beam	50 GeV		4 hours
Carbon	50 GeV	C, Al, Ni	6 hours each (18 hours)
Total			94 hours
Develop beam	5 GeV		16 hours
Aluminum	5 GeV	C, Al, Ni	6 hours each (18 hours)
Develop beam	20 GeV		20 hours
Aluminum	20 GeV	C, Al, Ni	6 Hours each (18 hours)
Develop beam	50 GeV		4 hours
Aluminum	50 GeV	C, Al, Ni	6 hours each (18 hours)
Total			94 hours
Develop beam	5 GeV		16 hours
Iron	5 GeV	C, Al, Ni	6 hours each (18 hours)
Develop beam	20 GeV		20 hours
Iron	20 GeV	C, Al, Ni	6 Hours each (18 hours)
Develop beam	50 GeV		4 hours
Iron	50 GeV	C, Al, Ni	6 hours each (18 hours)
Total			94 hours
Grand Total			11.75 days (i.e. two weeks)

Table 3: Summary of the FXT beam/target scan request. Assumptions are 16 hours of beam development for each beam at 5 GeV, 20 hours of beam development for each beam at 20 GeV, and 4 hours of beam development for each beam at 50 GeV. There would then be 18 hours of physics running (6 hours for each of the three targets) of data taking for each beam. Additionally one day would be needed to configure RHIC for low energy running.

High energy ion-on data are needed by the Space Radiation Protection community. The RHIC and STAR has developed techniques, facilities, and a knowledge base that allows us make the measurements that would benefit society by addressing a key identified need of the Space Radiation Protection community. Timely acquisition of relevant data sets would reduce the risk to astronauts, spacecraft, and equipment.

References

[1] A. Aprahamian *et al.*, (2015).

[2] F. Shen *et al.*, Nucl. Instrum. Meth. A **896**, 90 (2018), 1805.03938.

[3] J. Adams *et al.*, Nucl. Instrum. Meth. A **968**, 163970 (2020), 1912.05243.

[4] STAR, CBM eTOF Group, The CBM Collaboration eTOF Group, (2016), 1609.05102.

[5] STAR, Y. Yang, Nucl. Phys. A **1005**, 121758 (2021).

[6] P. Bozek, W. Broniowski, and J. Moreira, Phys. Rev. **C83**, 034911 (2011), 1011.3354.

[7] J. Jia and P. Huo, Phys. Rev. **C90**, 034915 (2014), 1403.6077.

[8] L.-G. Pang, H. Petersen, G.-Y. Qin, V. Roy, and X.-N. Wang, Eur. Phys. J. **A52**, 97 (2016), 1511.04131.

[9] B. Schenke and S. Schlichting, Phys. Rev. **C94**, 044907 (2016), 1605.07158.

[10] W. Li, Nucl. Phys. A **967**, 59 (2017), 1704.03576.

[11] CMS, V. Khachatryan *et al.*, Phys. Rev. C **92**, 034911 (2015), 1503.01692.

[12] ATLAS, M. Aaboud *et al.*, Eur. Phys. J. C **78**, 142 (2018), 1709.02301.

[13] STAR, L. Adamczyk *et al.*, Phys. Rev. C **98**, 034918 (2018), 1701.06496.

[14] A. Behera, M. Nie, and J. Jia, Phys. Rev. Res. **2**, 023362 (2020), 2003.04340.

[15] C. Shen and B. Schenke, Phys. Rev. **C97**, 024907 (2018), 1710.00881.

[16] S. K. Das *et al.*, Phys. Lett. B **768**, 260 (2017), 1608.02231.

[17] S. Chatterjee and P. Bożek, Phys. Rev. Lett. **120**, 192301 (2018), 1712.01189.

[18] B. Chen, M. Hu, H. Zhang, and J. Zhao, Phys. Lett. B **802**, 135271 (2020), 1910.08275.

[19] STAR, J. Adam *et al.*, Phys. Rev. Lett. **121**, 132301 (2018), 1806.02295.

[20] ATLAS, M. Aaboud *et al.*, Phys. Rev. Lett. **121**, 212301 (2018), 1806.08708.

[21] J. E. Bernhard, J. S. Moreland, S. A. Bass, J. Liu, and U. Heinz, Phys. Rev. C **94**, 024907 (2016), 1605.03954.

[22] JETSCAPE, D. Everett *et al.*, Phys. Rev. C **103**, 054904 (2021), 2011.01430.

[23] G. Nijs, W. van der Schee, U. Gürsoy, and R. Snellings, Phys. Rev. Lett. **126**, 202301 (2021), 2010.15130.

[24] G. Denicol, A. Monnai, and B. Schenke, Phys. Rev. Lett. **116**, 212301 (2016), 1512.01538.

[25] H. Niemi, G. S. Denicol, P. Huovinen, E. Molnar, and D. H. Rischke, Phys. Rev. C **86**, 014909 (2012), 1203.2452.

[26] STAR, L. Adamczyk *et al.*, Phys. Rev. Lett. **111**, 052301 (2013), 1212.3304.

[27] STAR, B. Aboona *et al.*, Phys. Rev. Lett. **130**, 112301 (2023), 2207.06568.

[28] X. Guo, S. Shi, N. Xu, Z. Xu, and P. Zhuang, Phys. Lett. B **751**, 215 (2015), 1502.04407.

[29] B. Chen, X. Du, and R. Rapp, Nucl. Part. Phys. Proc. **289-290**, 475 (2017), 1612.02089.

[30] ALICE, J. Adam *et al.*, JHEP **05**, 179 (2016), 1506.08804.

[31] ATLAS, M. Aaboud *et al.*, Eur. Phys. J. C **78**, 762 (2018), 1805.04077.

[32] CMS, A. M. Sirunyan *et al.*, Phys. Rev. Lett. **118**, 162301 (2017), 1611.01438.

[33] STAR, L. Adamczyk *et al.*, Nature **548**, 62 (2017), 1701.06657.

[34] STAR, J. Adam *et al.*, Phys. Rev. Lett. **126**, 162301 (2021), 2012.13601.

[35] STAR, B. Abelev *et al.*, Phys. Rev. C **76**, 064904 (2007), 0706.0472.

[36] Z.-T. Liang, J. Song, I. Upsal, Q. Wang, and Z.-B. Xu, Chin. Phys. C **45**, 014102 (2021), 1912.10223.

[37] Y. Xie, D. Wang, and L. P. Csernai, Eur. Phys. J. C **80**, 39 (2020), 1907.00773.

[38] STAR, M. S. Abdallah *et al.*, Nature **614**, 244 (2023), 2204.02302.

[39] X.-L. Sheng, L. Oliva, and Q. Wang, Phys. Rev. D **101**, 096005 (2020), 1910.13684.

[40] X.-L. Sheng, Q. Wang, and X.-N. Wang, Phys. Rev. D **102**, 056013 (2020), 2007.05106.

[41] V. Voronyuk *et al.*, Phys. Rev. C **83**, 054911 (2011), 1103.4239.

[42] W.-T. Deng and X.-G. Huang, Phys.Rev. **C85**, 044907 (2012), 1201.5108.

[43] X.-L. Zhao, G.-L. Ma, and Y.-G. Ma, Phys. Rev. C **99**, 034903 (2019), 1901.04151.

[44] X.-L. Zhao, Y.-G. Ma, and G.-L. Ma, Phys. Rev. C **97**, 024910 (2018), 1709.05962.

[45] D. E. Kharzeev, L. D. McLerran, and H. J. Warringa, Nucl. Phys. A **803**, 227 (2008), 0711.0950.

[46] U. Gursoy, D. Kharzeev, and K. Rajagopal, Phys. Rev. C **89**, 054905 (2014), 1401.3805.

[47] U. Gürsoy, D. Kharzeev, E. Marcus, K. Rajagopal, and C. Shen, Phys. Rev. C **98**, 055201 (2018), 1806.05288.

[48] ALICE, S. Acharya *et al.*, Phys. Rev. Lett. **125**, 022301 (2020), 1910.14406.

[49] STAR, J. Adam *et al.*, Phys. Rev. Lett. **123**, 162301 (2019), 1905.02052.

[50] STAR, L. Adamczyk *et al.*, Phys. Rev. Lett. **113**, 022301 (2014), 1312.7397, [Addendum: Phys.Rev.Lett. 113, 049903 (2014)].

[51] D. Kharzeev and R. D. Pisarski, Phys.Rev. **D61**, 111901 (2000), hep-ph/9906401.

[52] D. Kharzeev, Phys. Lett. B **633**, 260 (2006), hep-ph/0406125.

[53] Y. Feng, Y. Lin, J. Zhao, and F. Wang, Phys. Lett. B **820**, 136549 (2021), 2103.10378.

[54] STAR, M. Abdallah *et al.*, Phys. Rev. Lett. **128**, 092301 (2022), 2106.09243.

[55] R. Milton *et al.*, Phys. Rev. C **104**, 064906 (2021), 2110.01435.

[56] F. Becattini, M. Buzzegoli, A. Palermo, and G. Prokhorov, Phys. Lett. B **822**, 136706 (2021), 2009.13449.

[57] L. Finch and S. Murray, Phys. Rev. C **96**, 044911 (2017), 1801.06476.

[58] STAR, (2023), 2304.10037.

[59] S. Cao, G.-Y. Qin, and S. A. Bass, Phys. Rev. C **92**, 024907 (2015), 1505.01413.

[60] JETSCAPE, A. Kumar *et al.*, Nucl. Phys. A **1005**, 122009 (2021), 2002.07124.

[61] Y. Mehtar-Tani and K. Tywoniuk, Phys. Rev. D **98**, 051501 (2018), 1707.07361.

[62] Y. Mehtar-Tani and K. Tywoniuk, Nucl. Phys. A **979**, 165 (2018), 1706.06047.

[63] B. G. Zakharov, Eur. Phys. J. C **81**, 57 (2021), 2003.10182.

[64] L. Chen, G.-Y. Qin, S.-Y. Wei, B.-W. Xiao, and H.-Z. Zhang, Phys. Lett. B **773**, 672 (2017), 1607.01932.

[65] A. H. Mueller, B. Wu, B.-W. Xiao, and F. Yuan, Phys. Lett. B **763**, 208 (2016), 1604.04250.

[66] STAR, J. Adam *et al.*, Phys. Rev. C **102**, 054913 (2020), 2006.00582.

[67] STAR, N. R. Sahoo, PoS **HardProbes2020**, 132 (2021), 2008.08789.

[68] ALICE, J. Adam *et al.*, JHEP **09**, 170 (2015), 1506.03984.

[69] STAR, L. Adamczyk *et al.*, Phys. Rev. C **96**, 024905 (2017), 1702.01108.

[70] A. Bazavov *et al.*, Phys. Rev. D **95**, 054504 (2017), 1701.04325.

[71] S. Borsanyi *et al.*, JHEP **10**, 205 (2018), 1805.04445.

[72] STAR, M. Abdallah *et al.*, Phys. Rev. Lett. **127**, 262301 (2021), 2105.14698.

[73] CMS, V. Khachatryan *et al.*, Phys. Lett. B **772**, 489 (2017), 1605.06966.

[74] ALICE, B. Abelev *et al.*, Phys. Lett. B **718**, 1273 (2013), 1209.3715.

[75] STAR, L. Adamczyk *et al.*, Phys. Rev. C **96**, 054904 (2017), 1702.07705.

[76] ALICE, S. Acharya *et al.*, JHEP **06**, 035 (2020), 2002.10897.

[77] ALICE, S. Acharya *et al.*, (2021), 2101.02581.

[78] ALICE, S. Acharya *et al.*, (2021), 2101.04623.

[79] ALICE, S. Acharya *et al.*, (2021), 2101.04577.

[80] LHCb, R. Aaij *et al.*, Phys. Rev. C **105**, L032201 (2022), 2108.02681.

[81] M. Alvioli, L. Frankfurt, V. Guzey, M. Strikman, and M. Zhalov, CERN Proc. **1**, 151 (2018).

[82] V. Guzey and M. Zhalov, JHEP **10**, 207 (2013), 1307.4526.

[83] V. Guzey, M. Strikman, and M. Zhalov, Phys. Rev. C **99**, 015201 (2019), 1808.00740.

[84] B. Sambasivam, T. Toll, and T. Ullrich, Phys. Lett. B **803**, 135277 (2020), 1910.02899.

[85] V. Guzey, Phys. Part. Nucl. Lett. **16**, 498 (2019).

[86] V. Guzey and M. Klasen, Phys. Rev. D **104**, 114013 (2021), 2012.13277.

[87] V. Guzey and M. Klasen, Inclusive and diffractive dijet photoproduction in ultraperipheral heavy ion collisions at the LHC, in *28th International Workshop on Deep Inelastic Scattering and Related Subjects*, 2021, 2106.16084.

[88] W. Chang *et al.*, Phys. Rev. D **106**, 012007 (2022), 2204.11998.

[89] V. Guzey, M. Strikman, and M. Zhalov, Eur. Phys. J. C **74**, 2942 (2014), 1312.6486.

[90] H. Xing, C. Zhang, J. Zhou, and Y.-J. Zhou, JHEP **10**, 064 (2020), 2006.06206.

[91] STAR, J. the STAR Collaboration, Adam *et al.*, Phys. Rev. Lett. **123**, 132302 (2019), 1904.11658.

[92] W. Zha *et al.*, Phys. Rev. C **97**, 044910 (2018), 1705.01460.

[93] M. B. Gay Ducati and S. Martins, Phys. Rev. D **97**, 116013 (2018), 1804.09836.

[94] W. Shi, W. Zha, and B. Chen, Phys. Lett. B **777**, 399 (2018), 1710.00332.

[95] M. R. Whalley, D. Bourilkov, and R. C. Group, The Les Houches accord PDFs (LHAPDF) and LHAGLUE, in *HERA and the LHC: A Workshop on the Implications of HERA and LHC Physics (Startup Meeting, CERN, 26-27 March 2004; Midterm Meeting, CERN, 11-13 October 2004)*, pp. 575–581, 2005, hep-ph/0508110.

[96] M. Cacciari and G. P. Salam, Phys. Lett. B **641**, 57 (2006), hep-ph/0512210.

[97] X. Ji, F. Yuan, and Y. Zhao, Phys. Rev. Lett. **118**, 192004 (2017), 1612.02438.

[98] Y. Hatta, Y. Nakagawa, F. Yuan, Y. Zhao, and B. Xiao, Phys. Rev. D **95**, 114032 (2017), 1612.02445.

[99] S. Bhattacharya, R. Boussarie, and Y. Hatta, Phys. Rev. Lett. **128**, 182002 (2022), 2201.08709.

[100] Y. Hatta, B.-W. Xiao, and F. Yuan, Phys. Rev. Lett. **116**, 202301 (2016), 1601.01585.

[101] ZEUS, I. Abt *et al.*, JHEP **12**, 102 (2021), 2106.12377.

[102] PHENIX, C. Aidala *et al.*, Nature Phys. **15**, 214 (2019), 1805.02973.

[103] W. Zhao, C. Shen, and B. Schenke, Phys. Rev. Lett. **129**, 252302 (2022), 2203.06094.

[104] ATLAS, G. Aad *et al.*, Phys. Rev. C **104**, 014903 (2021), 2101.10771.

[105] STAR, R. A. Lacey, Nucl. Phys. A **1005**, 122041 (2021), 2002.11889.

[106] D. Kharzeev, Phys. Lett. B **378**, 238 (1996), nucl-th/9602027.

[107] C. A. Bertulani, S. R. Klein, and J. Nystrand, Ann. Rev. Nucl. Part. Sci. **55**, 271 (2005), nucl-ex/0502005.

[108] Z. Tu *et al.*, Phys. Lett. B **811**, 135877 (2020), 2005.14706.

[109] A. Accardi *et al.*, Eur. Phys. J. A **52**, 268 (2016), 1212.1701.

[110] STAR Collaboration, J. Adam *et al.*, Phys. Rev. D **103**, 092009 (2021).

[111] J.-w. Qiu and G. F. Sterman, Phys. Rev. D **59**, 014004 (1999), hep-ph/9806356.

[112] K. Kanazawa, Y. Koike, A. Metz, and D. Pitonyak, Phys. Rev. D **89**, 111501 (2014).

[113] STAR Collaboration, J. Adam *et al.*, Phys. Rev. D **103**, 072005 (2021).

[114] J. P. Ralston and D. E. Soper, Nuclear Physics B **152**, 109 (1979).

[115] R. Jaffe and X.-D. Ji, Nucl. Phys. B **375**, 527 (1992).

[116] P. Mulders and R. Tangerman, Nucl. Phys. B **461**, 197 (1996), hep-ph/9510301, [Erratum: Nucl.Phys.B 484, 538–540 (1997)].

[117] D. Sivers, Nuovo Cim. C **035N2**, 171 (2012), 1109.2521.

[118] C. Alexandrou *et al.*, Phys. Rev. D **98**, 091503 (2018).

[119] R. Jaffe and X.-D. Ji, Phys. Rev. Lett. **67**, 552 (1991).

[120] STAR Collaboration, M. Abdallah *et al.*, Phys. Rev. D **106**, 072010 (2022), 2205.11800.

[121] U. D'Alesio, F. Murgia, and C. Pisano, Phys. Rev. D **83**, 034021 (2011), 1011.2692.

[122] Z.-B. Kang, X. Liu, F. Ringer, and H. Xing, JHEP **11**, 068 (2017), 1705.08443.

[123] Z.-B. Kang, A. Prokudin, F. Ringer, and F. Yuan, Phys. Lett. B **774**, 635 (2017), 1707.00913.

[124] STAR, L. Adamczyk *et al.*, Phys. Rev. D **97**, 032004 (2018), 1708.07080.

[125] STAR, Y. Zhang, Azimuthal transverse single-spin asymmetries of inclusive jets and hadrons within jets from polarized p+p collisions at 510 GeV, in *25th International Spin Physics Symposium, Duke University*, 2023.

[126] J. Collins and J.-W. Qiu, Phys. Rev. D **75**, 114014 (2007).

[127] T. C. Rogers and P. J. Mulders, Phys. Rev. D **81**, 094006 (2010).

[128] D. Müller, D. Robaschik, B. Geyer, F.-M. Dittes, and J. Hoˇ rejši, Fortsch. Phys. **42**, 101 (1994), hep-ph/9812448.

[129] X.-D. Ji, Phys. Rev. Lett. **78**, 610 (1997), hep-ph/9603249.

[130] A. Radyushkin, Phys. Lett. B **380**, 417 (1996), hep-ph/9604317.

[131] M. Burkardt, Phys. Rev. D **62**, 071503 (2000), hep-ph/0005108, [Erratum: Phys.Rev.D 66, 119903 (2002)].

[132] S. Klein and J. Nystrand, Photoproduction of J / psi and Upsilon in pp and anti-p p collisions, in *5th Workshop on Small x and Diffractive Physics*, 2003, hep-ph/0310223.

[133] S. R. Klein, J. Nystrand, J. Seger, Y. Gorbunov, and J. Butterworth, Comput. Phys. Commun. **212**, 258 (2017), 1607.03838.

[134] J. Lansberg, L. Massacrier, L. Szymanowski, and J. Wagner, Phys. Lett. B **793**, 33 (2019), 1812.04553.

[135] HERMES, A. Airapetian *et al.*, Phys. Lett. B **577**, 37 (2003), hep-ex/0307023.

[136] HERMES, A. Airapetian *et al.*, Nucl. Phys. B **780**, 1 (2007), 0704.3270.

[137] HERMES, A. Airapetian *et al.*, Phys. Lett. B **684**, 114 (2010), 0906.2478.

[138] W. Brooks and H. Hakobyan, Nucl. Phys. A **830**, 361C (2009), 0907.4606.

[139] NuSea, M. Vasilev *et al.*, Phys. Rev. Lett. **83**, 2304 (1999), hep-ex/9906010.

[140] K. J. Eskola, P. Paakkinen, H. Paukkunen, and C. A. Salgado, Epps21: A global qcd analysis of nuclear pdfs, 2021.

[141] PHENIX, S. Adler *et al.*, Phys. Rev. Lett. **98**, 172302 (2007), nucl-ex/0610036.

[142] R. Sassot, M. Stratmann, and P. Zurita, Phys. Rev. D **81**, 054001 (2010), 0912.1311.

[143] E. Aschenauer *et al.*, (2014), 1409.1633.

[144] N. Armesto, H. Paukkunen, J. M. Penín, C. A. Salgado, and P. Zurita, Eur. Phys. J. C **76**, 218 (2016), 1512.01528.

[145] H. Paukkunen, K. J. Eskola, and C. Salgado, Nucl. Phys. A **931**, 331 (2014), 1408.4563.

[146] K. J. Eskola, H. Paukkunen, and C. A. Salgado, JHEP **10**, 213 (2013), 1308.6733.

[147] H. Paukkunen and P. Zurita, JHEP **12**, 100 (2014), 1402.6623.

[148] L. Gribov, E. Levin, and M. Ryskin, Phys. Rept. **100**, 1 (1983).

[149] E. Iancu and R. Venugopalan, The Color glass condensate and high-energy scattering in QCD, in *In *Hwa, R.C. (ed.) et al.: Quark gluon plasma* 249-3363*, 2003, hep-ph/0303204.

[150] H. Weigert, Prog. Part. Nucl. Phys. **55**, 461 (2005), hep-ph/0501087.

[151] J. Jalilian-Marian and Y. V. Kovchegov, Prog. Part. Nucl. Phys. **56**, 104 (2006), hep-ph/0505052.

[152] F. Gelis, E. Iancu, J. Jalilian-Marian, and R. Venugopalan, Ann. Rev. Nucl. Part. Sci. **60**, 463 (2010), 1002.0333.

[153] G. Giuliani, H. Zheng, and A. Bonasera, Prog. Part. Nucl. Phys. **76**, 116 (2014), 1311.1811.

[154] Y. V. Kovchegov and E. Levin, *Quantum Chromodynamics at High Energy*Cambridge Monographs on Particle Physics, Nuclear Physics and Cosmology (Cambridge University Press, 2012).

[155] A. H. Mueller and J.-w. Qiu, Nucl. Phys. B **268**, 427 (1986).

[156] L. McLerran and R. Venugopalan, Phys. Rev. D **49**, 2233 (1994).

[157] L. McLerran and R. Venugopalan, Phys. Rev. D **49**, 3352 (1994).

[158] L. McLerran and R. Venugopalan, Phys. Rev. D **50**, 2225 (1994).

[159] Y. V. Kovchegov, Phys. Rev. D **54**, 5463 (1996).

[160] Y. V. Kovchegov, Phys. Rev. D **55**, 5445 (1997).

[161] J. Jalilian-Marian, A. Kovner, L. McLerran, and H. Weigert, Phys. Rev. D **55**, 5414 (1997).

[162] A. H. Mueller, Nucl. Phys. **B415**, 373 (1994).

[163] A. H. Mueller and B. Patel, Nucl. Phys. B **425**, 471 (1994), hep-ph/9403256.

[164] I. Balitsky, Nucl. Phys. **B463**, 99 (1996), hep-ph/9509348.

[165] I. Balitsky, Phys. Rev. D **60**, 014020 (1999), hep-ph/9812311.

[166] Y. V. Kovchegov, Phys. Rev. **D60**, 034008 (1999), hep-ph/9901281.

[167] Y. V. Kovchegov, Phys. Rev. D **61**, 074018 (2000), hep-ph/9905214.

[168] J. Jalilian-Marian, A. Kovner, and H. Weigert, Phys. Rev. D **59**, 014015 (1998), hep-ph/9709432.

[169] J. Jalilian-Marian, A. Kovner, A. Leonidov, and H. Weigert, Phys. Rev. D **59**, 014014 (1998), hep-ph/9706377.

[170] E. Iancu, A. Leonidov, and L. D. McLerran, Phys. Lett. B **510**, 133 (2001), hep-ph/0102009.

[171] E. Iancu, A. Leonidov, and L. D. McLerran, Nucl. Phys. **A692**, 583 (2001), hep-ph/0011241.

[172] Y. V. Kovchegov and M. D. Sievert, Nucl. Phys. B **903**, 164 (2016), 1505.01176.

[173] CMS, S. Chatrchyan *et al.*, Eur. Phys. J. C **74**, 2951 (2014), 1401.4433.

[174] STAR, E. Braidot, Nucl. Phys. A **854**, 168 (2011), 1008.3989.

[175] PHENIX, A. Adare *et al.*, Phys. Rev. Lett. **107**, 172301 (2011), 1105.5112.

[176] C. Marquet, Nucl. Phys. A **796**, 41 (2007), 0708.0231.

[177] J. L. Albacete and C. Marquet, Phys. Rev. Lett. **105**, 162301 (2010), 1005.4065.

[178] Z.-B. Kang, I. Vitev, and H. Xing, Phys. Rev. D **85**, 054024 (2012), 1112.6021.

[179] M. Strikman and W. Vogelsang, Phys. Rev. D **83**, 034029 (2011), 1009.6123.

[180] STAR Collaboration, M. S. Abdallah *et al.*, Phys. Rev. Lett. **129**, 092501 (2022), 2111.10396.

[181] J. Jalilian-Marian and A. H. Rezaeian, Phys. Rev. D **86**, 034016 (2012), 1204.1319.

[182] J. L. Albacete and C. Marquet, Nucl. Phys. A **854**, 154 (2011), 1009.3215.

[183] K. J. Eskola, H. Paukkunen, and C. A. Salgado, JHEP **07**, 102 (2008), 0802.0139.

[184] A. H. Rezaeian, Phys. Rev. D **86**, 094016 (2012), 1209.0478.

[185] T. Sjostrand, S. Mrenna, and P. Z. Skands, Comput. Phys. Commun. **178**, 852 (2008), 0710.3820.

[186] Di-jet production from pythia8.189 is scaled down due to its overestimation of inclusive π_0 yields compared to those reported by BRAHMS in phys. rev. lett. 98 (2007) 252001 and STAR in phys. rev. lett. 97 (2006) 152302.

[187] T. Kaufmann, A. Mukherjee, and W. Vogelsang, Phys. Rev. D **92**, 054015 (2015), 1506.01415, [Erratum: Phys.Rev.D 101, 079901 (2020)].

[188] D. de Florian, R. Sassot, M. Epele, R. J. Hernández-Pinto, and M. Stratmann, Phys. Rev. D **91**, 014035 (2015), 1410.6027.

[189] A. Khouaja *et al.*, Nucl. Phys. A **780**, 1 (2006).

[190] D. de Florian and R. Sassot, Phys. Rev. D **69**, 074028 (2004), hep-ph/0311227.

[191] D. de Florian, R. Sassot, and M. Stratmann, Phys. Rev. D **75**, 114010 (2007), hep-ph/0703242.

[192] D. de Florian, R. Sassot, and M. Stratmann, Phys. Rev. D **76**, 074033 (2007), 0707.1506.

[193] M. A. Lisa *et al.*, (2021), 2101.10872.

[194] J. L. Nagle and W. A. Zajc, Ann. Rev. Nucl. Part. Sci. **68**, 211 (2018), 1801.03477.

[195] PHENIX, C. Aidala *et al.*, Phys. Rev. C **95**, 034910 (2017), 1609.02894.

[196] G. Giacalone, B. Schenke, and C. Shen, Phys. Rev. Lett. **125**, 192301 (2020), 2006.15721.

[197] H. Helmholtz, The London, Edinburgh, and Dublin Philosophical Magazine and Journal of Science **33**, 485 (1867), https://doi.org/10.1080/14786446708639824.

[198] C. Shen *et al.*, In preparation.

[199] B. Schenke, S. Jeon, and C. Gale, Phys. Rev. **C82**, 014903 (2010), 1004.1408.

[200] I. Upsal, *Global Polarization of the $\Lambda/\overline{\Lambda}$ system in the STAR BES*, Ph.D. thesis, The Ohio State University, 2018.

[201] Y. B. Ivanov and A. Soldatov, Phys. Rev. C **95**, 054915 (2017), 1701.01319.

[202] Y. B. Ivanov and A. Soldatov, Phys. Rev. C **97**, 044915 (2018), 1803.01525.

[203] Y. B. Ivanov, V. Toneev, and A. Soldatov, Phys. Atom. Nucl. **83**, 179 (2020), 1910.01332.

[204] Y. B. Ivanov, V. Toneev, and A. Soldatov, J. Phys. Conf. Ser. **1435**, 012012 (2020).

[205] B. Fu, K. Xu, X.-G. Huang, and H. Song, (2020), 2011.03740.

[206] M. Baznat, K. Gudima, A. Sorin, and O. Teryaev, Phys. Rev. C **88**, 061901 (2013), 1301.7003.

[207] O. Teryaev and R. Usubov, Phys. Rev. C **92**, 014906 (2015).

[208] M. I. Baznat, K. K. Gudima, A. S. Sorin, and O. Teryaev, Phys. Rev. C **93**, 031902 (2016), 1507.04652.

[209] W.-T. Deng and X.-G. Huang, Phys. Rev. C **93**, 064907 (2016), 1603.06117.

[210] D.-X. Wei, W.-T. Deng, and X.-G. Huang, Phys. Rev. C **99**, 014905 (2019), 1810.00151.

[211] X.-L. Xia, H. Li, Z.-B. Tang, and Q. Wang, Phys. Rev. C **98**, 024905 (2018), 1803.00867.

[212] A. Zinchenko, A. Sorin, O. Teryaev, and M. Baznat, J. Phys. Conf. Ser. **1435**, 012030 (2020).

[213] G. Bunce *et al.*, Phys. Rev. Lett. **36**, 1113 (1976).

[214] COSY-TOF, F. Hauenstein *et al.*, Eur. Phys. J. A **52**, 337 (2016), 1607.06305.

[215] F. Abe *et al.*, Phys. Rev. D **34**, 1950 (1986).

[216] B. Lundberg *et al.*, Phys. Rev. D **40**, 3557 (1989).

[217] HERA-B, I. Abt *et al.*, Phys. Lett. B **638**, 415 (2006), hep-ex/0603047.

[218] HADES, G. Agakishiev *et al.*, Eur. Phys. J. A **50**, 81 (2014), 1404.3014.

[219] STAR, M. Abdallah *et al.*, Phys. Rev. C **105**, 014901 (2022), 2109.00131.

[220] STAR, L. Adamczyk *et al.*, Phys. Rev. Lett. **115**, 222301 (2015), 1505.07812.

[221] ALICE Collaboration, Phys. Lett. B **784**, 82 (2018), 1805.01832.

[222] CMS, A. M. Sirunyan *et al.*, Phys. Rev. C **100**, 044902 (2019), 1901.07997.

[223] ATLAS Collaboration, (2019), 1911.04812.

[224] ATLAS, G. Aad *et al.*, Phys. Rev. C **107**, 054910 (2023), 2205.00039.

[225] B. Bally, M. Bender, G. Giacalone, and V. Somà, Phys. Rev. Lett. **128**, 082301 (2022), 2108.09578.

[226] U. W. Heinz and A. Kuhlman, Phys.Rev.Lett. **94**, 132301 (2005), nucl-th/0411054.

[227] Q. Y. Shou *et al.*, Phys. Lett. B **749**, 215 (2015), 1409.8375.

[228] G. Giacalone, Phys. Rev. Lett. **124**, 202301 (2020), 1910.04673.

[229] G. Giacalone, *A matter of shape: seeing the deformation of atomic nuclei at high-energy colliders*, PhD thesis, U. Paris-Saclay, 2020, 2101.00168.

[230] G. Giacalone, J. Jia, and V. Somà, (2021), 2102.08158.

[231] G. Giacalone, J. Jia, and C. Zhang, (2021), 2105.01638.

[232] C. Zhang and J. Jia, Phys. Rev. Lett. **128**, 022301 (2022), 2109.01631.

[233] H. Li *et al.*, Phys. Rev. Lett. **125**, 222301 (2020), 1910.06170.

[234] H.-j. Xu, H. Li, X. Wang, C. Shen, and F. Wang, Phys. Lett. B **819**, 136453 (2021), 2103.05595.

[235] H.-j. Xu *et al.*, (2021), 2111.14812.

[236] T. Nakatsukasa, K. Matsuyanagi, M. Matsuo, and K. Yabana, Rev. Mod. Phys. **88**, 045004 (2016), 1606.04717.

[237] W. Ryssens, G. Giacalone, B. Schenke, and C. Shen, Phys. Rev. Lett. **130**, 212302 (2023), 2302.13617.

[238] G. Giacalone, G. Nijs, and W. van der Schee, Phys. Rev. Lett. **131**, 202302 (2023), 2305.00015.

[239] N. Fortier, S. Jeon, and C. Gale, (2024), 2405.17526.

[240] G. Giacalone, Phys. Rev. C **99**, 024910 (2019), 1811.03959.

[241] J. Jia, S. Huang, and C. Zhang, (2021), 2105.05713.

[242] J. Jia, Phys. Rev. C **105**, 014905 (2022), 2106.08768.

[243] STAR, H. Xu, Acta Phys. Polon. Supp. **16**, 30 (2023), 2208.06149.

[244] J. Jia and C.-J. Zhang, (2021), 2111.15559.

[245] G. Nijs and W. van der Schee, (2021), 2112.13771.

[246] S. Zhao, H.-j. Xu, Y.-X. Liu, and H. Song, (2022), 2204.02387.

[247] J. M. Lattimer and M. Prakash, Phys. Rept. **442**, 109 (2007), astro-ph/0612440.

[248] B.-A. Li, B.-J. Cai, W.-J. Xie, and N.-B. Zhang, Universe **7**, 182 (2021), 2105.04629.

[249] PREX, D. Adhikari *et al.*, Phys. Rev. Lett. **126**, 172502 (2021), 2102.10767.

[250] J. Jia, Phys. Rev. C **105**, 044905 (2022), 2109.00604.

[251] ALICE, S. Acharya *et al.*, (2021), 2111.06106.

[252] STAR, M. Abdallah *et al.*, Sci. Adv. **9**, eabq3903 (2023), 2204.01625.

[253] STAR, (2024), 2401.06625.

[254] T. Otsuka *et al.*, (2023), 2303.11299.

[255] J. W. Norbury *et al.*, Frontiers in Physics **8** (2020).